The role of degassing in eruptive dynamics and its influence on magma rheology

A dissertation submitted to:

UNIVERSITA' DEGLI STUDI ROMA TRE
Scuola dottorale in Scienze della Terra

Cycle XXXI

For the degree of

Doctor of Sciences

Presented by

STEFANIA SICOLA

Supervisor:
Prof.ssa Claudia Romano
Co- Supervisor:
Prof. Alessandro Vona

2018

Study nature, love nature,
Stay close to nature.
It will never fail you.

Frank Lloyd Wright

Acknowledgements

There are so many people I have to thank for the help they gave me during these 3 years, but first of all I would like to say a special thank to my supervisor Claudia Romano for giving me the great opportunity to work with her in this project, choosing and trusting me without knowing me much. I have to thank her for his guidance, for having taught me to look at things from a critical point of view, showing me what does it means to be a good researcher. Thanks also for critics and reprimands, also them contributed to my growth both as scientist and as person. She gave me a great help especially in the last critical period of my Ph.D and in this particular moment of my life.

My deepest gratitude goes to Alessandro Vona, who stayed by my side (literally sometimes) in my path for the very beginning until the end. With a ton of patience he taught me probably most of the things I know now, providing indispensable advises that really opened my mind. His enthusiasm for science and research is contagious and his support was essential to my successes here. Heartfelt thanks Ale!

Special thanks to Danilo Di Genova for his precious collaboration in part of my thesis, his support, guide and friendship were fundamental; thank you for your essential contribute and for showing me how to move in a world that was completely new for me.

Very special thanks to Kelly J. Russell and Daniele Giordano for my thesis revision and the helpful suggestions; in particular I'm so grateful to Kelly for being so encouraging, positive and smiling, always.

A big THANK YOU goes to my friend Amy Ryan for her precious collaboration and the beneficial discussions; her help has been fundamental especially in the last (crazy) time of my Ph.D. Thank you buddy!

These three years wouldn't have turned out this way without all fellow PhD students (and not only): Matteo, Stefano, Aurora (my pupil), Giuditta, Silvia, Gabriele, Andrea Schito (especially for the complaining day), Ileana and anyone else I've probably forgotten but that have being part my Ph.D in someway. Very special thanks to my officemates Martina, Riccardo, Andrea, without them dark times would have been darker, and Ahmed, the best coffee maker ever!

Most of my experiments would not have been possible without the essential help of Andrea Angelini, thanks for setting up the computer in the lab! Without the following people, the analytical side of this thesis would not have been possible: thanks to Prof. Giuseppe Della Monica and

Francesco Basile for their help in samples volume analysis and for their kindness; my gratitude goes to Prof. Giancarlo Della Ventura who taught me how to make a thin section in the proper way; thanks to Sergio Lo Mastro for his help in SEM analysis and for making them always with a smile; thanks to Prof. Elsa Gliozzi for allowing me to use the micropaleontology lab microscope without any problems, but above all to encourage me from the beginning and for being my "Ph.D godmather".

Thanks to all my family, even far away, they are always by my side. A special thank to my little niece Aurora and her warm hugs.

Last but not least, I want to thank my Marco, my life companion, who has encouraged me with all his strength to pursue research, he was the first person who truly believed in me. His support has been essential, without him I probably would not be here where I am now.
Thanks for being there when I need it, always.

Abstract

Volatiles have a strong influence on volcanic and magmatic processes, both as dissolved and exsolved species. Water (H_2O) is the most dominant species and greatly affects (even at low concentration) a variety of thermodynamic and physical properties (reaction kinetics, element diffusivities, electrical conductivity, heat capacity, partial melting). Furthermore, bulk properties such as viscosity and density of the melt can vary by several orders of magnitude depending on the dissolved and exsolved water content. Such properties control the entirety of magmatic and volcanic processes from melt generation, magma rise, decompression and, ultimately, and the style of volcanic eruptions. Knowledge of the rheological properties of magmas is required for accurate modeling of the volcanic processes. For instance, rheological data are needed to quantify volatile exsolution, bubble growth rates and explosivity of volcanic eruptions.

In this thesis the role of degassing in silicic melts is investigated, combining different techniques, involving the study of both dissolved and exsolved volatiles in volcanic materials.

The study of degassing process requires an accurate quantification of dissolved H_2O. Analytical studies of water distribution in natural glasses are here performed by Raman spectroscopy techniques. A calibration model for water content estimation of natural glassy samples is provided for a wide range of compositions (from basalt to rhyolite including alkali- and iron-rich).

In the second part of this thesis, H_2O exsolution is investigated with a new experimental approach, in order to better constrain the relationship between viscosity and porosity. The proposed viscosity models highlight the importance of different frameworks phase for modeling magma rheology.

The last part of this thesis regards the study of H_2O resorption. The rehydration of melt could occurs after degassing and exsolution, when the slow cooling of the magma allows H_2O to “return” in the melt. Dome extrusions or ignimbrites and lava emplacement represent some possible volcanic scenarios in which this phenomenon could alter the physical characteristic of the material.

In conclusion, this thesis provides an in depth investigation of H_2O both as dissolved and exsolved species in order to better understand degassing processes and how they affect the rheological behavior of magmas.

Contents

Introduction

Motivation and objective

Volcanoes display a wide range of eruption styles, from the effusion of lava flow or domes over periods of days to decades, to explosive eruptions that last for seconds to days to months that eject material into the stratosphere. Approximately 800 million people around the world live close enough volcanoes to be directly affected by an eruption (Loughlin et al. 2015), and many more are at risk of social or economic impact as the consequences of volcanism extend from regional to potentially global areas (e.g. Svensen et al. 2004). The challenge posed by volcanology is to be able to model the dynamics of volcanoes from magma ascent, to eruption and emplacement. One of the central topics in volcanology concerns the role of degassing in magmas, both as initial dissolved phase and as exsolved fluids. Violent degassing results in explosive eruption and formation of pyroclastic deposits; on the other hand, slow degassing allows the separation of exsolved gases from host magma and the eruption of degassed lava or domes (Carroll and Holloway 1994).

Volatiles (H_2O and CO_2 are the dominant species) are present in all terrestrial magmas. Dissolved and exsolved volatiles strongly affect the thermodynamic and physical properties of the melt and dramatically influence magmatic and volcanic processes (Hess and Dingwell 1996; Ryan et al. 2015). Water (H_2O) is the most relevant volatile species in volcanic system and plays a fundamental role in magma dynamics and evolution; for instance, the addition of 1 wt.% H_2O to an andesitic melt results in a viscosity decrease of more three orders of magnitude (Richet et al. 1996; Hess and Dingwell, 1996; Vetere et al. 2006; Le Losq et al, 2012). Also physical and chemical properties of magma are strongly affected by the presence of water, for example volatiles control solidus temperature, partial melting, melt viscosity, thermodynamic properties and eruption style.

The understanding of volatile behavior during dissolution/exsolution clearly demands an accurate quantification of the water dissolved in volcanic products (e.g. melt and fluid inclusions). Volcanic glasses, from glass shards to melt inclusions trapped in crystals, represent the products of most volcanic eruptions. Analytical studies of water distributions in natural glasses are therefore crucial for understanding physical and chemical processes (reducing solidus temperature, vesiculation and formation of foam, crystallization, magma transport, emplacing of lava flow etc),

and their feedbacks, occurring before, during, and after the eruption (Bachmann et al., 2009; Berry et al., 2008; Blundy and Cashman, 2005; Dingwell, 2006; Hartley et al., 2014; Kennedy et al., 2005; Métrich et al., 2010).

Dissolved water content can be estimated through several techniques as Fourier transform infrared spectroscopy (FTIR), Karl Fischer titration (KFT), and Thermogravimetric analysis (TGA). Nevertheless, all of these methods present some drawbacks and limitations that make them unsuitable for general use. FTIR measurements require precise knowledge of the extinction coefficients of the glasses. These are a complex function of composition and are not available for most multicomponent natural melt. Moreover, the extinction coefficients are also function of temperature so that high T measurements cannot often give quantitative results. Even in cases where absorption coefficients are available and accurate, FTIR measurements require bulk sample of certain size and complex sample preparation. KFT is an absolute method, which gives quantitative results. However, it requires a certain amount of sample and it is a destructive technique. Moreover, it cannot be used for melt/fluid inclusion samples. In TGA methodology, the mass of the sample is measured over time and as temperature changes; as the sample is heated the dissolved volatiles start to exsolve and degas and the change in mass is proportional to the volatile loss. This technique allows to record the amount of gases which where dissolved in the sample but it is also a destructive technique and it cannot be used to study melt/fluid inclusion samples.

Recently, Raman spectroscopy has been used to quantify water content (H_2Omolecular/OH) (Behrens et al. 2006; Le Losq et al., 2012). The main advantages of Raman spectroscopy, over other standard techniques typically used for water content determination, are represented by the minor sample preparation, the non-destructiveness of the technique and high-spatial resolution of few μm.

In the pre-existing studies (Thomas, 2000, 2006; Behrens et al., 2006; Mercier et al., 2009, 2010; Di Muro et al, 2006, 2010; Le Losq et al. 2012) only few selected magmas were calibrated, mainly iron-free and calc-alkaline in compositions. Moreover, the effect of crystals at the micro- and nanoscale on the Raman spectra, known to be dramatic, was only recently investigated by Di Genova et al. (2017b).

In order to fill this gap, and to extend the calibration over a wider range of natural compositions, in particular related to the iron-bearing alkaline potassic magmas typical of the Italian volcanic provinces, here, we investigate a series of hydrous glasses with $FeO_{tot.}$ up to 14.1 wt.% characterized by chemical composition spanning from basalt to iron-poor and iron-rich phonolite and rhyolite. We used two Raman spectrometers to investigate possible effects of diverse instrumental characteristics.

The quantification of the water content in glasses/inclusion is, of course, only the first step to study the degassing process in magmas and the effect of the exsolution on the rheological properties of magmas (i.e. second part of my thesis). Magmatic volatile contents are generally assumed to decrease as magmas ascend toward the Earth's surface as a consequence of their evolving saturation state in the melt as pressure decreases. This decrease in pressure causes a decrease in solubility, and volatiles (which were initially dissolved at higher pressures) exsolve and nucleation and growth of gas as bubbles occur (Pal, 2003). The segregation of gas from melt can also lead to chemical differentiation and can induce changes in magma physical properties, density and viscosity (Hess and Dingwell 1996; Navon et al. 1998; Mysen and Acton 1999; Sparks et al. 1999; Zhang 1999; Gardner et al. 2000; Di Matteo et al. 2004; Zhang et al. 2007; Giordano et al. 2008; Behrens and Zhang, 2009; Bouhifd et al., 2015; Dingwell et al., 1996; Stebbins et al., 1995; Lange and Carmichael, 1990; Whittington et al., 2000).

Whilst the effects of dissolved volatiles on melt viscosity are well known, the effects of exsolved fluid (i.e. bubbles) on the bulk viscosity of magmas remain unresolved. Indeed, exsolved volatiles, expressed as magma porosity, also affect the rheology of magmas; the rheology of bubble-bearing magma controls the dynamics of volcanic eruption and can modify the eruptive style and the flow of magma and lavas, making it a central issue in volcanology.

Several studies have been conducted investigating the effects of porosity on magma viscosity in natural melts. These studies include experiments and models based on different approaches (theoretical/empirical). Theoretical models predict a wide range of behavior and a significant rise in magma viscosity (e.g. ~1 order of magnitude) as a function of increasing porosity. Other theoretical models predict a near-linear decrease in relative viscosity (η_{bulk}/η_0) with increasing porosity. Those works take into account the effects of bubbles on melt viscosity as a function of capillary number (Ca) in steady, simple-shearing flows. The capillary number is defined as $Ca = \lambda \dot{\gamma}$ where $\dot{\gamma}$ is the shear strain rate and λ is the bubble relaxation time. For example, Llewellin and Manga (2005) identified two flow regimes (based on the previous work of Pal, 2003 and Bagdassarov and Dinwgell, 1992): Regime 1 in which shear viscosity increases with increasing gas volume-fraction ($Ca \leq 1$) and Regime 2 where shear viscosity decreases with increasing gas volume-fraction ($Ca \geq 1$). Llewellin and Manga (2005) work is in agreement with some existing experimental/theoretical/numerical data but fails on others.

Empirical models include experimental data obtained using different rheometrical apparatus (compression or torsion) on a variety of materials (analogue or natural). Moreover, those experiments are performed on starting materials which vary from unconsolidated or sintered particles with interclast porosity (Rahaman et al.,1987; Ducamp and Raj, 1989; Sura and Panda,

1990; Quane and Russell, 2005; Quane et al., 2009) and frameworks configuration with distributed porosity (Bagdassarov and Dingwell, 1992, 1993; Lejeune et al., 1999; Stein and Spera, 2002). All the experimental data are in the regime of ($Ca \geq 1$) (viscosity decreases as a function of porosity), and within this regime they do not show consistent trends The fitting of those experimental data describes a wide range of behavior in $Ca \geq 1$ regime. Furthermore, experimental models concerning the effect of porosity on viscosity on natural material are very few (Bagdassarov and Dingwell, 1992; Quane et al., 2009; Heap et al., 2014; Vona et al., 2016). On this view, despite the wide literature existing, those studies are often in disagreement each other and a general parameterization is not available so far. Given the paucity of experimental data on natural materials and the discrepancy among the different set of data and models, we decided to investigate the rheology of porous melts at $Ca \geq 1$ with a new set of experiments especially designed to investigate the in situ high-temperature degassing and deformation process of natural rhyolites.

The same degassing experiments have then been used to analyze the reverse phenomenon, in which H_2O, as a result of a decrease in temperature, can "turn back" in the melt or be "resorbed". This process occurs in any volcanic environment where cooling is slow, as in welding of pyroclastic deposits or the emplacement of lava flow of silicic melts. The most important consequence of this process is a decrease of the effective glass transition temperature (Tg) of the melt, leading to an expansion of the melt field relative to the glassy state.

In this last part of my work, I tried to define, through a series or degassing experiments, this resorption process and to identify the cooling rate region where such a process is activated.

In summary, the objectives of the present work can be resumes as it follows:

1. Estimation of water content of natural hydrous glasses through Raman spectroscopy;

2. Investigation of the degassing process in natural rhyolites and its effects on the their rheological behavior;

3. Investigation of the water resorption process during cooling of silicic melts.

Thesis outline

This thesis consists of four main chapters. In Chapter 1 the estimation of water content in hydrous glasses through Raman spectroscopy is described and a model is presented. This part is provided in the form of a short-length research article and also supplementary material is attached. The model was developed analyzing several hydrous glasses having different compositions spanning from basalt to rhyolite synthetized at different water contents up to 4.5 wt.% H_2O. All the samples have been analyzed both in Roma Tre and LMU in Munich, in order to make a comparison between two instruments and make the model consistent.

In Chapter 2 a new set of high-temperature experiments to investigate the rheology of porous and bubble-bearing melts is presented. Experiments were performed at 1 atm using TMA and the starting materials are 5 x 5 mm cores of natural rhyolitic obsidian from Krafla, Iceland (vesicle and crystal-free). The results of this study highlight the effect of porosity on the viscosity of natural rhyolitic obsidian, taking into consideration for the first time the pore nature in addition to the overall porosity (vapor filled or empty). Indeed, these experiments have been used to develop an empirical model for melt rheology, which takes into account both the volume fraction of bubbles and their nature. This chapter is written in the form of a research article and will be soon submitted to an international journal.

In Chapter 3 high temperature degassing experiments were performed in order to explore the water resorption process during cooling. In particular, the objective of the work was to identify the minimum cooling rate at which resorption processes are occurring. Preliminary results are presented and additional work is currently underway.

An overall discussion that links the results in a comprehensive overview is presented in the last section (Chapter 4). Some suggestions for future research are presented as well.

Chapter 1

Effect of iron and nanolites on Raman spectra of volcanic glasses: A reassessment of existing strategies to estimate the water content

Note – This chapter has been published as:

Di Genova, D., Sicola, S., Romano, C., Vona, A., Fanara, S., Spina, L., 2017a. Effect of iron and nanolites on Raman spectra of volcanic glasses: reassessment of existing strategies to estimate the water content. Chem. Geol. 475:76–86. https://doi.org/10.1016/j.chemgeo.2017.10.035.

Abstract: The effect of iron content and iron nanolites on Raman spectra of hydrous geologically-relevant glasses is presented. Current procedures to estimate the water content using Raman spectra were tested to explore potential effects of iron content, its oxidation state, and nanolites on models' reliability. A chemical interval spanning from basalt to rhyolite, including alkali- and iron-rich compositions, with water content up to 5.6 wt.% was investigated using two spectrometers. When considering nanolite-free samples, the area of the band at 3550 cm^{-1} linearly correlates with the sample water content regardless of chemical composition. Using this approach, data were reproduced with a root-mean-square error (RMSE) of ~ 0.15 wt.%. Depending on the sample chemistry, water content, and acquisition conditions the laser-induced sample oxidation led to underestimating the water content up to ~90% with a long acquisition time (26 min). Normalizing the water band region to the silicate band region minimizes such a limitation. The area ratio between these bands linearly correlates with the water content and the use of different baseline procedures does not remove the dependence of such a correlation by the iron content and its oxidation state. With this procedure, data were reproduced with a RMSE of ~0.16 wt.%. For both approaches, the presence of iron nanolites may result in underestimating the water content.

1. Introduction

Water is the most abundant volatile species dissolved in natural melts and greatly affects, even at low concentration, a variety of thermodynamic and physical properties, from phase equilibria, to reaction kinetics, element diffusivities, electrical conductivity, heat capacity, and partial melting (Behrens and Zhang, 2009; Giordano et al., 2015; Lange and Carmichael, 1990; Poe

et al., 2012; Scaillet and Macdonald, 2001; Stebbins et al., 1995). Moreover, bulk properties such as viscosity and density of the melt can vary by several orders of magnitude depending on the dissolved water content (Bouhifd et al., 2015; Dingwell et al., 1996; Lange and Carmichael, 1990; Whittington et al., 2000). Such properties control the entirety of magmatic and volcanic processes occurring from the melt generation, magma rise, decompression and, ultimately, the fate and style of volcanic eruptions. Volcanic glasses, from glass shards to melt inclusions trapped in crystals, represent the products of most of volcanic eruptions. Analytical studies of water distribution in natural glasses are crucial for understanding the plethora of physical and chemical processes, and their feedbacks, occurring before, during, and after the eruption (Bachmann et al., 2009; Berry et al., 2008; Blundy and Cashman, 2005; Dingwell, 2006; Hartley et al., 2014; Kennedy et al., 2005; Métrich et al., 2010). Moreover, investigations of run products from solubility, diffusion, decompression, crystallisation, and bubble nucleation experiments help to constrain the timescale of physical and chemical processes in hydrous systems (Blundy and Cashman, 2005; Fanara et al., 2015; Gardner et al., 2000; Gonnermann and Gardner, 2013; Hammer et al., 2000; Le Gall and Pichavant, 2016; Martel and Iacono- Marziano, 2015; Shishkina et al., 2010).

Raman spectroscopy is a non-destructive technique used to chemically discriminate glasses, study and estimate the oxygen fugacity and volatile content (e.g., Di Genova et al., 2016a, 2016b; Di Muro et al., 2006a, 2009; Le Losq et al., 2012; Morizet et al., 2013; Thomas, 2000). The minor sample preparation and high-spatial resolution of few μm represent the main advantages of using Raman spectroscopy over other standard techniques typically used for water content determination [Fourier transform infrared spectroscopy (FTIR), Karl Fischer titration (KFT), and thermogravimetric analysis (TGA)]. The potential of Raman spectroscopy, together with progress in the performance of spectrometers, now opens future opportunities for producing high-resolution maps of water distribution in volcanic and experimental products necessary to constrain processes involved in volcanic eruptions and their equilibrium versus disequilibrium timescales. Over the past few decades, several authors have adopted different protocols for the quantification of water content by Raman spectroscopy based on internal and external calibrations (Behrens et al., 2006; Chabiron et al., 2004; Di Muro et al., 2006b; Mercier et al., 2009; Thomas, 2000; Thomas et al., 2008; Zajacz et al., 2005). The external calibration requires a set of standards where the water content is independently determined (Behrens et al., 2006; Thomas et al., 2008; Mercier et al., 2009).

Moreover, each spectrometer needs to be calibrated due to the different performance of detectors and instrumental settings (e.g., grating, excitation source, objective, acquisition time, focus depth), which affect the spectra intensity and the band area. Differently, the internal calibration is based on spectra normalization between the water and silicate regions. This approach

is expected to remove most of instrumental effects on Raman spectra. Therefore, so far, the internal calibration has been considered to allow different laboratories to use a common calibration. In order to provide a single calibration valid over a large compositional interval, Le Losq et al. (2012) embedded the chemical-dependence of Raman spectra into a background procedure, which depends on the sample SiO_2 content (more details are provided in the following sections). After background subtraction, their calibration relied on the ratio (HW/LW) between the water (HW, 2700–3900 cm^{-1}) and silicate (LW, 200–1300 cm^{-1}) area bands to estimate the dissolved water content H_2O (wt%) as follows:

1) $$\frac{H_2O}{100-H_2O} = A \cdot \frac{HW}{LW}$$

The left member of the equation represents the water/glass proportion and the A coefficient is equal to $7.609 \cdot 10^{-3}$. While A might change with the used spectrometer, the relationship between HW/LW and the water/glass proportion was found to be unique and linear regardless of the sample composition (Le Losq et al., 2012). However, the starting materials used in their study were mainly iron-free glasses (9 out of 12 glasses).

Natural glasses contain iron, which is present in both reduced (Fe^{2+}) and oxidized ($Fe^{3+)}$ forms depending on temperature, oxygen fugacity, and chemical composition. The dual behavior of iron affects the Raman spectra of natural glasses (Di Muro et al., 2009; Di Genova et al., 2016a). Moreover, Di Muro et al. (2006a, 2006b) and Di Genova et al. (2017b) found that iron-bearing crystals at the micro and nanoscale dramatically alter the Raman features of glasses. These particles nucleate and grow during cooling or thermal annealing above the glass transition temperature and have been recently recognized to be pervasive in experimental specimens and natural products (b et al. 2017). Based on these observations, it is evident that any Raman model used to estimate the water content of natural products should consider such effects. These considerations led us to reassess the relationship between Raman spectra and the water content of volcanic glasses.

Here, we investigate a series of hydrous glasses with FeO_{tot}. up to 14.1 wt.% characterized by chemical composition spanning from basalt to iron-poor and iron-rich phonolite and rhyolite. We used two Raman instruments to investigate possible effects of diverse instrumental characteristics. This contribution aims to test current strategies and provide reliable procedures to estimate the water content of naturally-occurring glasses by Raman spectrometry.

Table 1

Dry composition (wt.%) of starting materials.

Sample	**KR**[a]	**HO**[a]	**ETN**[b]	**FR**[b]	**AMS**[b]	**PS-GM**[b]	**472AD**[c]	**79AD**[c]	**V_1631_W**[d]	**RH**[e]
Composition	Fe^{+} Basalt	Dacite	Trachy-Basalt	Latite	Trachyte	Fe^{+} Rhyolite	Fe^{+} Phonolite	Fe^{-} Phonolite	Tephri-Phonolite	Fe^{-} Rhyolite
H_2O[e]	TGA	TGA	KFT+NIR	KFT+NIR	KFT+NIR	KFT+NIR	KFT	KFT	NIR	TGA
SiO_2	50.24	66.17	48.06	56.55	57.72	69.21	51.36	56.09	53.52	78.87
TiO_2	1.99	0.77	1.67	0.81	0.39	0.5	0.48	0.19	0.6	0.10
Al_2O_3	13.55	15.96	16.72	17.92	18.4	9.18	21.63	22.02	19.84	12.52
$FeO_{tot.}$	14.08	5.02	9.92	6.59	4.51	7.94	4.54	2.26	4.8	1.55
MnO	0.25	0.12	0.24	0.17	0.1	0.32	-	-	0.14	0.04
MgO	5.86	1.70	5.46	2.36	1.46	0.08	0.74	0.18	1.76	0.04
CaO	10.09	4.65	10.03	5.52	4.23	0.6	5.90	2.8	6.76	0.84
Na_2O	2.46	3.70	3.68	4.55	3.72	6.52	5.92	6.22	4.66	1.01
K_2O	0.32	2.23	1.83	4.53	7.9	4.35	9.42	10.25	7.91	5.28
P_2O_5	0.55	0.01	0.48	0.01	0.19	0.04	-	-	-	0.02

[a] This study; [b] Di Genova et al., 2014; [c] Scaillet and Pichavant, 2004; [d] Romano et al., 2003; [e]Di Genova et al., under review.

[e] The dissolved water content in glass was determined by thermogravimetric (TGA), Karl–Fischer titration (KFT), and near-infrared spectroscopy (NIR) analyses.

2. Materials and analytical methods

To explore chemical effects on Raman spectra of glasses, we investigated hydrous samples with variable water content over a wide range of chemical composition. Sample set includes 20 glasses from previous studies and 9 glasses synthesized specifically for this study. In term of silica, iron, and alkali content, the used compositions span almost the entire chemical spectrum of magmas erupted on Earth.

2.1. Samples and starting material from previous studies

The chemical composition of samples synthesized in previous studies is reported in Table 1 and shown in a TAS (total alkali versus silica) diagram in Fig. 1A. The samples include:

– Trachybasalt (ETN, Di Genova et al., 2014a) from Etna (1991–1993 lava flow field in Val Calanna, Italy);

– Latite (FR, Di Genova et al., 2014b) from Fondo Riccio eruption (9.5 ka Campi Flegrei, Italy);

– Trachyte (AMS-B1, Di Genova et al., 2014a) from Agnano Monte Spina eruption (4400 BP Campi Flegrei, Italy);

– Phono-tephrite (V_1631_W, Romano et al., 2003) from AD 1631 Vesuvius eruption;

– Tephri-phonolite (472AD) and phonolite (79AD) from Scaillet and Pichavant (2004) belonging to the main explosive phases of Pollena (472AD) and Pompei (79AD) Vesuvius eruptions;

– Iron-rich rhyolite (PS-GM, Di Genova et al., 2013) from the Khaggiar lava flow (8.2 to 5.5 ka Pantelleria, Italy);

– An anhydrous iron poor-rhyolite (RH, Di Genova et al. 2017b) with chemistry similar to rhyolitic melts of the Yellowstone Plateau Volcanic Field (USA).

Details of the experimental procedures employed to synthesize hydrous glasses are reported in the mentioned studies. Detailed anhydrous composition and water contents (determined by FTIR, TGA, and/or KFT) are reported below.

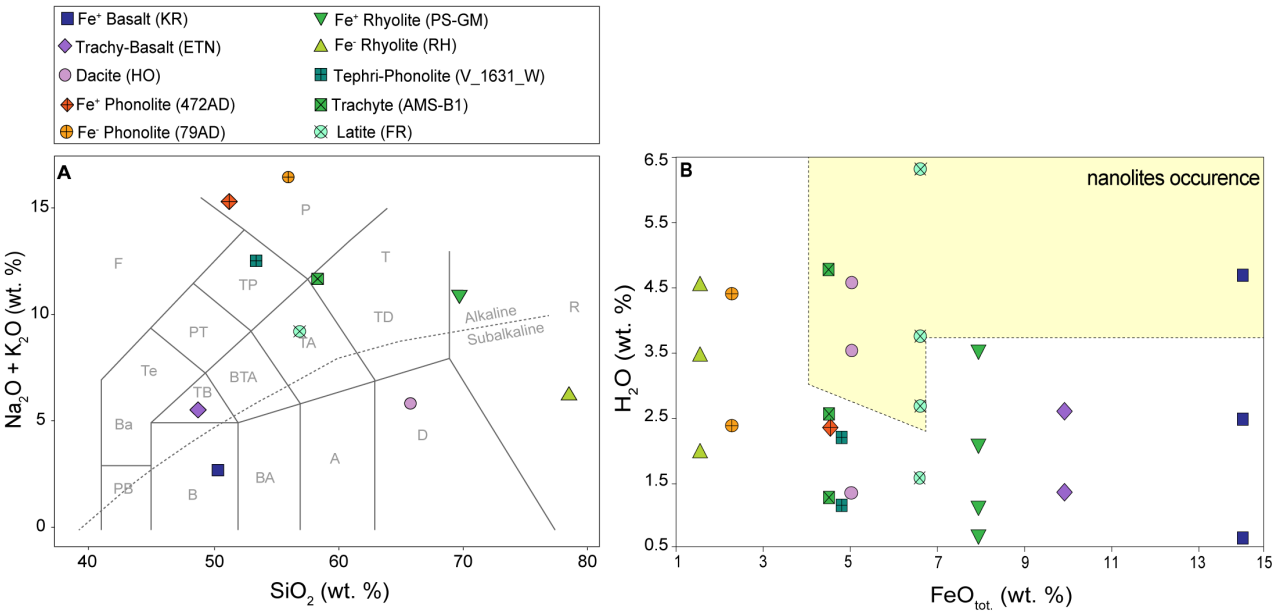

Figure. 1. A) TAS (total alkali versus silica) diagram showing the composition of samples used in this work. KR and HO glasses were synthesized in this study, while all other glasses were previously synthesized (see Table 1 for samples reference). Abbreviations in the plot mean: PB - picrobasalt, B - basalt, BA - basaltic andesite, A - andesite, D - dacite, R - rhyolite, TB - trachybasalt, BTA - basaltic trachyandesite, TA - trachyandesite, TD - trachydacite, T - trachyte, Ba - basanite, Te - tephrite, PT - phonotephrite, TP - tephriphonolite, P - phonolite, F - foidite. B) Samples water content (wt%) as a function of FeOtot. (wt%). The shaded area shows the occurrence of iron-bearing nanolites in some of the investigated samples (see text for a detailed discussion). The sample water content is reported in Table 2.

2.2. Samples synthesized in this study

In addition to the samples from literature, two anhydrous glasses belonging to the calcalkaline magma series were produced starting from: i) a basalt (KR) from the 1984 lava flow at Krafla volcano (Iceland; Tryggvason, 1986); ii) a dacite (HO) from AD 1707 Hoei eruption at Mt. Fuji (Japan; Miyaji et al., 2011). The rocks were melted in a thin-walled Pt crucible using a Nabertherm $MoSi_2$ box furnace at 1400 °C for 5 h and rapidly quenched in air. Glass chips from KR and HO samples were separately loaded into a $Pt_{80}Rh_{20}$ crucible. A concentric cylinder assembly was used to chemically homogenize the samples and remove bubbles from the melts.

Samples were continuously stirred at 1 atm from 4 h to 1 day at 1400 °C until the melt was free of bubbles and completely homogenized. Afterwards, the sample was rapidly quenched by immerging the crucible in water. The obtained glasses were chemically characterized and prepared for hydrous synthesis. Chemical compositions were measured with a Cameca SX100 electron micro probe analyser (EMPA) using a defocused beam (10-μm) to minimise alkali loss. Analyses were carried out at 15 kV acceleration voltage and 5 nA beam current. Wollastonite (Ca, Si), periclase (Mg), hematite (Fe), corundum (Al), natural orthoclase (K), and albite (Na) were used as standards. Additionally, a matrix correction was performed according to Pouchou and Pichoir (1991). The precision was better than 2.5% for all analyzed elements. The chemical homogeneity of glasses was verified by performing ~25 chemical analyses for each sample.

In order to obtain water-bearing glasses, anhydrous glasses from KR and HO, together with the iron-poor rhyolite RH (Di Genova et al. 2017b), were powdered and sieved to obtain two powder fractions with grain sizes of 200–500 μm and < 200 μm. Afterwards, powders were loaded into AuPd capsules (3 mm outer diameter, 10 mm lengths, 0.2 mm wall thickness) with a weight ratio of 1:1 to minimize the pore volume together with the appropriate amount of doubly distilled water.

Syntheses were performed at 260 MPa and at 1250 °C for 3 days in an internally heated gas pressure vessel (IHPV) at the Institute of Mineralogy at the University of Göttingen using the drop-fast quench technique. Samples were placed in the furnace hot zone through a platinum wire. At the end of the experiment, the wire was melted with a sudden D.C. current and samples were quenched rapidly in the cold part of the vessel. Each capsule was weighted before and after the experiment to test for possible leakage. The obtained glasses were free of bubbles and crystals at the micro-scale. Each composition was nominally hydrated with three different water contents of ~1, ~3, and ~4.5 wt%. Dissolved water content in glasses was measured using the Fourier Transform Infrared (FTIR) spectroscopy technique and thermogravimetric analysis (TGA). We used a Bruker Vertex 70 spectrometer coupled with an IR Microscope Hyperion 3000 at the Institute of Mineralogy at the University of Göttingen. For NIR analyses, each sample was double-polished below ~ 400 μm thickness measured using a Mitutoyo instrument (error of 2 μm). The densities of the water-bearing glasses were calculated after Lange and Carmichael (1987). The Lambert-Beer law was used to determine the sample water content (Stolper, 1982) using the NIR and MIR spectra (see the Supplementary materials section and Table S1 for measurements details). Thermogravimetric analyses were performed using a Setaram™ TGA 92 instrument at the Institute of Mineralogy at the University of Göttingen. Between 10 and 20 mg of coarsely powdered glass was loaded into a Pt crucible (4 mm diameter, 10 mm height) covered with a Pt lid. The sample was heated from

ambient temperature at 10 °C/min up to 1200 °C. After a dwell time of 30 min, the sample was cooled at 30 °C/min to room temperature. During the entire analysis, the sample weight loss was continuously recorded. To account for buoyancy changes with temperature of the sample and therefore correct the measured sample weight loss, a subsequent heating and cooling cycle was performed with the degassed sample (Schmidt and Behrens, 2008). For each sample, three thermogravimetric analyses were performed.

2.3. Raman spectroscopy

Raman spectra were acquired with two different Raman instruments available at the Mineralogical State Collection of Munich (SNSB, Horiba XploRa-Raman-System) and Department of Science at Roma Tre University (Horiba LabRam HR 800) hereafter termed M and R spectrometers, respectively. For each sample, 10 spectra were acquired to investigate the experimental reproducibly of the results. The instruments are equipped with an attenuated doubled Nd3:YAG laser having a wavelength of 532 nm and a microscope. The laser power on the sample surface was measured to be 7.15 mW (M spectrometer) and 11 mW (R spectrometer) through a 100Å~ objective and ~5 μm2 spot size. The instruments were calibrated using a silicon standard.

Instrumental settings consisted of 1800 grooves/mm grating density, confocal hole of 300 μm and slit of 200 μm with an exposure time of 60 s (3 times). The backscattered Raman radiation was collected on a polished sample surface over a range from 100 to 1500 cm^{-1} and from 2700 to 4000 cm^{-1} hereafter defined as the low-wavenumber (LW) and high-wavenumber (HW) regions respectively. In total, the M spectrometer required 6 min to acquire both LW and HW regions, while for the R spectrometer 26 min were necessary. Raman signal was found to be maximized at 6 μm of depth using a motor on the Z-axis. Therefore, spectra were collected at the same depth for all samples. Prior the Raman spectra acquisition, the samples were stored at 100 °C in an oven to avoid water absorption on the surface.

3. Raman spectra treatment

Raman spectra intensity were corrected for the frequency-dependence scattering intensity and temperature (Long, 1977; Neuville and Mysen, 1996) as it follows:

$$2)\ I = I_{obs}\left\{v_0^3 \cdot v \cdot \frac{\left[1-exp\left(-\frac{hcv}{kT}\right)\right]}{(v_0-v)^4}\right\}$$

where I_{obs} is the Raman spectra intensity, ν_0 is the wavenumber of the incident laser light (107/532 cm^{-1} for the green laser), ν is the measured wavenumber in cm^{-1}, h is the Planck constant (6.62607 Å~10 − 34 J s), c is the speed of light (2.9979 Å~ 1010 cm s^{-1}), k is the Boltzmann constant (1.38065 Å~ 10 − 23 J K^{-1}) and T the absolute temperature. Several procedures have been proposed to remove the spectra background (e.g., Behrens et al., 2006; Le Losq et al., 2012) with the aim to provide a general and chemically independent model to estimate the water content. Here, Matlab© and R codes were developed to fully automatize the background subtraction procedure (see Supplementary materials for the Matlab© code).

We followed two different approaches to determine the spectra background in the LW region: the SiO_2-dependent procedure provided by Le Losq et al. (2012) and a compositionally independent strategy (this study). The background subtraction procedure from Le Losq et al. (2012) relies on the definition of a set of zones devoid of peaks (Background Interpolation Regions, BIRs) to constrain the baseline. Specifically, in the silicate region (100 –1 500 cm^{-1}, LW), the number and wavelength interval of BIRs depend on the SiO_2 content, while in the water region (2700 – 4000 cm^{-1}, HW) two BIRs are maintained constant regardless of the composition. The results showed that the independently measured water content correlates linearly with the ratio between the LW and the HW band areas. In this work, we explored the possibility to extend this strategy to a wide range of naturally-occurring iron-bearing glasses with different iron oxidation state. Furthermore, we tested a baseline subtraction procedure based on a single cubic spline fitting independent on the chemical composition (Di Genova et al., 2015). With this, we aim to provide a simple and reproducible procedure to estimate the baseline of iron-bearing glasses, which are characterized by a substantial spectral variability and fluorescence (see Results section) due to the effect of the iron content, its oxidation state, and the presence of iron-bearing nanolites on Raman spectra. This would help when analyzing samples with unknown chemical composition, namely small melt inclusions trapped in crystals. By using Raman spectra, this study provides best procedures to both estimate water content of natural glasses and recognize iron nanolites.

4. Results

The measured chemical compositions of anhydrous glasses from this study (KR, HO) and samples from previous studies are listed in Table 1. Samples are also shown in a TAS diagram (Fig. 1A). Overall, SiO_2 content spans from ~48 to ~79 wt.%, with Na_2O+K_2O between ~2.8 and ~16.5 wt.%, FeO_{tot}. and H_2O up to ~14 and 4.53 wt.%, respectively (Fig. 1B). The Table S1 (Supplemetary Material 1) shows the water content measured by FTIR for samples synthesized in this study, while in Table 2 the TGA results obtained from the same samples. Furthermore, estimations from previous studies are reported for the other samples are listed. For the iron-poor rhyolite (RH) and dacite (HO), the water content was estimated using the peak intensity of the 4500 and 5200 cm^{-1} (Table S1, Fig. S1.1A, B) attributed to the combination of stretching and bending of OH groups bonded to tetrahedral cations and to the combination of stretching and bending modes of H_2O molecules, respectively. A linear baseline was applied to the RH and OH spectra (Fig. S1.1A). For the RH and HO samples, we used the linear molar adsorption coefficients given by Ohlhorst et al. (2001) and Withers and Behrens (1999), respectively (details are reported in the Supplementary materials 1). The KR basalt was opaque at thickness compatible with the analyses in the NIR range due to its high iron content (12.79 wt.%) which hindered the water quantification. The KR spectra displayed a broad band at ~5700 cm^{-1} which is attributed to crystal field transitions of iron (Ohlhorst et al., 2001) and, possibly, to the presence of iron-bearing nanolites. Therefore, for this composition, we used the band at 3550 cm^{-1} (MIR) to determine the amount of dissolved water in glasses.

A linear baseline was applied to evaluate the peak height together with the adsorption coefficient given by Stolper (1982) (Supplementary materials 1 and Fig. S1.1B). Concerning the TGA analysis of hydrous samples, it must be noted that for the iron-rich samples such as the KR series, the H_2O content may be underestimated due to the iron oxidation during the high temperature extraction of water by releasing H_2 instead of H_2O. Assuming initial extremely reduced conditions and, therefore, the iron only existing in a reduced state (Fe^{2+}), we calculated that the water concentration would be underestimated to a maximum of 0.8 wt.% for the KR3 sample (H_2O = 4.67 wt%). However, the IHPV used for the sample hydration is about 3 log units above the Ni-NiO buffer and a significant fraction of Fe^{3+} is expected. Therefore, we estimated that the water content may be underestimated to a maximum of ~0.25 wt% (see Schmidt and Behrens, 2008 for a detailed discussion).

The estimated water content for RH, HO, and KR samples using FTIR and TGA agrees within ~10% (Tables 2 and S1 for TGA and FTIR results, respectively). In the following, we consider the water content estimated via TGA.

Table 2

Measured and estimated samples water content of nanolite-free samples (chemical composition in Table 1). For both spectrometers (M and R), the calculated HW/LW ratio, *m* coefficient (Eq. 4) and estimated water contents are reported.

			M spectrometer						R spectrometer				
Sample	Composition	H_2O (wt.%)	HW/LW[a]	std. dev.	H_2O[b]	m[c]	H_2O[d]	H_2O[e]	HW/LW[a]	std. dev.	m[c]	H_2O[d]	H_2O[e]
KR1	Fe^+ Basalt	0.60	0.33	0.02	0.68	2.04	0.68	0.67	0.38	0.05	1.83	0.69	0.76
KR2[g]	Fe^+ Basalt	2.44	1.19	0.02	-	2.04	2.42	2.40	1.32	0.06	1.83	2.42	2.66
KR3[f]	Fe^+ Basalt	4.67	1.88	0.02	-	-	-	-	1.43	0.09	-	-	-
HO1[g]	Dacite	1.36	0.97	0.04	-	1.40	1.36	1.12	0.95	0.04	1.44	1.36	1.08
HO2[g]	Dacite	3.54	2.79	0.11	-	-	-	-	2.24	0.05	-	-	-
HO3[g]	Dacite	4.58	3.82	0.14	-	-	-	-	3.10	0.11	-	-	-
RH1	Fe^- Rhyolite	1.97	3.20	0.13	1.76	0.66	2.11	2.60	2.54	0.07	0.72	1.84	2.07
RH2	Fe^- Rhyolite	3.45	5.04	0.12	3.21	0.66	3.32	4.09	4.67	0.05	0.72	3.38	3.79
RH3	Fe^- Rhyolite	4.53	6.91	0.20	4.73	0.66	4.56	5.61	6.40	0.04	0.72	4.63	5.20
ETN1	Trachy-basalt	1.37	0.88	0.02	1.28	1.78	1.57	1.43	0.88	0.02	1.63	1.44	1.42
ETN2[g]	Trachy-basalt	2.61	1.39	0.06	-	1.78	2.48	2.25	1.57	0.07	1.63	2.57	2.55
LAT1[g]	Latite	1.59	1.05	0.03	-	1.51	1.59	1.37	-	-	-	-	-
LAT2[g]	Latite	2.69	1.43	0.04	-	-	-	-	-	-	-	-	-
LAT3[g]	Latite	3.76	2.46	0.10	-	-	-	-	-	-	-	-	-
LAT4[g]	Latite	6.32	7.34	0.95	-	-	-	-	-	-	-	-	-
AMS1	Trachyte	1.29	1.41	0.09	1.40	0.90	1.27	1.55	1.23	0.02	1.02	1.26	1.35
AMS2	Trachyte	2.57	2.85	0.10	2.46	0.90	2.58	3.13	2.52	0.06	1.02	2.58	2.77
AMS3[g]	Trachyte	4.78	3.63	0.04	-	-	-	-	-	-	-	-	-
PS-GM0.5	Fe^+ Rhyolite	0.72	0.74	0.02	0.77	1.32	0.98	1.06	0.62	0.03	1.38	0.85	0.88
PS-GM1	Fe^+ Rhyolite	1.16	1.08	0.01	1.18	1.32	1.43	1.55	0.92	0.01	1.38	1.27	1.31
PS-GM2	Fe^+ Rhyolite	2.11	1.70	0.02	1.96	1.32	2.24	2.43	1.48	0.02	1.38	2.03	2.11
PS-GM3.5[g]	Fe^+ Rhyolite	3.55	2.48	0.06	-	1.32	3.27	3.54	2.56	0.05	1.38	3.53	3.65
V_1631_1	Tephri-fonolite	1.17	1.58	0.02	1.50	1.00	1.59	1.78	1.29	0.07	1.22	1.57	1.45
V_1631_2	Tephri-fonolite	3.07	2.90	0.04	3.10	1.00	2.91	3.26	2.41	0.16	1.22	2.94	2.71
V_1631_3[g]	Tephri-fonolite	3.32	3.24	0.04	-	1.00	3.26	3.58	2.63	0.10	1.22	3.21	2.96
79AD1	Fe^- Phonolite	2.39	-	-	-	-	-	-	2.11	0.07	0.96	2.03	1.85
79AD2	Fe^- Phonolite	4.41	-	-	-	-	-	-	4.74	0.06	0.96	4.57	4.18
472AD1	Fe^+ Phonolite	2.36	-	-	-	-	-	-	2.47	0.04	0.96	2.36	2.72
External sample	Trachyte	5.57	6.08	0.18	5.58	0.90	5.49	6.42	-	-	-	-	-

[a]Calculated area ratio between the water (HW) and silicate (LW) bands.

[b]Calculated water content using the HW band area and Eq. 3.

[c]Calculated linear coefficient *m* (Eq. 4).

[d]Calculated water content using the HW/LW ratio and Eq. 4.

[e]Calculated water content using the $FeO_{tot.}$ (wt. %) and equation 4 and 5.

[f]Nanolite-bearing samples.

[g]Sample alteration due to laser-induced heating (M spectrometer conditions, see discussion for details).

5. Discussion

5.1. Effect of the chemical composition, water content, and iron nanolites on Raman spectra

Fig. 2 shows the LW region of a selection of corrected (Eq. (2)) spectra from anhydrous glasses to highlight differences in Raman features due to the composition. Spectra with a different SiO_2 content were vertically superimposed and listed by increasing iron content from the bottom.

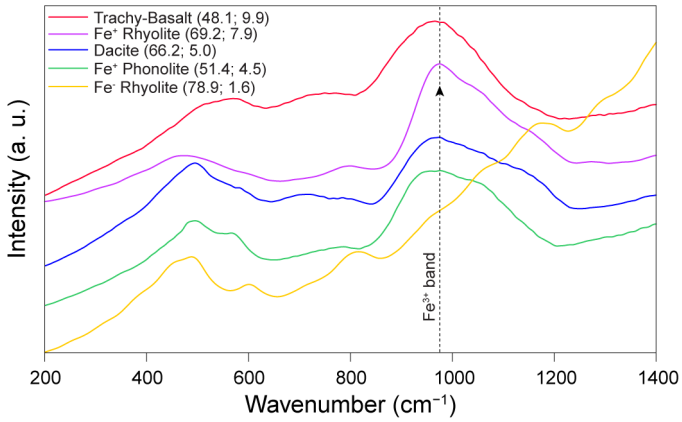

Figure 2. Raman spectra (LW region) of anhydrous glasses corrected for the excitation line and temperature (Eq. (2)) and normalized to the total area. Spectra were listed with increasing iron content from the bottom. The signal-background ratio is extremely low for the iron-poor rhyolite (RH). All the other spectra show higher signal-background ratio and a contribution at ~970 cm^{-1} (Fe^{3+} band). Fe^{+} and Fe^{-} in the legend indicate iron-rich and iron-poor compositions in Table 1, while numbers show the SiO_2 and iron content in wt%, respectively.

The most striking difference between spectra can be observed in the region around 1000 cm^{-1}. The iron-poor rhyolite (RH) exhibits the lowest signal to background ratio. At higher iron content, the signal to background ratio substantially increases. Moreover, excluding the iron-poor rhyolite (RH), all samples show a clear contribution at ~970 cm^{-1} in accordance with previous studies performed on iron-bearing multicomponent systems (Di Genova et al., 2015; Di Muro et al., 2009). The region below 700 cm^{-1} (Fig. 2) is attributed to T-O-T angle bending/rocking vibrations and tetrahedral O-Si-O bending vibrations (McMillan, 1984; Mysen et al., 1982). The broad band centered at ~500 cm^{-1} represents vibrational motions involving bridging oxygens associated with a wide range of T-O-T environments. This region originates from rings of tetrahedra connected in three-, four-, five-, six or higher-members (Bell et al., 1968; Galeener, 1982; McMillan, 1984; Mysen et al., 1982; Poe et al., 2001; Seifert et al., 1982; Sharma et al., 1981). The region between 800 and 1300 cm^{-1} results from T-O stretching vibrations and provides information on the

distribution of bridging oxygens and therewith on the degree of polymerization of the structure (Bell and Dean, 1972; Furukawa et al., 1981; McMillan, 1984; Mysen, 2003). Moreover, recent studies (Di Genova et al., 2017b; Di Muro et al., 2009) drew the attention to the effect of iron redox state on this region for anhydrous rhyolitic glasses. These studies reported direct correlations between the intensity of the band at 970 cm^{-1} with the $Fe^{3+}/Fe_{tot.}$ ratio of the glass. Di Genova et al. (2017b) showed that such a contribution 1) increased with the structure polymerization of the anhydrous glass and 2) disappeared in Raman spectra of iron-free rhyolites. Moreover, based on XANES spectra, Stabile et al. (2017) suggested that the Fe^{3+} is four-fold coordinated in these systems. According to these recent results, Di Genova et al. (2017b) named the ~970 cm^{-1} contribution of Raman spectra of rhyolites as "Fe^{3+} band". Here, looking at the hydrous iron-rich rhyolite spectra (Fe^{+} rhyolite, PS-GM series, $FeO_{tot.}$ =7.94 wt%, Fig. 3A), for which the $Fe^{3+}/Fe_{tot.}$ ratio is known (Di Genova et al., 2013), we observe that the Fe^{3+} band increases with increasing $Fe^{3+}/Fe_{tot.}$ ratio from 0.36 (PS-GM0.5, H_2O = 0.72 wt%) to 0.56 (PS-GM3.5, H_2O = 3.55 wt%). This agrees with previous observations from anhydrous samples (Di Genova et al., 2017; Di Muro et al., 2009). Furthermore, with increasing water content, the spectral contribution at 1060 cm^{-1} clearly decreases. This band may be assigned to symmetric stretching of tetrahedra with 3 bridging oxygens (Q3 species, Mysen et al., 1980; Zotov and Keppler, 1998). Therefore, for these samples, we suggest that the decrease of this band is directly related to the increase of water content depolymerizing the silicate structure (Zotov and Keppler, 1998). This would explain the measured decrease in viscosity (Di Genova et al., 2013) and glass transition temperature (Di Genova et al., 2014a) upon hydration for these samples although the oxidation state of the system increases with water and, therefore, an opposite behavior would be expected (Di Genova et al., 2017). However, in a multicomponent glass, the spectral contributions are not well resolved, and a systematic study based on spectra deconvolution is required to carefully address this aspect. Raman spectra of the iron-poor rhyolite (Fe^{-} rhyolite, RH series, $FeO_{tot.}$= 1.55 wt%, Fig. 3B) show a different behavior.

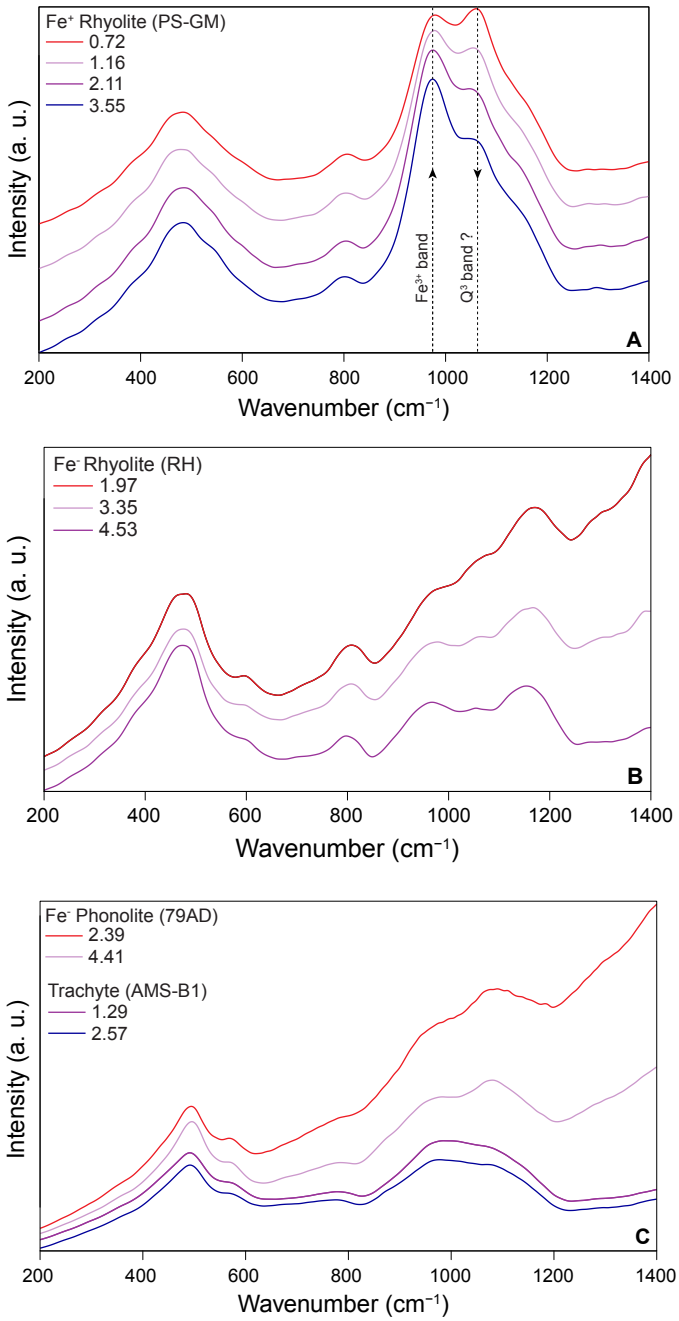

Figure 3. A) Corrected Raman spectra (LW region) of iron-rich rhyolitic series (PS-GM, SiO_2 =69.21 wt% and $FeO_{tot.}$ =7.94 wt%). With increasing water content, the Fe^{3+} band increases due to the increase of $Fe^{3+}/Fe_{tot.}$ ratio measured by Di Genova et al. (2013). Simultaneously, the band at 1060 cm^{-1} decreases possibly due to the structure depolymerisation (see text for discussion). Numbers in the legend show the dissolved water content in wt%. B) Corrected Raman spectra (LW region) of iron-poor rhyolitic series (RH, SiO_2= 78.87 wt% and $FeO_{tot.}$ =1.55 wt%). The spectra background decreases with increasing water content. Numbers in the legend show the dissolved water content in wt%. C) Corrected Raman spectra (LW region) of samples with ~57 wt% SiO_2 content. The iron-poor phonolite (79AD, FeOtot. = 2.26 wt%) shows a different spectra background depending on the dissolved water content (as observed in Fig. 5B). The trachyte, higher in $FeO_{tot.}$ content (4.51 wt%), shows a constant spectra background (as observed in panel A for the Fe^{+} rhyolite). Numbers in the legend show the dissolved water content in wt%.

Spectra are characterized by a high fluorescence, which decreases with increasing water content. To obtain a clear picture of the combined effect of iron and water on Raman features of glasses with different chemical compositions, a comparison between samples with lower SiO_2 content (~ 57 wt.%) is reported in Fig. 3C. Spectra from the phonolite (79AD) and trachyte (AMS-B1) with iron respectively equal to 2.26 and 4.51 wt.% were used. As observed for the Fe^{-} rhyolite (Fig. 3B), the iron-poor samples (Fe^{-} phonolite, 79AD series) display a background, which changes with water content. Conversely, the iron-rich spectra (trachyte, AMS-B1 series) are characterized by a constant background as showed before for the iron Fe^{+} rhyolite (Fig. 3A). Therefore, the amount of iron and its oxidation state (modulated by the water content) play a role in defining the variability of the spectra fluorescence of volcanic glasses. With increasing iron content (> 4.5 wt.%) we observed a substantial variation in the Raman features.

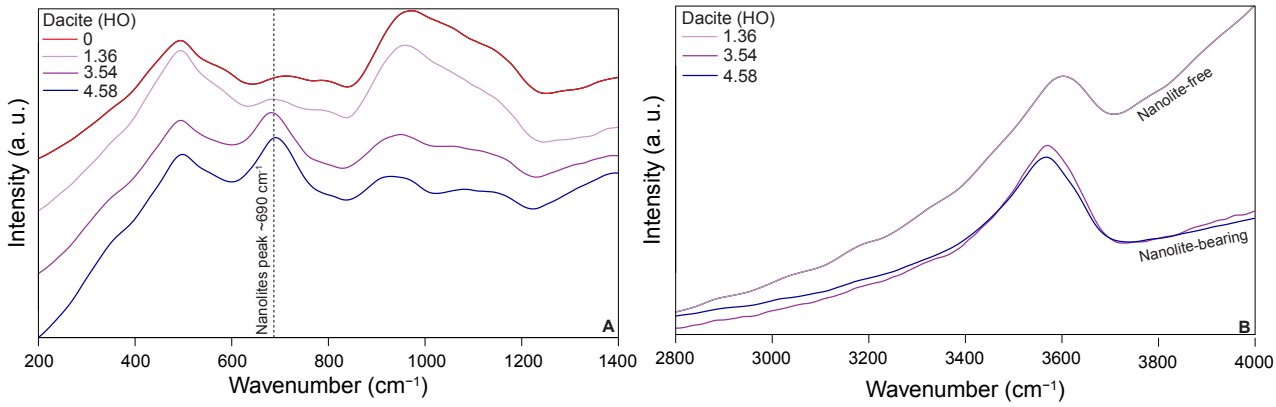

Figure 4. A) Corrected Raman spectra (LW region) of the dacitic series (HO, $FeO_{tot.}$= 5.02 wt%). With increasing water content, spectra show a peak at ~690 cm^{-1} due to the iron-bearing nanolites occurrence. Numbers in the legend show the dissolved water content in wt%. B) Corrected Raman spectra (HW region) of the dacitic series (HO, $FeO_{tot.}$= 5.02 wt%). Nanolite-bearing samples, characterized by a different water content (H_2O= 3.54 and 4.58 wt%), exhibit a similar band area. Numbers in the legend show the dissolved water content in wt%.

In Fig. 4A, B the LW and HW regions of dacitic spectra (HO series) are reported, respectively. With increasing water content (≥ 3.54 wt.%), the spectra show three main features: 1) the lowering of the silicate (LW) region area, 2) the development of a peak at ~ 690 cm^{-1} (Fig. 4A) and 3) no changes of the water band (HW) with water content (Fig. 4B). Analogous spectral signature was acknowledged by Di Muro et al. (2006a, 2006b) and Di Genova et al. (2017) for dacitic, trachytic and rhyolitic samples. Di Genova et al. (2017b) experimentally demonstrated that

both the quench from liquidus condition and the heating above the glass transition temperature induced the crystallization of iron oxides at the nanoscale. Here, the nanolite occurrence seems to be related to the high element diffusivity due to the extremely low-viscosity of hydrous melts at liquidus condition. Indeed, excluding the relatively viscous iron-rich rhyolite (PS-GM, see Di Genova et al., 2013 for viscosity measurements and comparisons with other compositions), samples with $FeO_{tot.}$ and H_2O respectively higher than ~ 4.5 and ~ 3 wt % crystallized nanolites.

Importantly, nanolites were present in our samples before the Raman measurements and were not detected during microprobe analyses. Therefore, we can exclude their occurrence induced by the laser heating of glasses. To confirm that, we performed high resolution SEM analyses on pristine samples that revealed the presence of whitish particles at the nanoscale (Fig. S2.1). This is in line with results reported by Di Genova et al. (2017b). There, magnetic-hysteresis analyses were performed on nanolite-bearing samples. Magnetite nanolites with diameters between ~ 5 nm to ~ 30 nm were detected. Therefore, our results demonstrate that Raman spectroscopy can also be used to show the presence of iron-bearing nanolites in volcanic glasses. This will help to reveal overlooked features in the glass matrix of experimental syntheses and natural rocks. Moreover, the presence of nuclei at the nanoscale can affect the onset of (heterogeneous) crystallization of other phases and degassing of volatiles during cooling and/or decompression and, ultimately, the magma rheology Di Genova et al. (2017b). Based on the documented effect of the chemical composition, oxygen fugacity and iron nanolites on Raman spectra, we reassessed the current methodologies to estimate the water content dissolved in volcanic glasses.

5.2 Quantification of the dissolved water content

5.2.1 Water content versus HW band area

The effect of increasing H_2O content on the HW band for nanolite-free and nanolite-bearing samples is shown in Fig. 5A, B for both spectrometers.

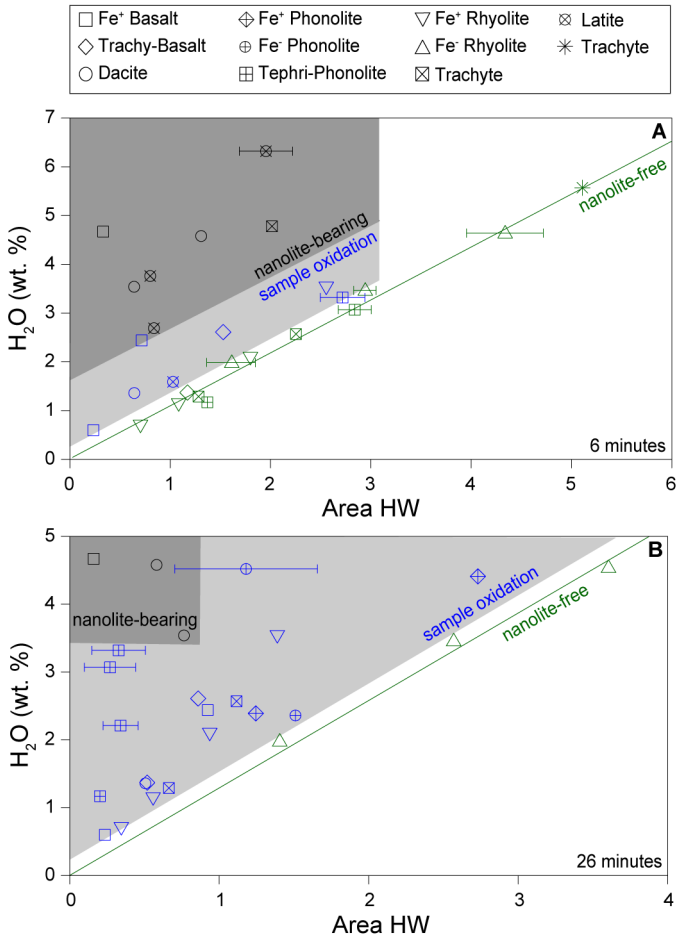

Figure 5. Area of the HW band for samples investigated in this study. Samples distribute in 3 different regions identified by sample colors: green symbols indicate nanolite-free samples, blue symbols represent nanolite-free samples that experienced surface oxidation during the analysis (light-grey area), while black symbols represent nanolite-bearing samples (dark-grey area). A linear relationship between the sample water content and HW area can be observed for nanolite-free samples which did not experience surface oxidation due to the acquisition timescale (see text for a detailed discussion). All nanolite-bearing samples deviate from the linear relationship. Band area has been divided by 10^5. A) Data from M spectrometer, total acquisition time 6 min (3 min for the LW region and 3 min for the HW region). The trachyte (* symbol, H_2O= 5.57 wt% external sample in Table 2) was used to validate the calibration. B) Data from R spectrometer (total acquisition time 26 min). Some samples were not measured with both spectrometers (see Table 2). (For interpretation of the references to color in this figure legend, the reader is referred to the web version of this article.)

For nanolite-free samples (green symbols), the HW area band linearly increases with

increasing water content. Therefore, for a single spectrometer, a (set of) glass standard(s) is sufficient to estimate the water content of unknown samples with different chemical composition. Importantly, spectra must be collected using the same experimental settings (see Materials and analytical methods section). However, for some nanolite-free samples, a deviation from linearity was observed (Fig. 5A, B). Looking at results from the M spectrometer (blue symbols, bright-grey area in Fig. 5A), where spectra were acquired in 6 min (LW + HW region), the iron-rich samples (KR and ETN basalts, FR latite and the PS-GM iron-rich rhyolite sample with maximum water content) exhibit a HW area lower than expected. Concerning the data from the R spectrometer (Fig. 5B), and except for the iron-poor rhyolitic series (RH), all the nanolite-free samples deviate from the linearity. The time necessary to acquire a single spectrum (LW + HW region) using the R spectrometer was 26 min, four times longer than the time needed when using the M spectrometer.

For these spectra, we clearly observed a change in the LW region. In fact, when comparing the spectra normalized to the region related to the T-O-T environment (~500 cm^{-1}), we observed that the spectra intensity increased at ~970 cm^{-1} (i.e. the Fe^{3+} band increased, Fig. S3.1). Furthermore, the intensity increased with the acquisition time suggesting that the laser heating induced the oxidation of the glass. We noted that this was particularly relevant for alkali-rich composition such as the tephriphonolite (Fig. S3.1). We explain the observed decrease of the HW area (Fig. 5A and B) with the degassing of dissolved H_2O through iron oxidation according to the following reaction: $H_2O + 2FeO = H_2+Fe_2O_3$ (Burgisser and Scaillet, 2007; Humphreys et al., 2015).

In order to avoid the sample oxidation and provide the best experimental conditions to estimate the water content, we performed several tests varying the laser power and/or the spectra acquisition time. By combining the results obtained from both spectrometers, we recommend a laser power of ≤ 5 mW on the sample surface and acquisition time of 5 min maximum (using the 100Å~ objective). For silica- poor and iron-rich hydrous (nanolite-free) systems (basalt, latite and, at lesser extent, Fe-rich rhyolite), the sample surface may oxidise within 6 min using a laser power of 7.15 mW on the sample surface. The sample oxidation results in the underestimation of the sample water content using the calibration based on the HW band area (i.e. external calibration).

Increasing the acquisition time and laser power (up to 26 min and 11 mW) this effect occurs regardless of the glass composition with the exception of the iron-poor rhyolite (RH). Nanolite-bearing samples differently deviate from the linear relationship observed in Fig. 5A, B depending on the sample composition. The HW area of nanolites-bearing samples is lower than expected for a given water content (Fig. 4B). This might be related to a decrease in the analyzed hydrous glass volume due to the presence of nanolites. However, since the effect of nanolites on the water

estimation using standard techniques is unknown, more studies are required to investigate their effect on KFT, TGA and NIR analyses. Therefore, the estimation of the sample water content based on the comparison of the HW band area (Fig. 5A, B) must be used only for nanolite-free samples where sample oxidation did not occur. For the M spectrometer, we derived the linear relationship between the HW and the water content as it follows:

3) $H_2O\ (\text{wt\%}) = 1.092 \cdot 10^{-5} \cdot HW$

where HW represents the water band area of Long-corrected spectra (Eq. (2)). It must be noted that this relationship is valid for the M spectrometer using the experimental conditions reported in Section 2.4. We recommend that laboratories develop a specific calibration applicable to their instrument, measuring condition and spectra treatment procedure. A spectrum from a trachyte with H_2O =5.57 wt.% estimated by KFT ("external sample" Table 2) was acquired. Using the Eq. (3), we estimated the water content equal to 5.58 wt%. Therefore, over a large interval of composition, a linear relationship between the HW band area and the water content can be used to estimate the water content provided that the sample surface does not oxidize during the spectra acquisition.

5.2.2 Water content versus HW/LW band area ratio

For a given sample, the HW/LW band ratio depends on the procedure employed for background subtraction in the LW region. Fig. 6A, B, C show the background subtraction procedure following Le Losq et al. (2012) and the protocol used in this study.

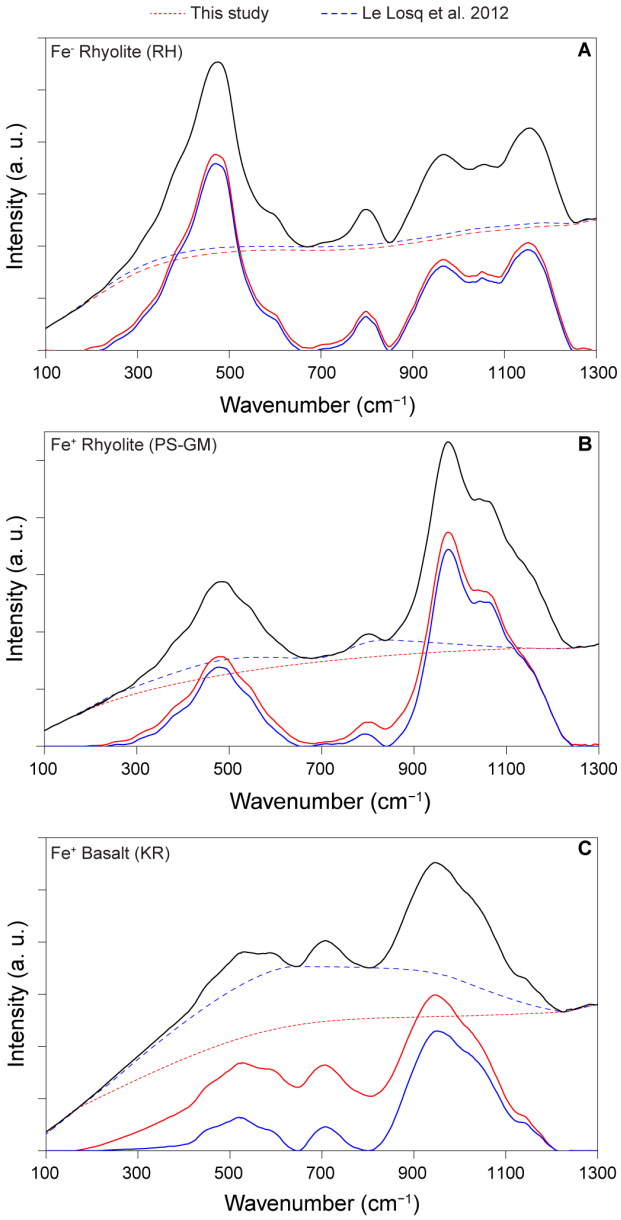

Figure 6. Corrected Raman spectra of A) Fe^{-} rhyolite (RH3), B) Fe^{+} rhyolite (PS-GM3) and C) Fe^{+} basalt (KR2). Blue and red dashed lines represent the baseline according to the procedure reported in Le Losq et al. (2012) and this study, respectively. Baselines substantially diverge for SiO_2-poor samples resulting in a different LW band area. (For interpretation of the references to color in this figure legend, the reader is referred to the web version of this article.)

Nanolite-bearing samples were not compared as the intermediate Raman region (640–740 cm^{-1}) is heavily affected by the spectral signature of nanolites (Fig. 4A) and, therefore, the background could not be assessed following the Le Losq et al. (2012) model. While for SiO_2-rich systems (Fig. 6A, B) both procedures returned similar results, for SiO_2-poor systems (Fig. 6C) the baseline strategies resulted in different spectra and, therefore, different LW areas for the same sample. This agrees with that reported by Le Losq et al. (2012). We estimated the dissolved water content of our glasses using the Le Losq et al. (2012) model.

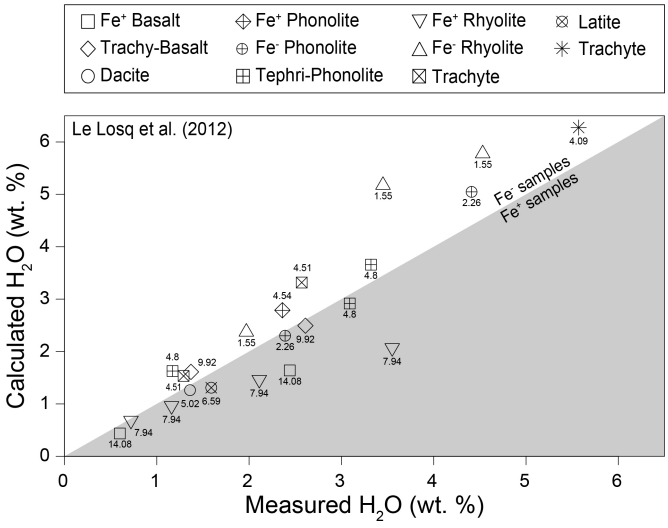

Figure 7. Calculated (after Le Losq et al., 2012) versus measured water content. Numbers show the sample FeO_{tot}. content in wt%. The model overestimates and underestimates the water content of iron-poor and iron-rich samples, respectively. All samples are nanolitefree.

The measured water contents versus model predictions are given in Fig. 7. The RMSE of the model prediction is 0.68 wt.%, which decreases to 0.32 wt.% if only samples with water content below 2 wt.% are considered. At H_2O > 2 wt.%, the model overestimates and underestimate the measured data for iron-poor and iron-rich samples, respectively. These results suggest that the A coefficient from Eq. (1) depends on the composition, especially on iron content. Our findings suggest that, although removing some of the chemical dependence (from SiO_2), the background procedure proposed by Le Losq et al. (2012) does not completely account for the composition of glasses with variable iron content and oxidation state.

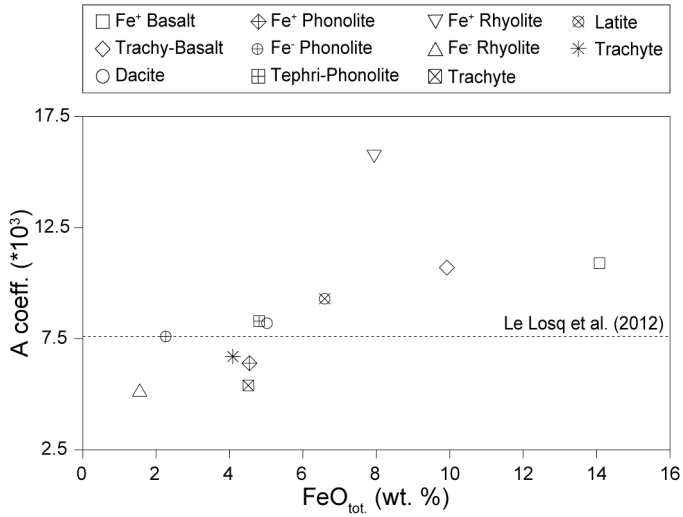

Figure 8. Calculated A coefficient (Eq. (1)) as a function of the sample iron content. The dashed line represents them value provided by the authors ($7.609 \cdot 10^{-3}$), considered independent of sample composition. Our results show that the coefficient increases with increasing iron content of the sample.

Fig. 8 shows the calculated A coefficient (Eq. (1)) for each nanolite-free sample series starting from spectra acquired using the M spectrometer. Iron-poor glasses ($FeO_{tot.}$ < 4.5 wt.%) exhibit a value slightly lower than the one provided by Le Losq et al. (2012). However, with increasing iron content, the coefficient increases up to $1.6 \cdot 10^{-2}$ (iron-rich rhyolite PS-GM, $FeO_{tot.}$ =9.55 wt.%). We interpret the increase of A with iron content as the result of the effect of iron, and its oxidation state, on Raman spectra which is known to be particularly important in SiO_2-rich systems (Di Genova et al., 2016a).

Since the modulation of the baseline based on the SiO_2 content cannot remove completely the chemical dependence of the water estimation procedure, we adopted a single criterion for the baseline assessment regardless of the sample composition. A cubic spline was applied between 50–200 and 1240–1500 cm^{-1} for the LW region and between 2750–3100 and 3750–3900 cm^{-1} for the HW region. With this protocol, the nanolite-bearing glasses could be included in the analysis as the wavelength intervals chosen to assign the baseline in the LW region are not affected by their spectral contribution (Fig. 4A).

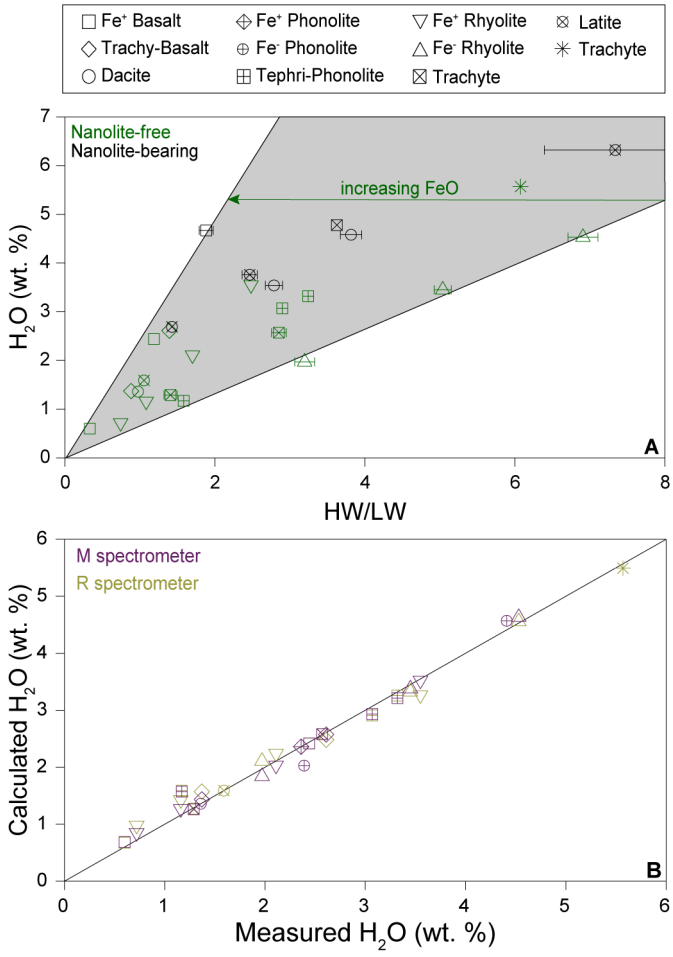

Figure 9. A) Data from M spectrometer. Sample water content versus the HW/LW band area ratio calculated following the baseline protocol reported in this study. For each sample series, a linear relationship is observed when nanolite-free samples (green symbols) are considered. Nanolite-bearing samples (black symbols) do not follow such a trend. B) Data from both spectrometers. Comparison between measured and calculated water contents using Eq. (4) and data from Table 2. (For interpretation of the references to colour in this figure legend, the reader is referred to the web version of this article.)

Fig. 9 shows the water content as a function of the HW/LW area ratio using the M spectrometer. For each sample series, a linear relationship passing through the origin (Eq. (4)) was adopted for nanolite-free samples (green symbols, Fig. 9A):

$$4)\ H_2O\ wt\% = \frac{HW}{LW} \cdot m$$

where *m* is the linear fit coefficient (Table 2). Samples that experienced surface oxidation (Fig. 5A, B) during measurements using both spectrometers follow the observed relationship meaning that the internal calibration removes, or minimises, such an effect. Conversely, the nanolite-bearing samples (black symbols in Fig. 9A) deviate from linear trends. However, for the dacitic series (HO) we observed the lowest deviation, while the latitic series highly deviates from the linearity. Therefore,

these samples were excluded from the calculation of the fit coefficient (m, Eq. (4)). The sample water content was estimated using the Eq. (4) and parameters in Table 2 with a RMSE of 0.17 and 0.15 wt % for the M and R spectrometer, respectively (Fig. 9B). The *m* coefficients reported in Table 2 can be used to retrieve the water content from Raman analyses whenever the chemical composition of the investigated sample is close to one of the samples used in this work.

We also investigated the possible chemical dependence of the fit parameter (m, Eq. (4)) in order to generalize our results. The Fig. 9 reveals that the fit parameter (*m*, Eq. (4)) shows a simple linear relationship with the iron content.

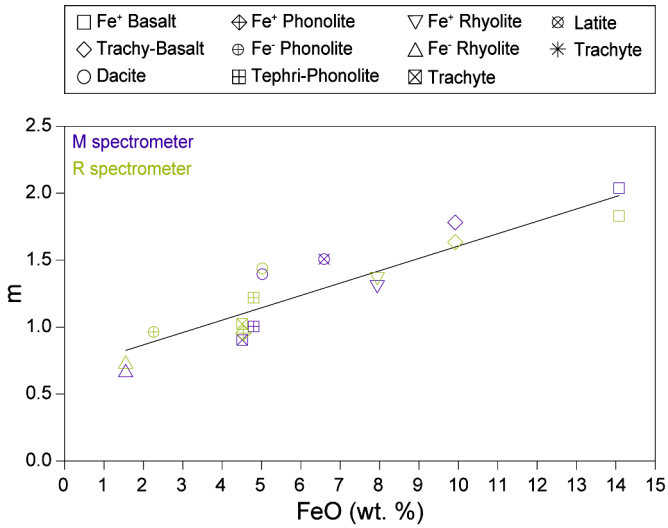

Figure 10. Iron dependence of the m coefficient (Eq. (4)) for nanolite-free samples. For both spectrometers, a linear trend can be observed. Estimated water content using calculated m (Eq. (5)) and Eq. (4) are reported in Table 2.

A linear trend was observed for all the samples and both spectrometers (Fig. 10) suggesting that instrumental effects are removed (or minimized) with this procedure. We parameterized the iron dependence of the m parameter in Eq. (4) as it follows:

5) $m = 0.096 \cdot FeO + 0.663$

where the FeO is the iron content in wt.%. We estimated the water content of nanolite-free samples with a RMSE of 0.47 wt.% for samples investigated with the M spectrometer and 0.29 wt.% for the R spectrometer. This procedure is intended to be used when samples have different iron content from the standard and a different m coefficient is expected. Moreover, in case the sample chemistry is unknown (i.e. small melt inclusions or in situ investigations), one may approximate the composition using the Raman spectrum (Di Genova et al., 2015, 2016b).

6. Conclusions

Here, we have shown how iron content, its oxidation state, and iron nanolites greatly affect Raman spectra of hydrous multicomponent glasses. Samples with composition spanning from basalt to rhyolite, including alkali- and iron-rich compositions, were used to explore and test procedures to estimate the water content of glasses through Raman spectroscopy. We recommend the following:

1) The sole water band area (HW, Fig. 5A, B) can be only used with nanolite-free samples regardless of the iron oxidation state of the glass. Sample and standard spectra must be acquired at the same depth (possibly at ~ 6 μm), instrumental conditions and using the same spectrometer.

Sample oxidation during spectra acquisition can easily occur, especially when analyzing iron- and alkali-rich samples. We found that 6 min of acquisition time and a laser power ~7 mW oxidized basaltic, dacitic, latitic, and iron-rich rhyolitic compositions, while ~ 5 mW are enough to alter alkali-rich (i.e. phonolite) sample. Increasing the acquisition time to ~ 26 min brings forth the oxidation for all samples excluding the calcalkaline rhyolite.

Since the glass oxidation depends on the sample composition, acquisition time, and employed experimental settings (i.e. objective and laser power), we suggest repeating Raman measurements on the same spot and look at the evolution, if any, of the peak at ~970 cm^{-1} (Fe^{3+} band) which increases with increasing the Fe^{3+} content of the glass. 2) The water to silicate band ratio (HW/LW, Fig. 9A) linearly correlates with the water content of the glass. This procedure works when using nanolite-free samples and, importantly, is not affected by sample oxidation. Some nanolite-bearing samples (e.g. dacite) also follow a quasi-linear trend. This procedure reduces instrumental effects. However, the slope (m, Eq. (4)) of the HW/LW ratio versus H_2O content depends on the iron content. For both spectrometers, we observed a linear relationship between the m coefficient and the iron content. Therefore, following the spectra treatment presented in this study, a unique calibration based on the iron content of the sample can be used to estimate the water content.

Acknowledgments

This study was supported by the NSFGEO-NERC "Quantifying disequilibrium processes in basaltic volcanism" (reference: NE/N018567/ 1). S. Sicola was supported by a MIUR fellowship to Roma Tre University PhD School. L. Spina wish to thank the ERC Consolidator "CHRONOS" project (reference: 612776). We thank M. Kaliwoda, R. Hochleitner, and A. Pisello for Raman measurements at the Mineralogical State Collection Munich (SNSB), L. Melekhova for some EMPA analyses in Bristol, S. Lo Mastro and D. De Felicis for SEM analysis at LIME laboratory (Roma Tre University), and R. Cioni for providing Vesuvius hydrated glass samples (79AD and 472AD). We also thank two anonymous reviewers for their contribution to the peer review of this work and helpful comments that helped us to improve this manuscript.

Chapter 2

Bubbles vs. Pores: a rheological study

Note – In preparation for submission

Abstract: The presence of pores strongly controls the rheological behavior of magma and thus influences all volcanic processes (pre-syn and post-eruptive). Nevertheless, the effects of porosity on the rheology of magma are not well characterized, and a general parameterization is not available yet. Here we present a new set of experiments designed to investigate the rheology of porous melts at high temperature (750-800 °C), low strain rates (10^{-6}-10^{-7} s^{-1}) and variable porosity (10-50% vol.). Experiments were performed at 1 atm using Thermomechanical Analysis (TMA). The starting materials are 5 x 5 mm cores of natural rhyolitic obsidian from Krafla, Iceland (vesicle and crystal-free) initially containing 0.11(4) wt.% dissolved H_2O. Two steps compose the experimental procedure: 1) synthesis of bubble-bearing materials by heating and expansion due to foaming; 2) deformation of the foamed samples at different temperatures (750-800°C). During the first step, cores are heated above the glass transition temperature interval (900-1050° C) and held for set amounts of time (10–24 h); the volume of the foamed samples increases because H_2O vapor-filled bubbles nucleate and expand. In the second step, two different experimental strategies are employed: 1) *Single-stage*: samples are deformed directly after foaming. A constant load (150 g) is applied by silica or alumina probes to the core, and the cores deform isothermally for 5-20 hours. 2) *Double-stage*: deformation of the synthesized of pore-bearing cores occurs after the quench and a 15 days repose at room T. In both cases, the variation in length (displacement) and volume (porosity) is continuously recorded and used to calculate the viscosity of the foamed cores using Gent's equations. Results suggest that single-stage measurements yield a lower effect of bubbles on the bulk viscosity, compared to double-stage measurements. We suggest that the different behavior may be related to the nature of the pores (vapor-filled/empty) and/or the different microstructure of the experimental materials.

1. Introduction

As magma rises through a volcanic conduit toward Earth's surface, nucleation and growth of gas bubbles occur by exsolution of volatiles, initially dissolved in magma at high pressure (Liu et al., 2000, Martel et al., 2001). Both dissolved and exsolved volatiles strongly affect the rheology of natural silicate melts during the eruption and during transport and emplacement. While the viscous behavior of single phase melts (with dissolved volatiles) is relatively well known, the effect of bubbles (i.e., exsolved volatiles) on the rheological properties of magmas is not well understood.

Several experimental studies have been conducted with different approaches (theoretical/numerical, empirical on analogues, empirical on natural material, Fig.1) in order to analyze the relationship between porosity and viscosity in silicate melts, varying adjustable parameters as porosity, temperature, stress, strain rates, capillary number (e.g. Rahaman et al., 1987; Webb and Dingwell, 1990; Bagdassarov and Dingwell, 1992; Lejeune et al., 1999; Stein and Spera, 2002; Pal, 2003; Rust et al., 2003 Llewellin and Manga 2005; Quane and Russell, 2005; Robert et al., 2008; Quane et al., 2009; Heap et al., 2014; Vona et al., 2016). Theoretical models (Fig.1a) highlight a wide range of behaviors in the viscosity vs. porosity relationship; while a large range of them predicts a rise in viscosity with increasing porosity; a comparable number predicts on the other hand a decrease in viscosity when porosity increases. Those studies consider the effect of bubbles on melt viscosity as a function of capillary number (Ca) in steady, simple-shearing flows. The capillary number is defined as $Ca = \lambda\,\dot{\gamma}$ where $\dot{\gamma}$ is the shear strain rate and λ is the bubble relaxation time. This number describes the relative importance of viscous stresses, able to deform bubbles and interfacial stresses. If Ca <1, interfacial tension forces dominate and bubbles are approximately spherical (e.g., Taylor, 1934) and they are also able to maintain their sfericity and deform the flow lines within the suspending medium, thus viscosity increases; if for Ca >1, viscous forces dominat, bubbles will be elongate (e.g. Hinch and Acrivos, 1980) providing free-slip surfaces within the suspending medium decreasing viscosity. Llewellin and Manga (2005) identified two flow regimes (based on the previous work of Pal, 2003 and Bagdassarov and Dinwgell, 1992). Llewellin et al. (2002; 2005) also introduced the concept of unsteady flow defined by the dynamic capillary number $\left(Cd = \lambda\frac{\ddot{\gamma}}{\dot{\gamma}}\right)$ which takes into account the rate of change of strain rate, namely the rate of change of shape of the elongated bubbles around their equilibrium deformation.

Empirical models (Fig.1b, c) include experimental data obtained using different rheometrical apparatus (compression or torsion) on a variety of materials (analogue or natural) and suspension configuration. As far as suspension configuration is regarded, the experiments were performed either on unconsolidated or sintered particles with interclast porosity (Rahaman et al., 1987;

Ducamp and Raj, 1989; Sura and Panda, 1990; Quane and Russell, 2005; Quane et al.; 2009) or on melt frameworks with distributed porosity (Bagdassarov and Dingwell, 1992, 1993; Lejeune et al., 1999; Stein and Spera, 2002). Very few experiments are based on natural materials (Bagdassarov and Dingwell, 1992; Quane et al., 2009; Heap et al., 2014, Vona et al., 2016). All the experimental data are in the regime of $Ca \geq 1$ (viscosity decreases as a function of porosity), and, within this regime they do not show consistent trends (Fig. 1b, c).

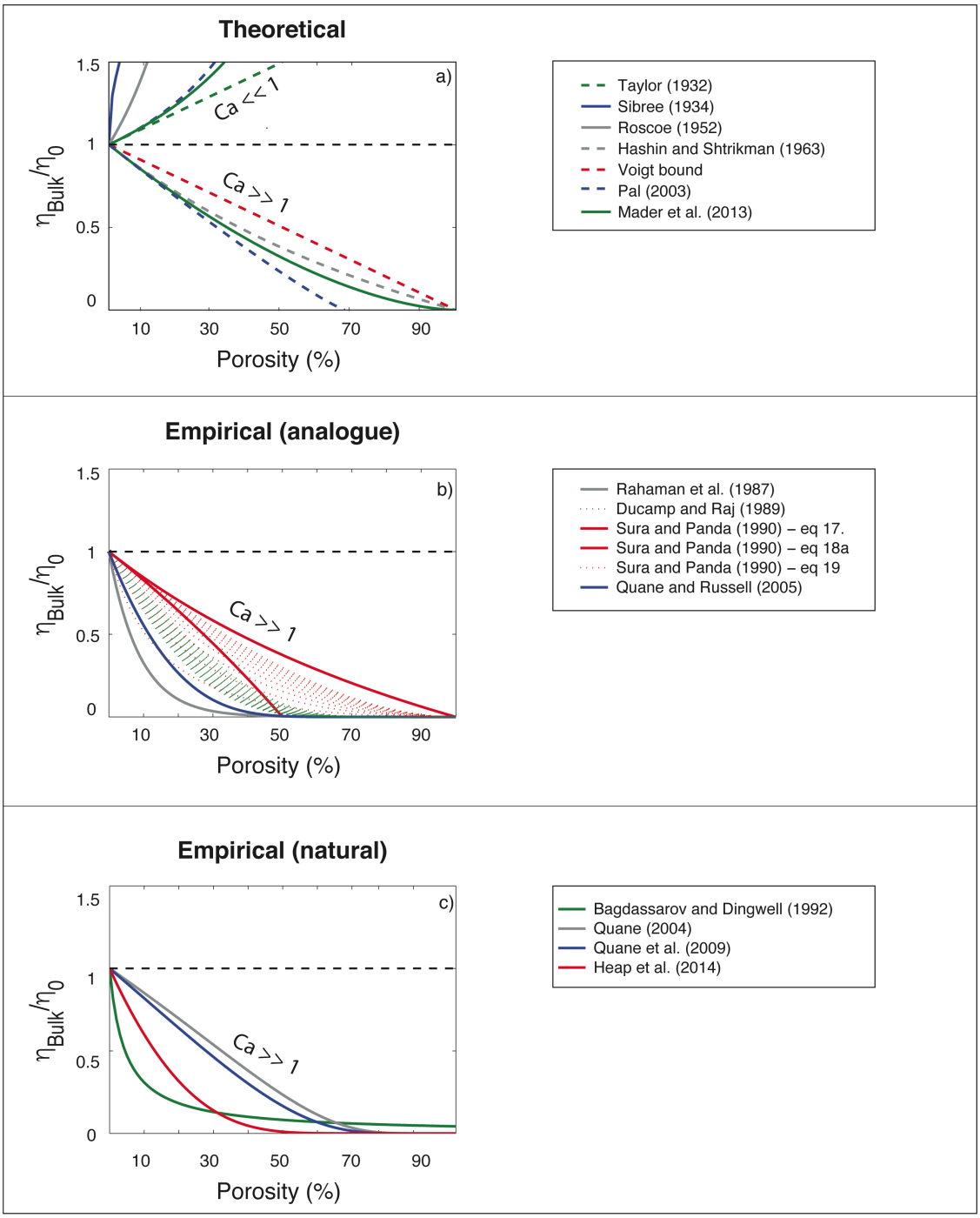

Figure1. Published models predicting the n_{bulk}/n_0 trend as a function of porosity a) Theroetical models. b) Empirical models on analogue materials. c) Empirical models on natural material. (Modified from Vona et al., 2016).

Given the paucity of experimental data on natural materials and the discrepancy among the different set of data and models, we decided to investigate the rheology of porous melts at Ca >1 with a new set of experiments especially designed to investigate the in situ high-temperature degassing and deformation process of natural rhyolites.

Experiments were performed at 1 atm using a Thermomechanical Analyzer (TMA) and the starting materials are 5 x 5 mm cores of natural rhyolitic obsidian from Krafla, Iceland (vesicle and crystal-free). The use of samples with those features is aimed at studying bubbles nucleation in silicic melts and exploring the rheology of natural bubble-rich magma. The experimental strategy involves two main phases: 1) Foaming phase and 2) Deformation phase.

Two different experimental strategies were employed: 1) *double-stage* (DS) in which the time between the foaming and the deformation phase is ~ 15 days 2) *single-stage* (SS) measurements, in which the deformation of the samples occurs directly after foaming. Mechanical data (load and displacement) were used to calculate the viscosity of the obsidian cores associated to their relative bubble content.

The two different methodologies were intended to reproduce two different volcanic scenarios: single-stage measurements are applicable to magma rising in the upper part of a conduit (constant high temperature conditions) whereas double-stage measurements should reproduce cooling and reheating of a lava flow or a dome. The present study allows to explore the effect of porosity on the viscosity of natural rhyolitic obsidian.

2. Starting material

The starting material is natural rhyolitic obsidian from Hrafntinnuhryggur, Krafla, Iceland, previously described and characterized by Tuffen and Castro (2009), Ryan et al. (2015a) and Vona et al. (2016). The starting material is essentially bubble and crystal free containing 0.11(4) wt.% H_2O (Ryan et al., 2015a). Cylindrical cores (5x5 mm) were drilled, trimmed, and the ends ground to make parallel polished end-surfaces.

Cores physical properties of obsidian cores were measured before experiment. Initial length (L_0), diameter (D_0) and volume (V_0) were determined using a digital caliper, mass (m_0) with a high-precision balance. Initial porosity (ϕ_0) is assumed equal to zero (below detection).

3. Experimental strategy

A set of 24 experiments has been performed using a Setaram Setsys vertical dilatometer (TMA) at Experimental Volcanology Lab (EVPLab) at Roma Tre University (Fig. 2). The device is composed by a heating chamber, where the sample is located and supported by an alumina base connected to a measuring head. Depending on experimental temperature, a silica (T < 975 °C) or alumina (T > 975°C) probe connected to a Linear Variable Displacement Transducer (LVDT) sits on the sample and monitors its length change (Fig. 2a). All experiments are conducted at atmospheric pressure and at oxygen fugacity fixed by continuous argon gas flux. The software Setsoft allows to set the experimental parameters (e.g. temperature, heating/cooling rate, probe weight, experiment time).

Classical dilatometric measurements (e.g., Webb and Dingwell, 1990; Gottsmann and Dingwell, 2001) involve the amount of the length change of the samples under controlled heating ramps to derive glass and melt thermal expansivity coefficients (linear, α_L and volumetric $\alpha_V = 3\alpha_L$). When these measurements are run in a vertical dilatometer, the probe weight is set equal to zero (i.e., an upwards force equal to the probe weight itself is applied) in order to avoid the probe effect on the sample expansion. On hydrous glasses, if the sample is hold at high T (above glass transition temperature, Tg) for sufficient time, the same set-up is able to investigate the water exsolution and foaming. A TMA device can also be used to measure sample viscosity; samples are deformed by applying a constant load and recording probe displacement during compression to derive material flow curves according to the parallel plate theory (e.g. Gent, 1960).

In the present study, we combined the two techniques (dilatometry and parallel plate) to investigate the rheology of bubble-bearing magmas as described in detail below. In particular, experiments in the vertical dilatometer device involved two steps (Fig. 2b): i) synthesis of bubble-bearing materials by heating and expansion due to foaming; ii) deformation of the foamed samples.

Prior to TMA experiments, obsidian glass transition temperature (Tg = 700 ° C ± 20° C) was measured by Differential Scanning Calorimetry (Netzsch DSC 404 Pegasus) at EVPLab Roma Tre University, in order to define the T range for foaming and deformation experiments (details are reported in the Supplementary Material 2).

The dwell times needed to reach equilibrium conditions were taken from Ryan et al. (2015a, 2015b) who conducted a series of high-temperature experiments on the same obsidian material in order to investigate water solubility in rhyolitic products. Each experiment had a prescribed dwell time ranging from 0.25 - 24 h at a constant temperature (900 - 1110 °C). In the adopted experimental approach the choice of T_{foam} and dwell time is based on water solubility experiments by Ryan et al. (2015a, 2015b).

The first experimental step in the dilatometer (i.e., foaming), involved heating obsidian cores at a rate of 5°C/min from room temperature to a target temperature above Tg (T_{foam} 900-1050 °C) and holding it at T_{foam} for set amounts of time (10 – 24 h) (Fig. 2b). As the temperature increases, the volume of the foaming samples increases, because H_2O vapor-filled bubbles nucleate and expand. After a given amount of time, exsolution and bubble growth ends as the equilibrium is reached.

In one case (experiment IK-13), a single test was performed in order to explore volatile exsolution and bubble growth kinetics; the sample expansion has been continuously monitored by leaving the probe on the sample surface during all the experimental time (see Section 3.1). For all other experiments, to avoid possible influence of the probe-sample interface on the degassing behavior and final sample geometry (e.g. non-isotropic expansion), the foaming step has been conducted by heating the sample without the probe on (see Tab. 1 for details).

Two different experimental strategies were employed, hereafter "*double-stage*" (DS; Fig. 2c) and "*single-stage*" (SS; Fig. 2d) experiments. *Double-stage* measurements involved deformation of foamed cores that have been previously synthesized and quenched (cooling rate 50 °C/min) in the same TMA apparatus. These experiments were conducted about 15 days after the foaming and quenching. The samples were re-heated to 750 °C and a constant load (150 g) was applied through the probe deforming the cores isothermally for 5 - 20 hours. At the experimental conditions (T_{def} = 750 °C, P = 1 bar), the melts are volatile undersaturated (Ryan et al., 2015a); therefore, no further H_2O exsolution and foaming takes place during deformation stage. *Single-stage* measurements involved deformation of the samples directly after foaming (without quenching). The samples were cooled down from T_{foam} = 900 - 950 °C to different target temperatures (T_{def} = 750 - 800 °C) always in order to obtain H_2O undersaturation conditions. After 1 hour at T_{def}, foamed cores were deformed under same applied load (150 g) and similar amount of time (5 - 20 hours) of *double-stage* measurements.

In both cases, the variation in length (i.e. displacement) during deformation phase was continuously recorded and used to calculate the viscosity of the foamed cores. However, while for *double-stage* measurements the foamed core geometry (i.e. Length, L_i, Diameter, D_i, Volume, V_i, Porosity ϕ_i) could be directly measured prior to deformation, for *single-stage* experiments the pre-deformation geometry needed to be calculated. Lowering the probe on the sample directly after the foaming stage allowed the measurement of the foamed sample height (i.e. Length, L_i), but no information was accessible on sample diameter (D_i). However, the analysis of pre-deformation foamed cores used for *double-stage* experiments indicated a 1:1 relationship between axial (L_i/L_0) and radial (D_i/D_0) strain (i.e. isotropic expansion) (Tab. 1, Fig. S2.2 in the Supplementary Materials

2). This relation allowed me to model and estimate the initial volume (V_i) and porosity (ϕ_i) for *single-stage* experiments (see Supplementary Materials 2 for calculations and associated uncertainties).

The samples showed a variable volume change during the foaming phase (V_i) even under the same experimental conditions, in response to a slightly heterogeneous water distribution in the natural obsidian samples. The final volume at the end of the experiment, either 'foaming' (V_i) or 'foaming + deformation' (V_f) was analyzed using a Micromeritics AccuPyc II 1340 helium pycnometer.

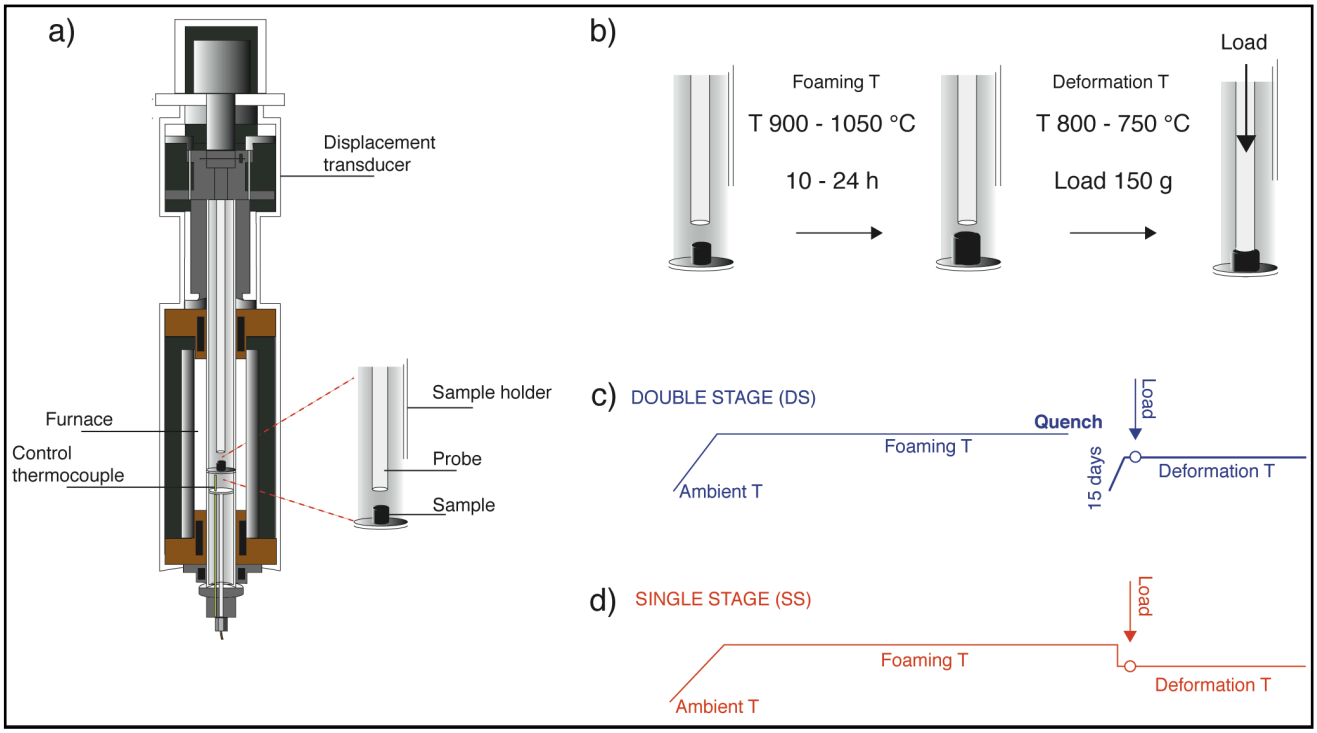

Figure 2. Sketch of the adopted setup. a) Setaram Setsys vertical dilatometer (TMA). b) Detail of the experimental setup used in the present study. c-d) Temperature time variation for double-stage (c) and single-stage (d) experiments.

Table1. Experimental properties and conditions of all the pre-foaming cores including: pre- foaming physical properties (L_0, m_0, d_0), volume (V_0) and density (ρ_0), foaming temperature (T_{foam}), dwell time (t), deformation temperature (T_{def}), The table summarizes the experimental approach: Single-stage (SS), Double-stage (DS) experimental type and the probe position.

SAMPLE	L_0 (mm)	m_0 (g)	D_0 (mm)	V_0 (mm^3)	ρ_0 (g/cm^3)	T_{foam} (°C)	t (h)	T_{def} (°C)	Type
IK-13	4.45	0.19	4.89	83.81	2.32	900	24	-	-
IK-11	5.14	0.22	4.89	96.35	2.33	950	10	-	-
IK-9	4.52	0.20	4.89	84.94	2.33	900	15	750	SS[a]
IK-7	5.84	0.26	4.90	110.06	2.35	900	24	750	SS[a]
IK-19	4.78	0.21	4.90	89.90	2.34	900	24	750	SS[a]
IK-32	5.36	0.24	4.91	101.37	2.36	900	24	750	SS[a]
IK-18	5.04	0.23	4.93	96.02	2.37	925	20	750	SS[a]
IK-25	4.98	0.22	4.92	94.77	2.36	925	20	750	SS[a]
IK-20	5.04	0.22	4.89	94.79	2.36	950	10	750	SS[a]
IK-30	5.24	0.23	4.94	100.22	2.28	950	10	750	SS[a]
IK-6	4.64	0.21	4.89	87.34	2.35	900	24	800	SS[a]
IK-23	5.02	0.23	4.93	95.58	2.37	900	24	800	SS[a]
IK-21	5.14	0.23	4.93	98.02	2.36	925	20	800	SS[a]
IK-26	4.98	0.22	4.93	94.83	2.34	950	2	800	SS[a]
IK-28	4.98	0.22	4.92	94.77	2.36	950	2.5	800	SS[a]
IK-27	5.09	0.23	4.93	97.17	2.36	950	4	800	SS[a]
IK-10	4.60	0.20	4.89	86.20	2.35	950	10	800	SS[a]
IK-22	4.99	0.22	4.92	94.77	2.36	950	10	800	SS[a]
IK-17	5.21	0.23	4.90	98.39	2.34	900	24	750	DS[b]
IK-16	5.17	0.23	4.91	98.06	2.35	925	20	750	DS[b]
IK-15	5.08	0.23	4.92	96.64	2.37	950	10	750	DS[b]
IK-36	5.10	0.23	4.92	96.99	2.33	975	6	750	DS[b]
IK- 35	5.01	0.22	4.92	95.33	2.35	1000	5	750	DS[b]
IK-37	5.06	0.23	4.92	96.35	2.35	1050	4	750	DS[b]

Notes: [a] The sample is deformed after foaming (without quenching). [b] Deformation involved previously synthesized and quenched foamed cores. [c] The probe is on the surface sample for the whole experiment (from foaming to deformation stage). [d] The probe is lowered during the deformation phase.

4. Results

4.1. Timescales of degassing process

During foaming experiments, the volume increase (ΔV) due to gas exsolution and foaming is manifested by a systematic increase in sample height (i.e. displacement, ΔL) with increasing dwell time (t) until a maximum stable value is reached (Fig. 3a and Table 1). The rate of change of sample volume (dV/dt) and the time to achieve the equilibrium plateau depends on T_{foam}.

The considered dissolved water is 0.11(4) wt.% in pre-run cores, was given by Tuffen and Castro (2009); they reported (based on synchrotron Fourier transform infrared spectroscopy, FTIR analysis) that the H_2O contents across the outcropping of Hrafntinnuhryggur obsidian varied from 0.11– 0.37 wt.%. The starting glass material is texturally isotropic and homogeneous except for minor occurrences of cryptic flow-banding, and is essentially bubble- and crystal-free (Ryan et al., 2015a).

In order to monitor dissolved/exsolved water content in both pre- and post-run products further analyses using Raman spectroscopy were performed. Unfortunately the initial dissolved

water content (0.11 wt.%) is below Raman detection limit (~ 0.5 wt.%) and no water was therefore detected by Raman spectroscopy. Despite that, Raman measurements provided useful information about samples silicate glass structure before and after the experiment; indeed the comparison between the LW part of the spectra (silicate region) of pre- and post-run cores proved that no crystallization happened from the heating to the cooling stages (see Chapter 1 for details). During the cooling phase other factors could affect water exsolved in bubbles, like H_2O resorption (see Chapert 3 for a more detailed explanation). This process occurs when the cooling rate is sufficiently slow to enhance the "return" of exsolved water in the melt. In the designed experimental method the cooling rate from T_{foam} to T_{def} is 50 °C/min that, from observations discussed in the third chapter, is considered too fast to promote water resorption.

Experiment IK-13 (foaming only experiment; T_{foam} = 900 °C; t = 24 h) allowed to investigate in detail the temporal evolution of volatile exsolution and bubble growth (Fig 3; Table 1). Indeed, leaving the probe on the sample surface during the whole foaming stage, the complete displacement vs. time signal was recorded. A closer analysis of the displacement-time path allows the identification of different processes. In particular, four regions can be recognized with increasing experimental time. Upon heating from room temperature to T_{foam} (region I, Fig. 3a), obsidian glass expands and the displacement increases almost linearly with T (and t) up to glass transition temperature Tg. Fig. 3b shows the glass thermal expansion in the domain of temperature; the normalized displacement ($\Delta L/L_0$) and its derivative is plotted as a function of T, i.e. the thermal expansion coefficient α_V (note that a factor of 3 was used to convert linear to volume thermal expansivity). The α_V coefficient increases with increasing temperature (α_V =10-30 x 10^{-6} °C^{-1} at T < 600 °C; Fig. 3b) and shows a peak of 78 x 10^{-6} °C^{-1} at Tg = 685 °C. Above Tg, ($\Delta L/L_0$) and α_V signals are more complicated being affected by viscous deformation of the melt and perhaps the onset of crystallization and/or degassing. To investigate more in detail this region, we performed an independent DSC measurement using the same heating ramp (5 °C/min). Fig. 3c shows that the normalized signals from TMA and DSC display an excellent match below Tg and yield identical Tg peak values. At higher T, the sink in Cp curve with a minimum at T ~ 800 °C records exothermic reactions likely ascribable to the onset of minor crystal nucleation (not detected by post-run Raman analysis). Further increase in Cp trace is probably related to the onset of volatile exsolution. All these processes are however hindered by a general decrease of displacement (viscous softening) that makes the precise onsets of volatile exsolution (and/or crystallization) difficult to identify. The displacement decrease dominates the initial part of the isothermal stage at T_{foam} (region II; Fig. 3a). With time, the trend inverts and the displacement increase is indicative of the dominant contribution

of degassing and bubble formation to sample expansion (region III; Fig. 3a). Displacement reaches a stable value after about 3-13 hours at T_{foam} = 900 °C (region IV; Fig. 3a).

The temporal evolution of porosity is tracked by he estimated increase in volume with time. The increase of sample height can be converted to an increase in porosity (Fig. 3d) by comparing the (measured) pre-run unfoamed and the (calculated) post-foaming volume of the core (see Supplementary Materials 2). Since viscous softening hides the precise onset of volatile exsolution and bubbles nucleation (Fig.3a), the minimum displacement value in the region II has been set as zero for the purpose of porosity calculations displayed in Fig. 3d, where region III (Foaming) and IV (Equilibrium plateau) are plotted versus time. The estimated sample expansion due to bubble growth (slope of the porosity trace in Fig. 3d) occurs with a rate of 0.1 vol.% min^{-1} up to the plateau, which is indicative of the end of the degassing. For the example in Fig. 2 (IK-13) the final calculated porosity (49.7 vol.%) shows an excellent agreement with the porosity measured by pycnometry (46.4 vol.%) on the post-run sample. This is however not true for higher temperature foaming experiments (e.g., IK-11) where the effect of the probe in altering the isotropic expansion of the sample becomes more important and the resulting calculated porosity (23.1 vol.%) departs from that measured at the end of the experiment (46.0 vol.%) (see Table 2 and Supplementary Materials 2). For this reason, all the subsequent deformation experiments were performed on samples foamed without the presence of the probe on their surface.

The estimated ϕ_i, with no distinction between *single-stage* and *double-stage* experiments, spans from 10.6 to 50.5 vol.% (Table. 2).

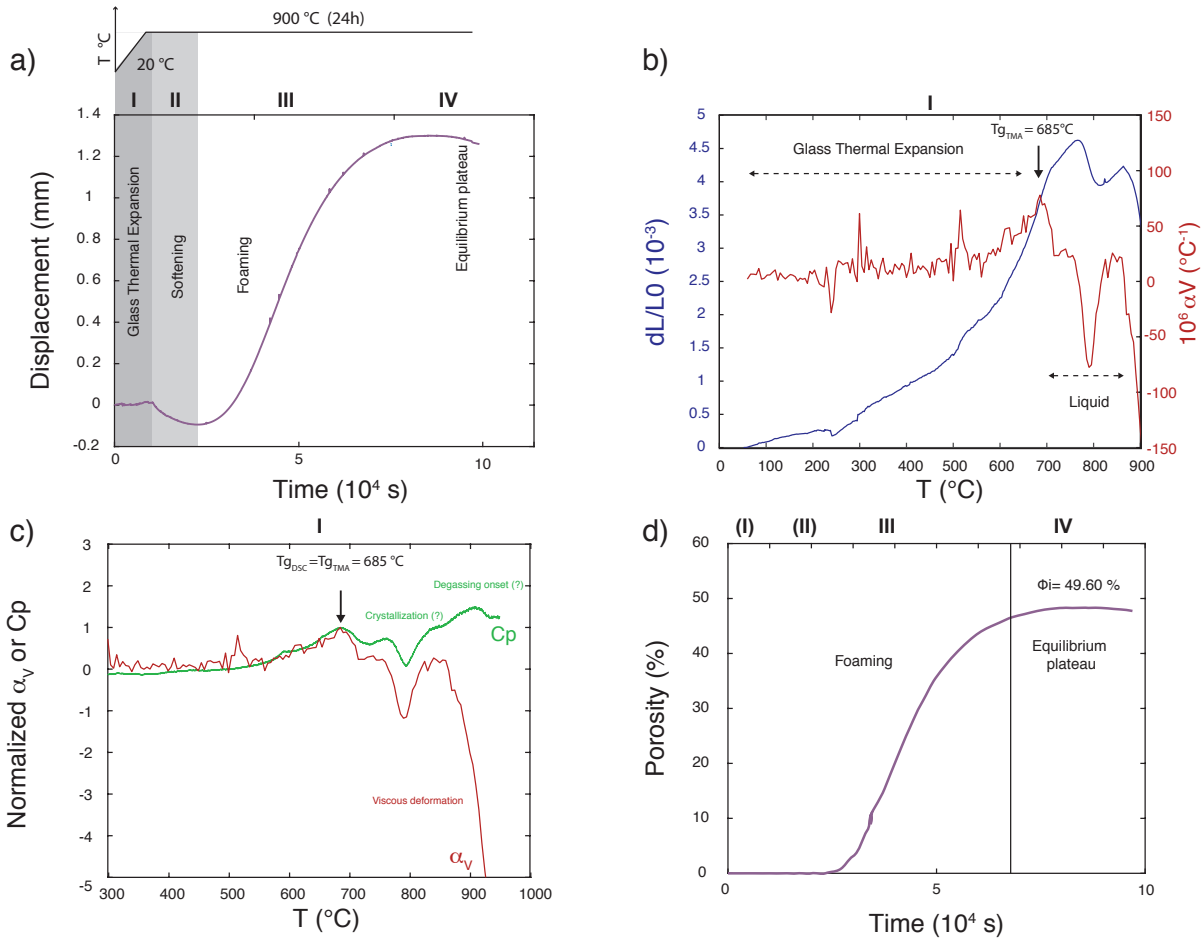

Figure 3. Example of an experiment leaving the probe on the sample (IK-13). a) Displacement vs Time plot; the dominant processes occurring during the experiment are described: Glass Thermal Expansion (I), Softening (II), Foaming (III), Equilibrium plateau (IV). Above Tg, thermal expansion, softening and foaming could occur simultaneously. b) Normalized displacement dL/L0 (in blue) and volume thermal expansivity coefficient α_V (red) vs. temperature (°C); Tg peak at 685 °C allows to separate glass thermal expansion from liquid region. c) Normalized signal from TMA (red) and DSC (green) as a function of temperature. d) Calculated temporal evolution of porosity.

Table 2. Summary of the post-foamed and post-deformed experiment cores physical properties

	Post-foaming physical properties						Post-deformation physical properties								
SAMPLE	T_{foam} (°C)	t (h)	L_i (mm)	D_i (mm)	V_i (mm^3)	ϕ_i (%)	T_{def} (°C)	L_f (mm)	D_f (mm)	m_f (g)	V_f (mm^3)	ϕ_f (%)	log η (Pa s)	γ	ε_f (s^{-1})
IK-13	900	24	6.19	6.80	166.31	49.60	-	-	-	-	-	-	-	-	-
IK-11	950	10	5.85	5.56	125.35	23.13	-	-	-	-	-	-	-	-	-
IK-9	900	15	5.80	6.29	142.51	40.39	750	5.62	5.79	0.20	141.90	40.14	10.23	0.04	1.35E-06
IK-7	900	24	6.97	5.84	157.95	30.32	750	6.63	6.13	0.26	189.30	41.86	10.58	0.04	5.80E-07
IK-19	900	24	5.35	5.48	112.98	20.43	750	5.04	5.14	0.21	112.52	20.10	10.62	0.03	6.73E-07
IK-32	900	24	6.36	5.82	143.57	29.39	750	6.30	5.90	0.24	142.60	28.91	10.36	0.03	9.51E-07
IK-18	925	20	6.08	5.94	140.91	31.86	750	5.83	6.06	0.23	133.70	28.18	10.58	0.05	6.25E-07
IK-25	925	20	5.98	5.92	137.94	31.29	750	5.91	6.03	0.23	142.50	33.49	10.40	0.04	8.15E-07
IK-20	950	10	5.98	5.80	134.32	29.43	750	6.10	5.61	0.22	140.90	32.73	10.35	0.07	1.29E-06
IK-30	950	10	6.49	6.11	155.34	35.48	750	6.00	6.49	0.23	171.30	41.50	10.11	0.09	1.78E-06
IK-6	900	24	5.40	5.70	118.97	26.59	800	4.58	5.50	0.21	121.00	27.82	9.97	0.16	2.34E-06
IK-23	900	24	5.56	5.46	117.58	18.71	800	4.97	5.60	0.23	107.90	11.42	10.12	0.11	1.90E-06
IK-21	925	20	6.00	5.76	134.48	27.11	800	6.14	5.06	0.23	133.60	26.64	9.73	0.18	3.24E-06
IK-26	950	2	5.39	5.34	111.51	14.96	800	4.88	5.38	0.22	111.60	15.02	9.91	0.11	2.62E-06
IK-28	950	2.5	5.26	5.20	105.96	10.56	800	4.80	5.41	0.22	104.60	9.40	9.99	0.11	2.28E-06
IK-27	950	4	5.85	5.66	128.74	24.52	800	5.12	5.90	0.23	130.00	25.25	9.71	0.14	3.24E-06
IK-10	950	10	5.87	6.24	142.73	39.61	800	4.73	6.49	0.20	137.40	37.27	9.30	0.23	4.44E-06
IK-22	950	10	6.03	5.94	139.48	32.06	800	4.67	6.58	0.22	136.70	30.67	9.62	0.24	3.42E-06
IK-17	900	24	6.35[a]	6.15[a]	121.48	19.01[a]	750	5.97	6.35	0.23	121.80	19.22	10.46	0.02	3.10E-06
IK-16	925	20	6.29[a]	5.98[a]	146.45	33.04[a]	750	6.11	5.98	0.23	144.70	32.23	10.37	0.06	1.36E-06
IK-15	950	10	5.81[a]	5.47[a]	159.00	39.22[a]	750	5.79	5.52	0.23	159.50	39.41	9.94	0.07	1.20E-06
IK-36	975	6	6.29[a]	6.69[a]	196.00	50.52[a]	750	5.49	6.72	0.22	188.00	48.41	9.55	0.11	4.32E-06
IK- 35	1000	5	6.51[a]	6.92[a]	178.30	46.53[a]	750	5.78	6.95	0.23	172.40	44.70	9.54	0.12	3.96E-06
IK-37	1050	4	6.45[a]	7.29[a]	194.10	50.36[a]	750	5.55	7.29	0.22	185.30	48.00	9.37	0.13	4.82E-06

Notes: The post-foaming geometry (named with the suffix "i", e.g., L_i, d_i ϕ_i), is calculated for Single-stage experiments. Post -deformation properties were measured by calliper (L_f and d_f), precision balance (m_f). V_f was mesured by He-picnometer. Final porosity ϕ_f is calculated from volume variation log η is calculated with Gent 1960 formula.

[a] The post-foaming geometry is measured for Double-stage suite (by calliper and He-Pycnometer) .

4.2. Rheology of vesicle bearing melts

After the foaming stage (both for *single* and *double-stage* experiments), temperature was reduced from T_{foam} to T_{def} with a cooling rate of 50 °C/min. After 1 hour at T_{def} , a load of 150 g was applied on the foamed core through the probe. The core is deformed isothermally (T_{def} 750 - 800 °C), and the temporal evolution of the displacement (μm) with time (s) allows to recover rheological data. The imposed uniaxial load remains constant during the whole rheological measurement.

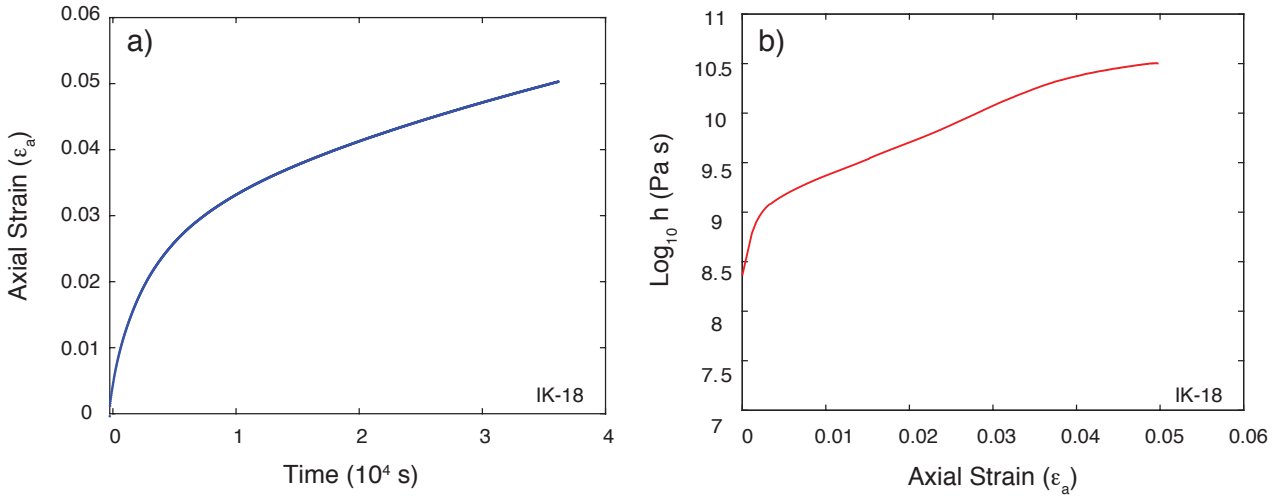

Figure 4. Analysis of post-run curves. a) Axial strain (ε_a) vs. Time (s) plot in which the first part of the curve is characterized by a fast change in slope, while it became gradually constant. b) Log viscosity vs Axial strain curve displays the same behaviour. The viscosity value is referred to the final part of the curve in which the slope remains unchanged.

Axial strain (ε_a) curve vs. time (Fig. 4a) shows an initial high strain rate (steeper slope), which becomes constant with time. The measured strain rate in whole dataset is between 5.8 10^{-7} and 7.61 10^{-6} s^{-1}, and the final values of ε_a span 0.02 to 0.24. In Fig. 4b the Axial Strain is related with the bulk viscosity curve. For bulk viscosity (η_{bulk}) estimation Gent's (1960) parallel plate theory was taken into account; the incremental variation of sample viscosity was calculated with *perfect slip* Gent's equation (see Supplementary Materials 2).

In all experiments, viscosity increases over time (Fig. 5), giving the impression of asymptotically approaching a steady state at long durations. This behavior reflects lava flow conditions, where no evidence of yield strength is observed, and the viscosity is best approached by a strain rate and temperature-dependent power law equation (Avard and Whittington, 2012).

Viscosity values of reference (Table. 2) are relative to the end of the plateau, when the axial strain curve becomes constant with time (i.e. constant strain rate). Being the load (and therefore stress) constant this condition corresponds to that of steady flow.

As a general observation viscosity decreases with increasing sample porosity. For *single-stage* experiments the variation in viscosity values is quite wide if we consider the two targets T_{def} (Fig. 5). Indeed, for samples deformed at 800 °C viscosity spans from 9.33 to 10.13 log Pa s; whereas, cores deformed at T_{def} of 750 °C recorded higher values of viscosity, ranging from 10.18 to 10.77 log Pa s. Viscosity values relative to DS experiments (T_{def} 750 °C) range from 9.37 to 10.40 log Pa s.

Among SS experiments, deformed at different T_{def}, there is a difference in viscosity range of about one order of magnitude (Fig 5 a, b). The same range, in terms of orders of magnitude, is shown from SS and DS experiments, deformed at the same T_{def} = 750 ° (Fig 5 b, c).

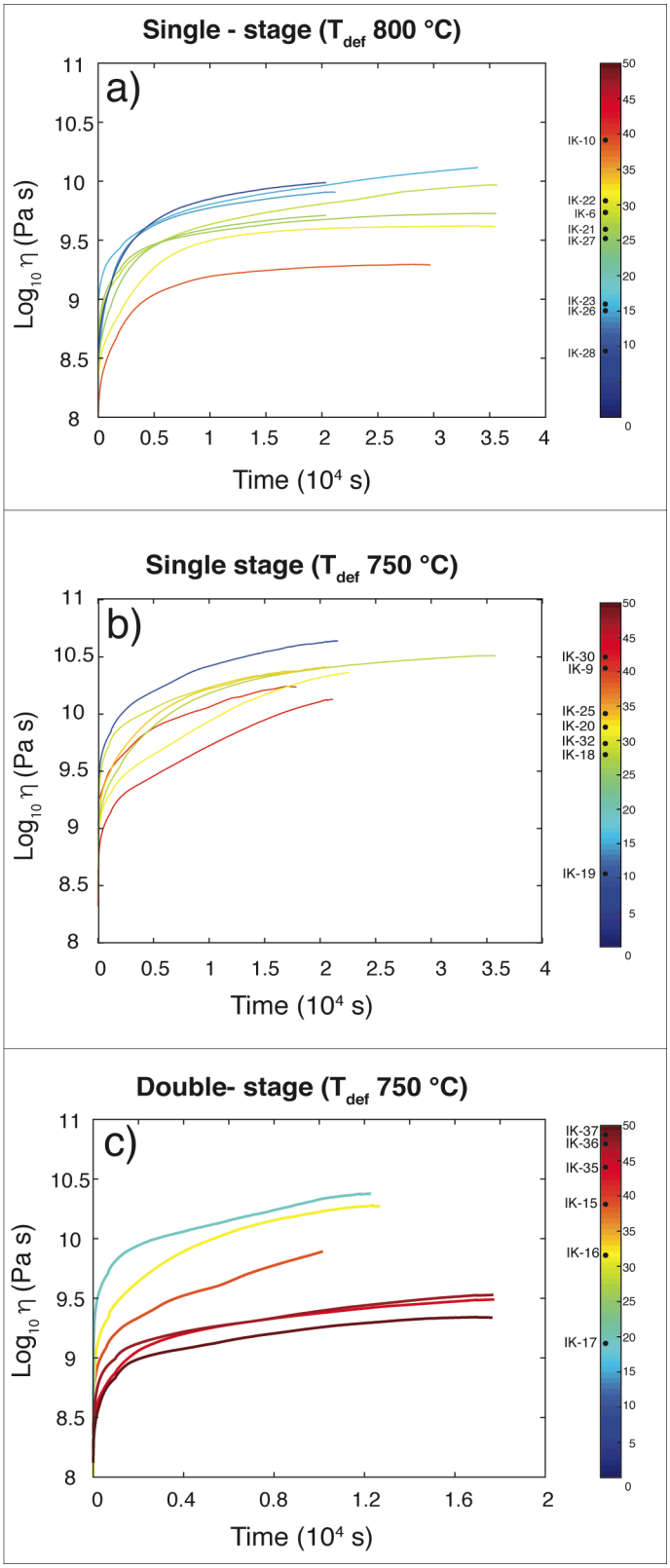

Figure 5. Results from rheological measurements under a constant load (150 g) expressed as Log_{10} η_{bulk} (Pa s) vs. Time (s) relative to the three subsets. a) Single-stage at T_{def} 800 °C); b) Single-stage at T_{def} 750 °C); Double-stage at T_{def} 750 °C). The colour of the curve is referred to the colour scale bar (on the right) in which the name of the samples and the relative ϕ_f is reported (in vol.%). Each curve reaches a stable plateau value, which reflects the effective viscosity of the foamed core referred to a specific final porosity value.

4.3. Post-run analysis

Post-run physical properties of each core were determined at the end of the deformation phase (Table. 2). Final length (L_f) and diameter (D_f) were measured with precision calliper; details of the strain analysis are described in Supplementary Materials 2. No mass (m_f) change indicative of volatile escape was detected at the end of the experiment. Final porosity (ϕ_f) measured by He-pycnometry spans from 6.8 to 48.4 vol.%.

Fig. 6a, and 6b relate ϕ_i values with ϕ_f, displaying a general good match between initial and final porosities values, whereas Fig 6c shows the variation of the porosity with strain. In general, only few data points record a discrepancy between ϕ_i and ϕ_f, (due to instrumental error or uncertainty in ϕ_i determination) while most of the data collapse on the 1:1 line.

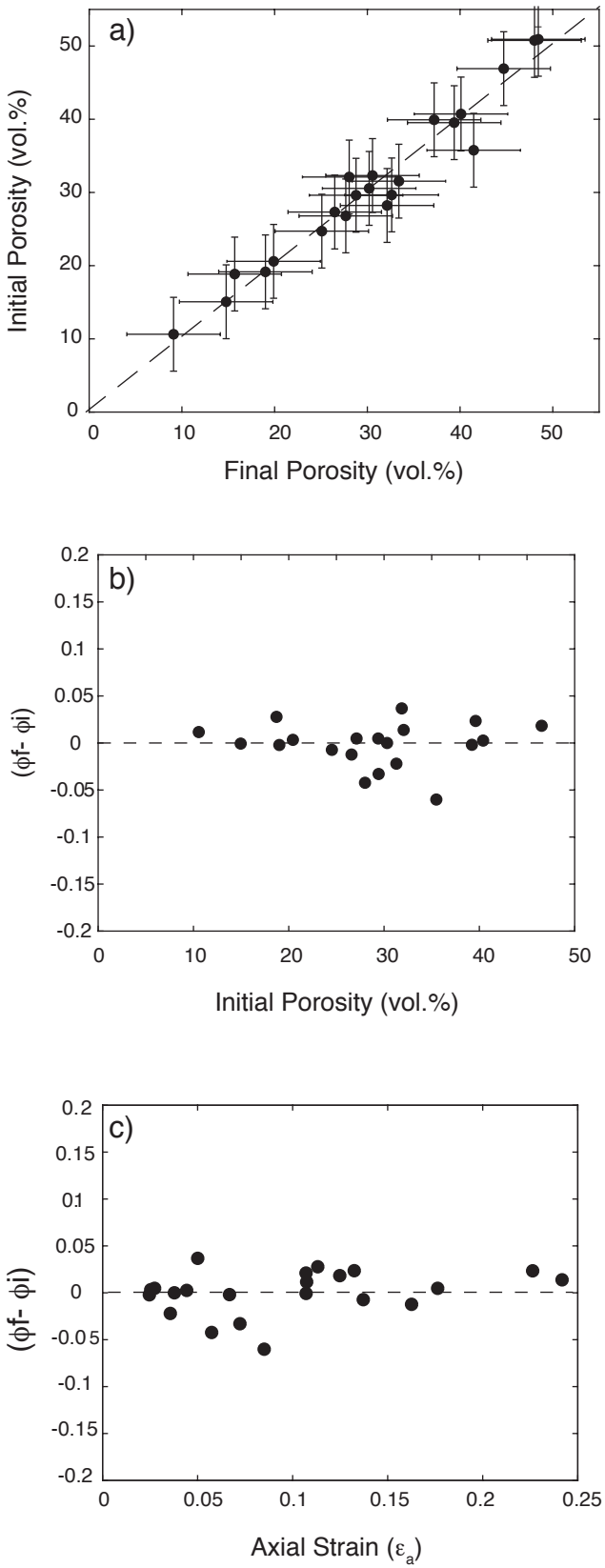

Figure 6. Comparison between initial (post-foaming) and final (post-deformation) porosity relative to each obisian core; the difference between these values is also shown and its relationship with sample strain. a) Initial porosity (ϕ_i) plotted against final porosity (ϕ_f) values (vol.%). The dashed line describes the 1:1 ratio. b) Analysis of porosity change $\Delta\phi$ (= ϕ_f - ϕ_i) in each sample during experiments; the dashed black line indicates the 0 value, when hypothetically, no variation in ϕ_f - ϕ_i is recorded. c) $\Delta\phi$ is compared with the final total strain the sample,

Fig.6b shows porosity change ($\Delta\phi$) from ϕ_i (post-foaming) and ϕ_f (after deformation) as a function of ϕ_i. A good correspondence between ϕ_i and ϕ_f is recorded, as the majority of the values collapse on the zero line zone or in the region nearby ($\pm$ 5 vol.%). Fig 6c the $\Delta\phi$ is plotted as a function of strain, showing that even for higher strain the discrepancy between ϕ_i and ϕ_f is negligible. This first test suggests that the initial porosity is well preserved after the deformation stage. Fig. 7 displays images of a sample after each experimental stage.

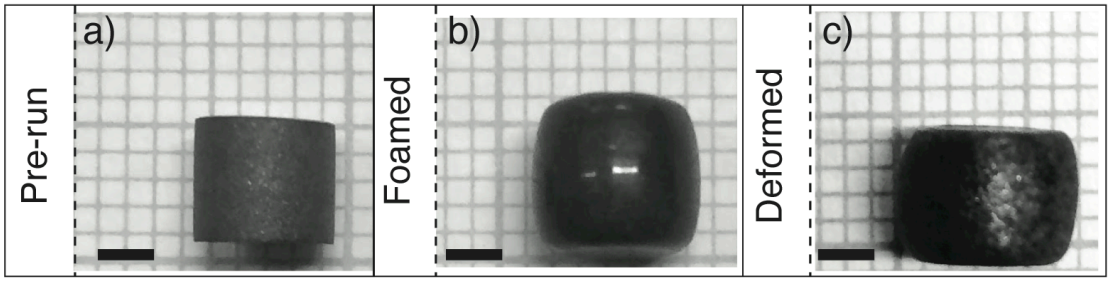

Figure 7. Images of an obsidian core after each different experimental stage: a) Pristine pre-run sample; b) Sample after the foaming stage; c) Foamed and deformed obsidian core.

In order to further investigate porosity preservation, four samples were selected and used specifically for this part of the study: two foamed (IK-2 and IK- 38) and two foamed + deformed samples (IK-11 and IK-14). The same experimental approach and analytic procedure were applied for pre- and post physical properties determination. At the end the experiments, the samples were cut, polished and micro-photographs of the sections were acquired with an optical microscope in order to analyze bubbles internal network. Fig. 8 shows the sections relative to foamed (IK-38, IK-2) and foamed + deformed (IK-11, IK-14) cores from longitudinal and radial perspectives. The top view of the radial section of IK-38 (foamed) and IK-11 (foamed + deformed) are shown in Fig. 8a and 8b. In both photographs, bubbles appear near spherical, with various sizes and with a maximum diameter of about 500 μm. In Fig. 8c and 8d the longitudinal section of IK-2 and IK-14 samples is displayed (foamed and foamed + deformed cores). This view provides more details about bubble shape during foaming stage and after deformation. Indeed, in Fig. 8c (foamed core) bubbles seem to maintain a spherical shape, with unsorted bubble sizes and a maximum diameter of ~ 500 μm. It is noteworthy that those features are similar to the radial section of the foamed core (Fig. 8a) and this suggests that the 1:1 assumed ratio among radial and longitudinal strain driven by bubble growth) is reasonable for initial porosity estimation (see Supplementary Material 2).

Looking at the longitudinal section of deformed core Fig. 8d, bubbles appear elongated perpendicularly to the direction of the applied stress; this indicates that during deformation, bubbles responded to the applied stress changing their shape from spherical to ellipsoidal. The change in shape allowed to accommodate the stress maintaining sample (i.e. bubble) volume unchanged from foaming to deformation stage.

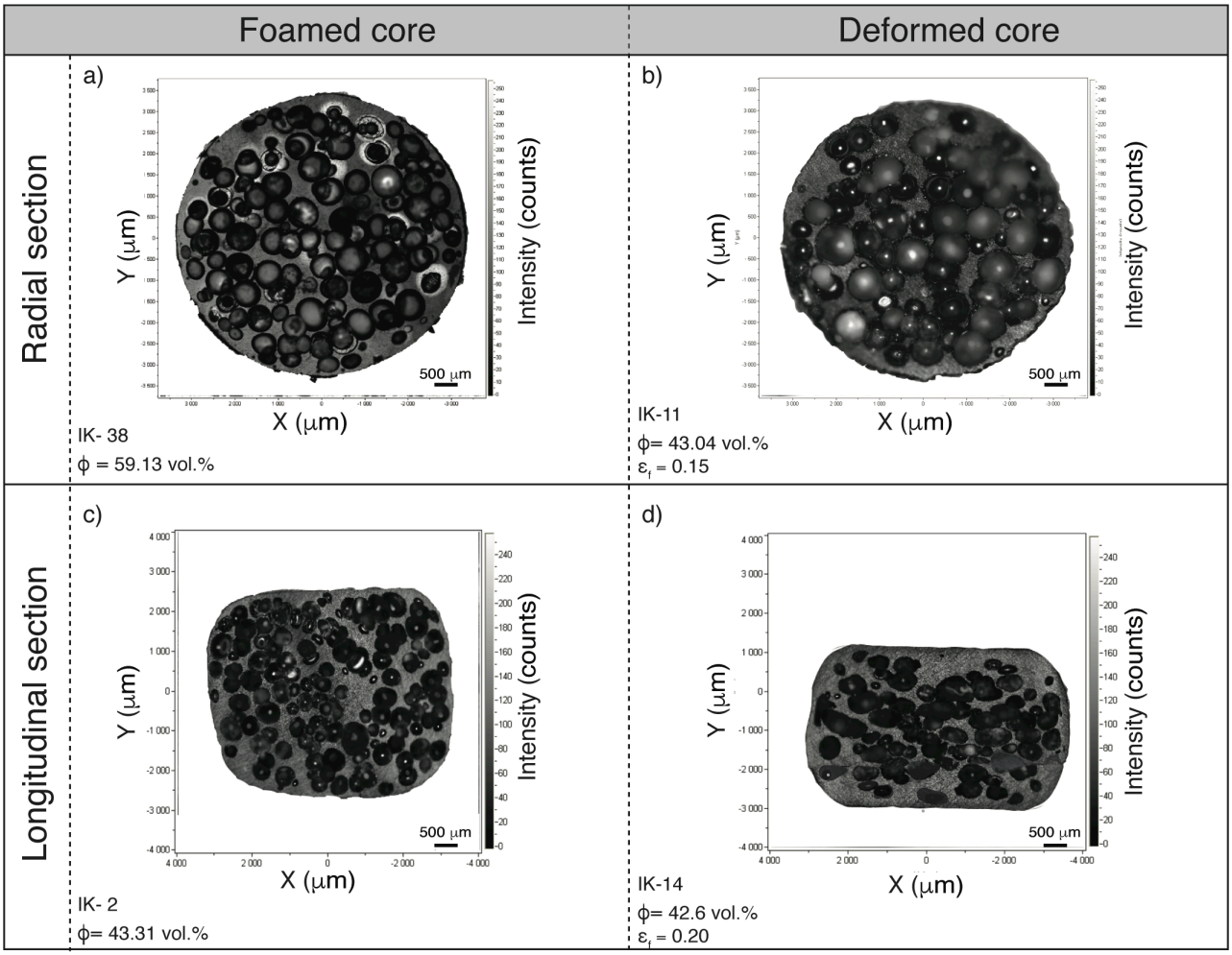

Figure 8. Microphotograph of experimental run products. Images are relative to four different foamed samples. (a-c) Radial (a) and longitudinal (b) sections of foamed (IK-38) core. (b-d) Radial (b) and longitudinal (d) sections and foamed + deformed core (IK-11). Porosity values measured with He-Pycnometer at the end of each experiment are indicated. For deformed cores final axial strain is also reported.

At the end of each experiment, cores showed an opaque glassy skin, where no pores or fractures were observed (Fig. 7c). In foamed samples (Fig. 8a and 8c) bubbles closer to this external edge appear more elliptical, whereas in the middle point of the core their shape remains near-spherical; this behavior can be attributable to this external skin, that acts like a “barrier”, preventing

the spontaneous rounded growth of bubbles and giving them a more elongated shape. At the same time that "barrier" isolates the inner bubbles network from the outside (e.g., von Aulock, et al., 2017).

All these observations suggest that porosity loss is negligible during deformation stage, bulging accommodates the shortening of the core and its volume remains constant thus the initial porosity remains preserved; this is further testified by the comparison between axial and radial strain displayed in Fig. 9, where the latter one recorded on average a larger variation (See Supplementary Material 2 for details).

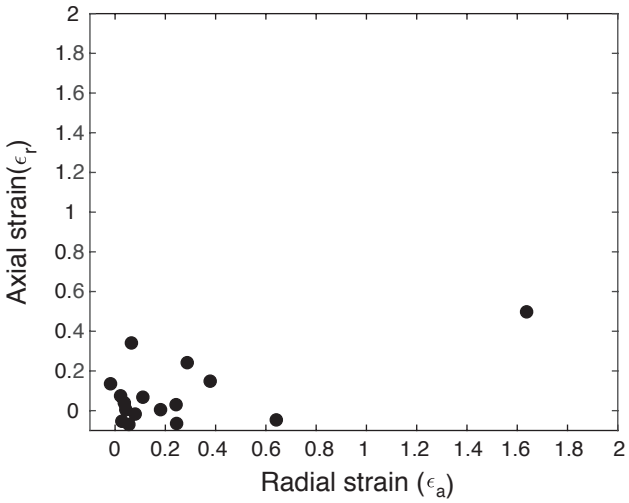

Figure 9. Comparison between axial and radial strain of the whole dataset at the end of the deformation stage.

5. Discussion

5.1 Viscosity model for bubble-bearing rhyolite

Values of final porosity (ϕ_f) and viscosity (η) recorded at the end of each experiment (plateau values, flow conditions) are used for the modeling purposes. The viscosity-time curves (Fig. 5, Result Chapter) show that low percentage of porosity corresponds to higher viscosity values and vice versa. This first observation suggests that a general trend exists, namely an inverse relationship between pore content and viscosity in rhyolitic material.

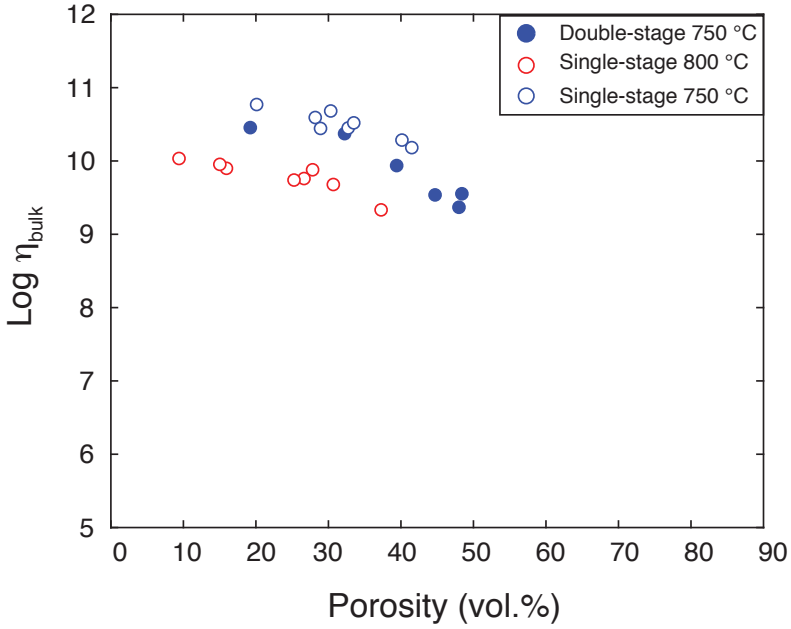

Figure 10. Relation between bulk viscosity (η_{bulk}) and porosity (ϕ_f) for *single-stage* experiments at different T_{def} (800-750 ° and *double stage* experiments.

Fig. 10 shows *single-stage* and *double-stage* datasets, where log bulk viscosity (log η_{bulk}) is plotted against final porosity values; a general decrease in viscosity with increasing in porosity is always observed, independently from the T_{def} (800 - 750 °C). However, a difference in the viscosity values is evident when considering the two target temperatures (red and blue symbols), and between SS and DS experiments performed at the same T_{def} = 750 °C.

In order to parameterize the relationship between viscosity and porosity, each dataset has been fitted following the equation of Quane et al. (2009), which represents one of the most recent models, based on experiments on natural materials:

$$\log \eta_{bulk} = A + B/T\,(K) - \alpha\,(\phi_f / 1 - \phi_f) \qquad (1)$$

where A, B and α are fitting parameters. In this equation, the first part [A+B/T(K)] captures the temperature dependence of the melt viscosity, while the second part [α (ϕ_f/ 1- ϕ_f)] takes into account the effect of porosity on the multiphase magma. According to this equation, the melt viscosity (η_0= A+B/T (K)) is assumed to have an Arrhenian dependence over the range of temperatures of the experiments.

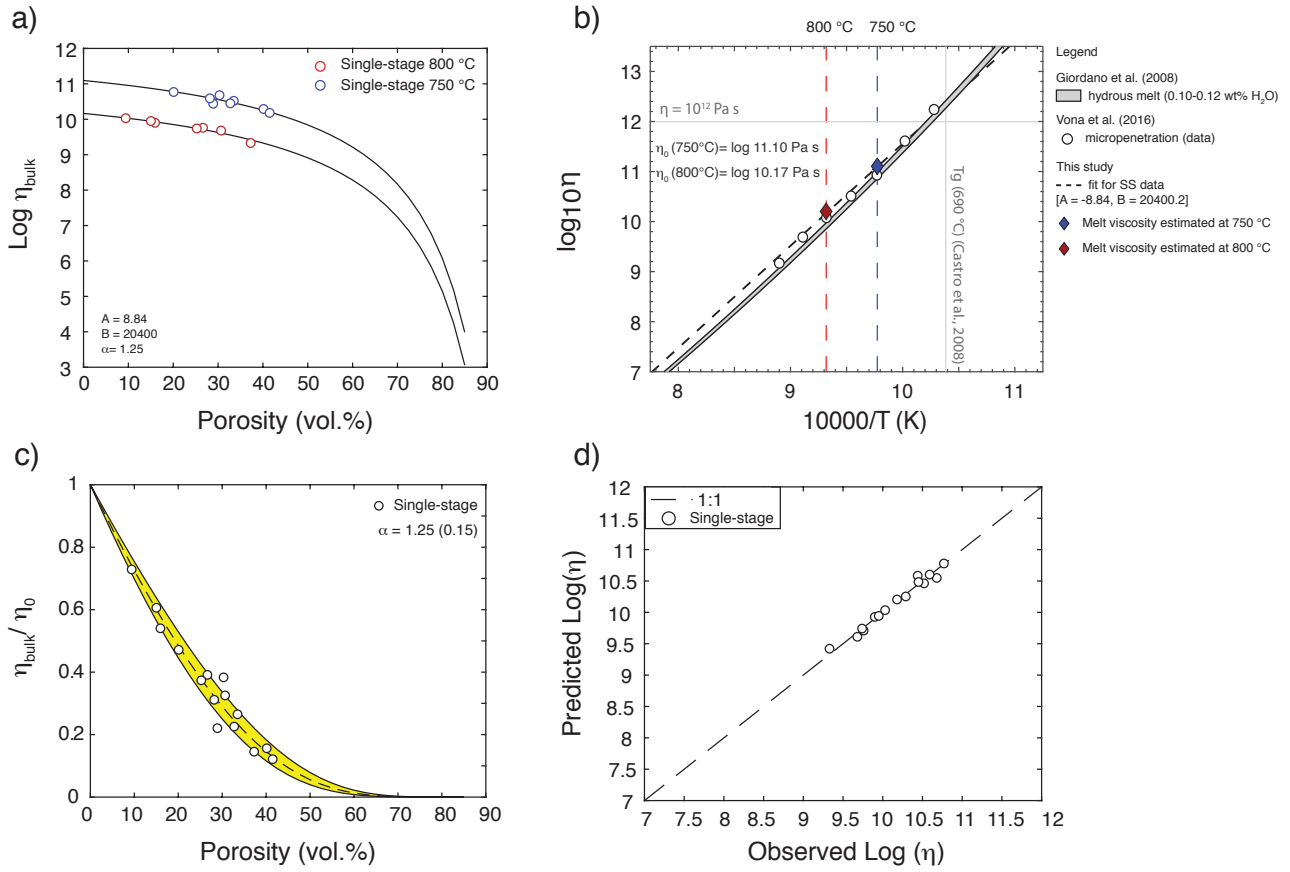

Figure 11. Model for viscosity as a function of porosity for *single-stage* experiments (SS) at the two target T_{def} =750 °C (blue) 800°C (red). a) Fit of the two subsets using Quane et al., (2009) equation form. b) Viscosity values of the hydrous melt is calculated using Giordano et al (2008) model (gray line) Viscosity values measured by micropenetration (white circles) of non-vesiculated melts from Vona et al., (2016) The black dashed line defines the fit for single-stage experiments using the fitting parameters A= -8.84 and B=20400.2; the calculated melt viscosity value from single-stage fit is also reported for 750 °C and 800 °C (blue and red diamond) which is 11.10 and 10.17 respectively. c) η_{Bulk}/η_0 plotted vs. porosity, d) Comparison between observed and predicted viscosity.(dashed line represents 1:1 line).

The fit results for the *single-stage* experiments are displayed in Fig. 11. A unique fit for experiments performed at the two different T_{def}, provided Av= -8.84 B = 20400.2 and α = 1.25 as

optimal fitting parameters. The downward curve shape in the logarithmic space (Fig. 11a) is constrained by the viscosity values at 100% porosity, which tend toward values pertaining to pure gas. At zero porosity the model curves provide estimation of the melt viscosity (11.10 log Pa s at T_{def} =750 °C and 10.17 log Pa s at T_{def} = 800 °C). In Fig. 11b, this calculated melt viscosity data are almost undistinguishable from values measured by Vona et al. (2016) by micropenetration technique proving the goodness of the fit and of the selected functional form. Fig. 11c shows the η_{bulk}/η_0 versus porosity data and modeling. The yellow field corresponds to model results for $\alpha = 1.25 \pm 0.15$. Fig. 11d shows the calculated versus measured viscosity values. As it can be observed, the results of the fit are excellent with a $R^2 = 0.9758$.

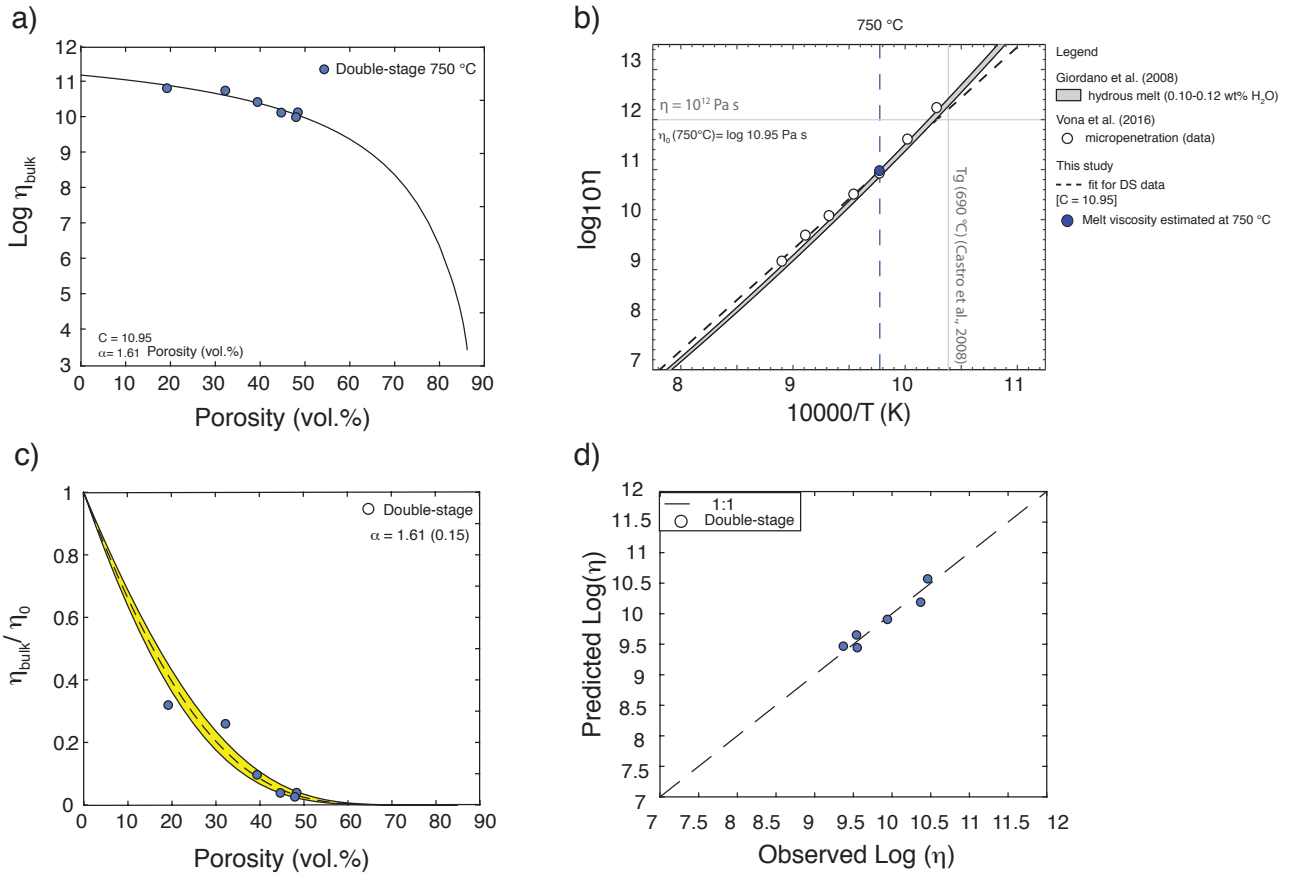

Figure 12. Viscosity model relative to double-stage suite of experiments (DS) at the target T_{def} = 750 °C a) Data points fitted using Quane et al., (2009) equation form b) Measured viscosity values using Giordano et al (2008) model (gray line) and by measured by micropenetration (white circles) from Vona et al., (2016) The black dashed line defines the fit for double-stage experiments and the calculated melt viscosity value from is reported for 750 °C (blue circles) which is 10.95; c) η_{Bulk}/η_0 plotted vs. porosity d) Predicted Log η_{Bulk} vs. the observed bulk viscosity values.

The results for the fitting of *double-stage* experiments is showed in Fig.12. In Fig 12a log viscosity versus porosity is showed. Viscosity decreases as a function of porosity of about 0.6 log units from 0 to 50% of porosity. Larger decrease in viscosity as a function of porosity is predicted at

higher porosity values. As all DS experiments were performed at the same T_{def}, the fitting parameters A and B can be replaced by a single parameter, namely C, which represents the calculated melt viscosity. The obtained α is 1.61. Also in this case, the intercept value on the y axis (i.e., the calculated unfoamed melt porosity) is equal to 10.95 log Pa s, within the experimental error of determination of micropenetration data (Fig. 12b). In Fig. 12c the DS data are presented as η_{bulk}/η_0 vs. porosity for $\alpha = 1.61 \pm 0.15$, and the inverse relation is again verified. In Fig. 12d, measured versus calculated viscosity values are shown. Data are reproduced with a $R^2 = 0.9249$.

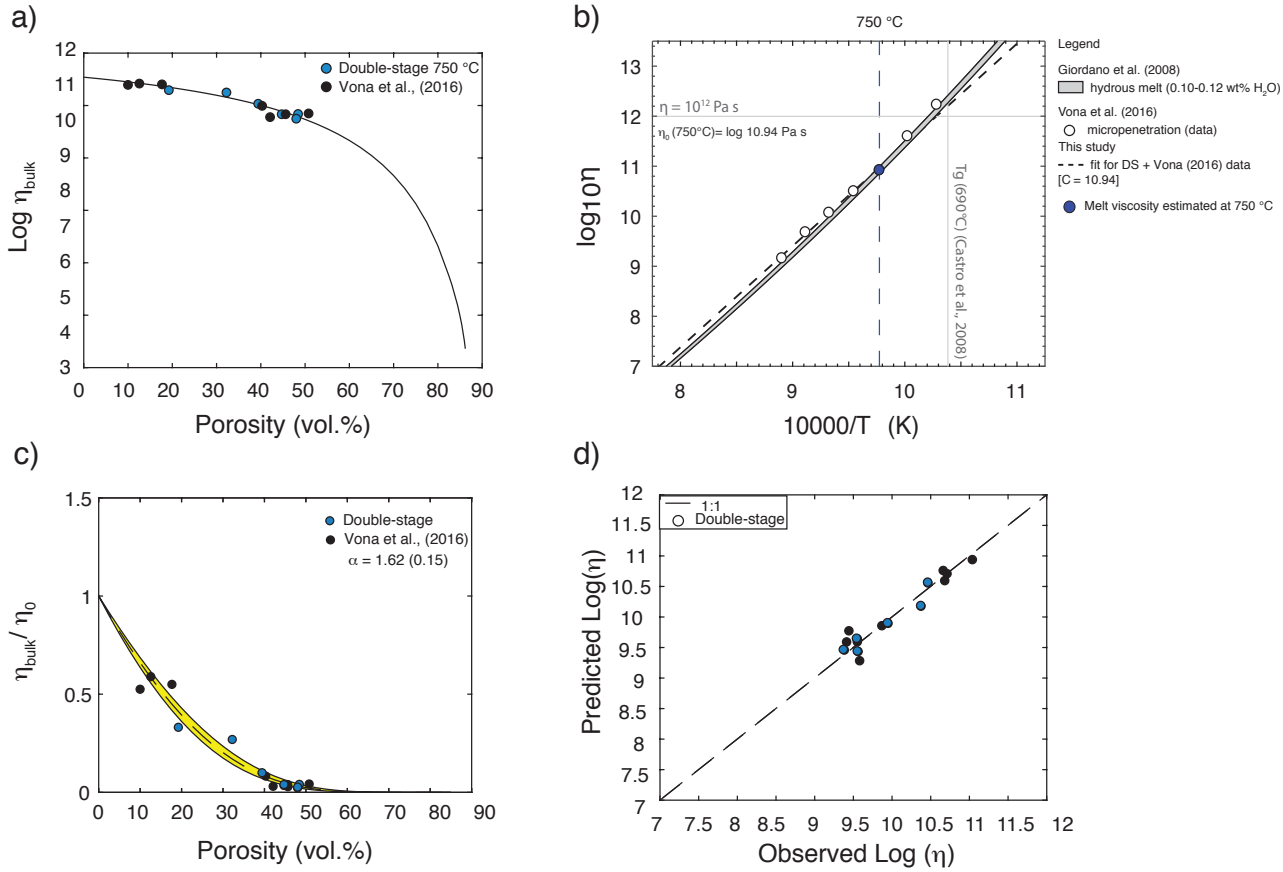

Figure 13. a) Log η_{Bulk} vs. porosity data and curve fitting. Results from double-stage experiments (this study) are plotted together with data from Vona et al.,(2016); the two dataset are treated together for the viscosity parameterization using Quane et al., (2009) equation form. b) Measured viscosity values from Giordano et al (2008) model (gray line) and by micropenetration measurements (white circles) from Vona et al., (2016); the calculated melt viscosity from the fit of double-stage experiments + Vona et al., (2016) is reported (blue circles) which is 10.94; c) η_{Bulk}/η_0 plotted vs. porosity. d) Predicted vs. the observed bulk viscosity values.

The starting material used in Vona et al. (2016) work is the same used here. Moreover, the experimental rationale behind the double stage experiments (DS) is very similar to the Vona et al (2016) measurements. In both cases rheology was investigated at the same temperature (750 °C)

through uniaxial compression experiments (pure shear regime) conducted at similar strain rates ($5 \cdot 10^{-5}$ s^{-1}) on previously vesiculated material. For these reasons, we combined the two datasets in a single parameterization using Quane et al. (2009) functional form, as for the SS and DS measurements. Merging the two datasets, we critically revised the overall quality of each measurement.

Experimental problems were encountered for the experiments AR-IK 34 and AR-IK 21 of Vona et al. (2016) and they were then discarded from the data set. In particular, AR-IK 34 did not show change in porosity during deformation, unlike the experiment AR-IK-47, performed under the same conditions and original porosity value; the measurement was therefore considered unsuccessful. Experiment AR-IK 21 was reproduced in the new dataset (IK-17). With respect to the overall data, AR-IK 21 falls outside the trend and we did not further consider it for the fitting. Fitting results are shown in Fig. 13; the fitting parameters of DS + Vona et al., (2016) (Fig.13a) are C = 10.94 and α = 1.62, very consistent with the results for the DS experiments only. As a consequence, also melt viscosity prediction (Fig. 13b) and η_{bulk}/η_0 modeling (Fig. 13c) show very similar results. The correspondence between modeled and measured viscosity value (Fig. 13d) yields a R^2 = 0.9271 (very similar to the DS data alone). As illustrated in Fig. 11b (SS experiments) and 13b (DS experiments), our modeling is able to predict the non-porous melt viscosity. For DS subset, given the excellent agreement between the modeling and all the experimental data, it seems reasonable to replace the fixed C parameter with the same (T-dependent) A and B values obtained from *single-stage* data fitting, in order to reduce the model to a single equation. Fixing A and B, viscosity variations between SS and DS datasets are captured by alpha parameter only.

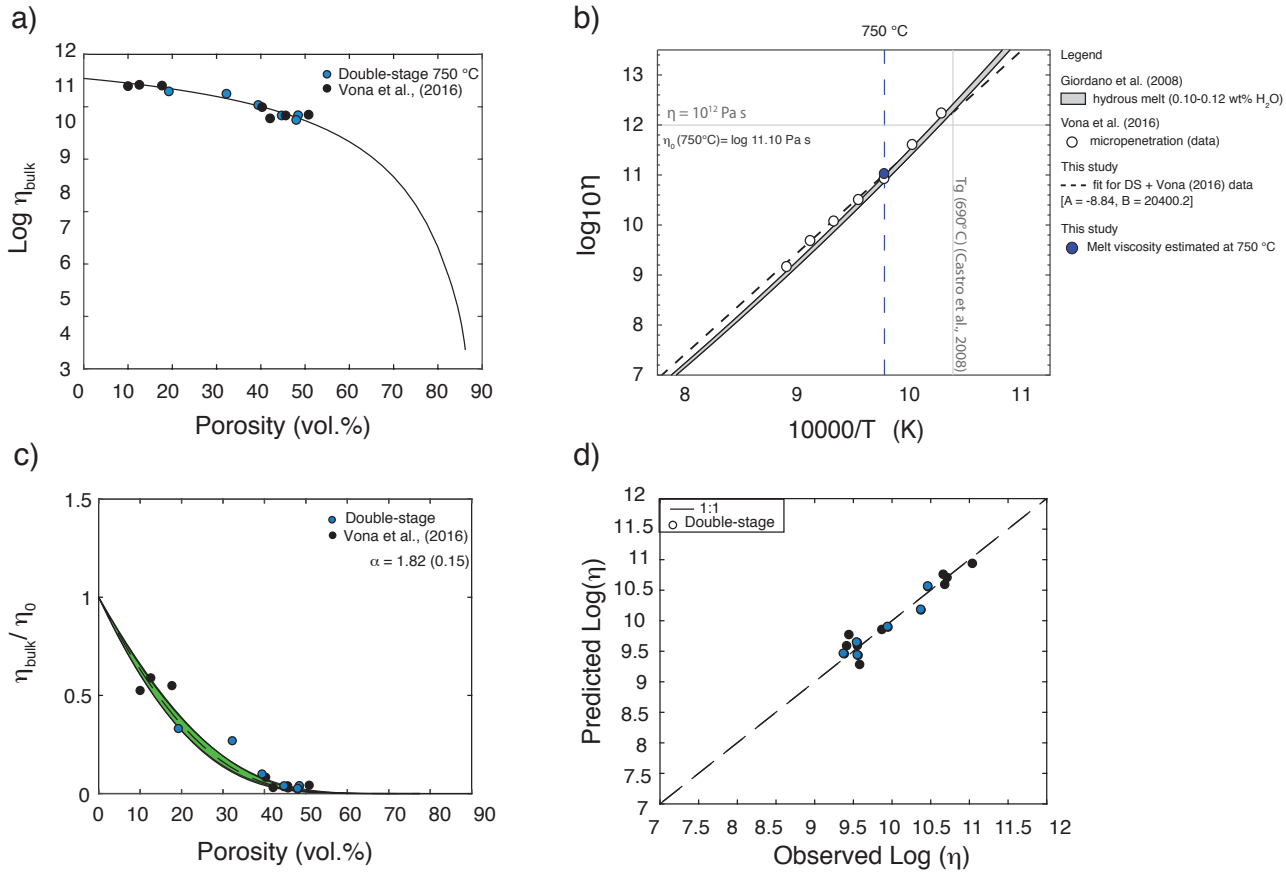

Figure 14. a) Log η_{Bulk} vs. porosity data and curve fitting relative to double-stage experiments (this study) + Vona et al.,(2016; b) Viscosity values of the hydrous melt is calculated using Giordano et al (2008) model (gray line) and measured by micropenetration (white circles) by Vona et al., (2016) The fit of the whole dataset was performed using the fitting parameters A= -8.84 and B=20400.2; the calculated melt viscosity at 750 °C (blue circles) is 11.10. c) η_{Bulk}/η_0 plotted vs. porosity. d) Predicted vs. the observed bulk viscosity values.

Fitting DS data with this strategy yields α = 1.82 (Fig. 12a). As illustrated in Fig. 14b and 14c, fixing A and B parameters do not affect the overall estimation of the melt viscosity and the viscosity prediction in the linear η_{bulk}/η_0 space, respectively. Comparison between calculated and observed viscosities yields a slightly larger R^2 of 0.9271.

5.2 Comparison with previous models

In Fig. 15 both proposed models are compared with the most recent model by Llewellin & Manga (2005); in this work, the authors presents an algorithmic approach in order to include the effects of bubble-suspension on the rheology of melts; in such model they provide two equations for two different regimes: 1) $Ca \leq 0.1$; 2) $Ca \geq 10$ and viscosity value is function of the gas volume-

fraction: for Regime 1) shear viscosity increases with increasing gas volume-fraction; in Regime 2) shear viscosity decreases with increasing gas volume-fraction.

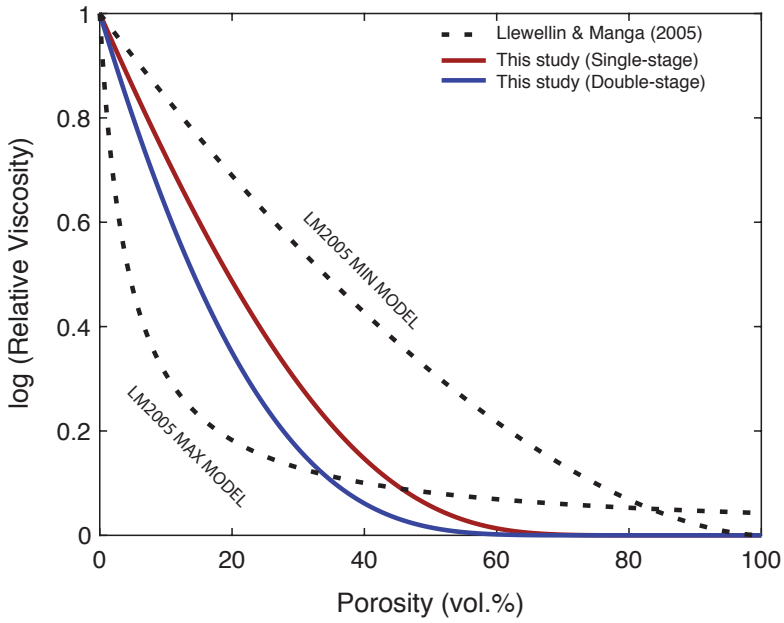

Figure 15. Final viscosity models for both single-stage (red line) and double-stage (blue line) respectively. The η_{bulk}/η_0 values are plotted against porosity ϕ_f and compared with Llewellin and Manga (2005) models (dashed gray lines) for both maximum and minumun effect at Ca ≥1.

The two plotted dashed curves describe the Regime 2 considering the maximum and the minimum effect when the Ca ≥ 1. As the plot shows, *double-stage* dataset and *single-stage* trend both collapse in an intermediate region between the minimum and the maximum model. The *single-stage* model is closer to the "minimum effect" curve (Eq.2) from Llewellin and Manga (2005), whereas double stage experiments show a stronger effect of porosity on viscosity, and they describe a curve which better approximate the "maximum effect" model (Eq.3).

$$\eta_{r,\infty} = (1-\phi)^{5/3} \tag{2}$$

$$\eta_{r,\infty} = \frac{1}{1+22.4\,\phi} \tag{3}$$

The relative difference between the *single-stage* and the *double-stage* curves is approximately 0.6 log Pa s for 50% porosity, becoming smaller as the porosity decreases. We interpreted the difference in the two curves (SS and DS), all other experimental conditions being

equal, as due to the two experimental approaches used: *single-stage*, where the deformation instantaneously followed heating, and *double-stage*, where deformation was preceded by cooling and resting of the sample at room temperature for a pronged period of time

5.3 Effects of vesicles nature on rheological measurements

In our experiments, different foaming temperatures (T_{foam} from 900 to 1050 °C) produced variability in bubble content due to exsolution of volatiles in the obsidian glasses. Bubbles are assumed to be dominantly H_2O (Ryan et al., 2015a). The extent of exsolution of H_2O fluid, at constant T, was evidenced by a change in volume (due to an increase in ϕ), which depends on the 1-atm solubility of H_2O at a given temperature and on the experimental dwell time (10 - 24 hours); in this view is possible to consider, for the *single-stage* experiments, vesicles filled by vapor, which should remain inside the bubble during the whole experiment. No outgassing events were observed after the foaming and during the deformation stages, proved also by the little discrepancy between Φ_i and Φ_f. Indeed, in *single-stage* suite of experiments (in situ), cores are always kept above Tg in the liquid phase. During the foaming stage, they are in oversaturated conditions, whereas in the deformation stage they become undersaturated. Under such regime, no outgassing or degassing phenomena is expected.

In *double-stage* experiments, samples are cooled to room temperature after the foaming stage and left to repose in air for ~ 15 days, during which water loss/cracking phenomena may occur, affecting the microstructure of the sample and so promoting the different behavior; cracking of the samples may form during cooling due to the different thermal expansivities of the melt around vesicles. In fact, during the nucleation and growth of the bubble, the melt around the vesicle becomes dehydrated because of diffusion of water inside the vesicle. The water distribution in the melt becomes unequal with a more dehydrated layer of melt around the vesicle walls and more water-rich layers far from it. As the thermal expansivity of melt/glass depends on the water dissolved, layers of melt/glass with different water content will display contraction during cooling. If the cooling is sufficiently slow, the different stress components acting on the vesicle walls due to this differential contraction will produce cracks according to a well-defined pattern (Mungall et al., 1996). These micro-cracks can be a viable path connecting vesicles with each other and with the exterior (Fig. 16). If sufficient time is allowed, water from the vesicle can escape along this network of micro-fractures and outgassing can be promoted. This phenomenon was studied by Romano et al., (1996), which monitored the slow growth of the micro cracks around H_2O-bearing vesicles, developed in foamed glass, prone to rapid (200 °C/s) and slow (200 °C/min) cooling rates. It was

observed that the dimensions of cracks was strictly related to the cooling rates; indeed, in the rapidly quenched samples the total volume of the region affected by micro-fracturing was negligible; in contrast, the volume of the region interested by cracks surrounding the slowly quenched vesicles was on the same order as that of the vesicles themselves.

Since in the present work the decrease in temperature (e.g. from T_{foam} to room temperature) is 50 °C/min, (rather slow compared with the study of Romano et al., 1996) and that cracks propagation can happens over an extended period which goes from days to month, is reasonable to consider that DS experiments were affected by micro-cracks formation during the initial cooling and that subsequent crack propagation and H_2O-loss could have happened in the 15 days that elapsed from the foaming to the deformation stages leaving a water-free micro-cracked vesicle-bearing glass. During subsequent heating, the material undergoing deformation would be very different from the *single-stage* experiment. The vesicles will be water-free and, if viscous relaxation did not have time to occur, the melt around the bubbles will be rich in micro-cracks (Fig.16). In this case, the viscosity of the material is expected to be lower for at least two reasons. First of all, the presence of micro-fractures, and their possible propagation during heating, would greatly lower the bulk strength of the glass around vesicle, explaining the lower apparent viscosity values. The lower viscosity should be related to a general weakness of the framework, both because of an increase of the overall effective porosity and due to a cracks promoting stress concentration on the fracture's tip and brittle-ductile deformation style. Secondly, due to the presence of cracks, in the *double-stage* dataset, bubbles (at least the bubbles smaller than a threshold diameter) may have outgassed their water and be air-filled, while in *single-stage experiments* vesicles contain H_2O-vapour. Aside from the effect of different compressibility of air compared to water to the deformation of vesicles, the air-filled bubbles are supposed to be interconnected (open cell configuration), so not overpressure due to imposed load is generated. In the *single-stage* experiments, the bubbles are supposedly water-filled and isolated (closed cells configuration), and this would certainly generate an overpressure able to counteract to a certain extent deformation and flow. Following this interpretation, we renamed the two experimental approaches used in this study, open-cell (*single-stage* experiments) and closed-cells configuration (*double-stage* experiments).

In these two sets of experiments, the formation of the different microstructures of the samples was not controlled or monitored in any way. It is possible that different experimental conditions would promote different physical processes leading to different cracking formation and propagation. For instance, in our samples (both SS and DS) we noticed the formation of an outer rim of bubble-free glass. This bubble-free layer was probably caused by diffusion of water during heating and initial stage of foaming, which created an external anhydrous layer of melt where not

degassing occurred. The higher viscosity of this internal rim prevented probably to a certain extent outgassing during foaming and deformation, as also inferred by the elongated shape of vesicles in proximity of the layer.

We can assume that the layer also served as a barrier to complete outgassing of water during the secondary permeability through cracking which we postulated occurred in the double stage experiments. Several scenarios (experimental and natural) in which such a secondary permeability can be instead promoted resulting in an even more catastrophic effect on viscosity.

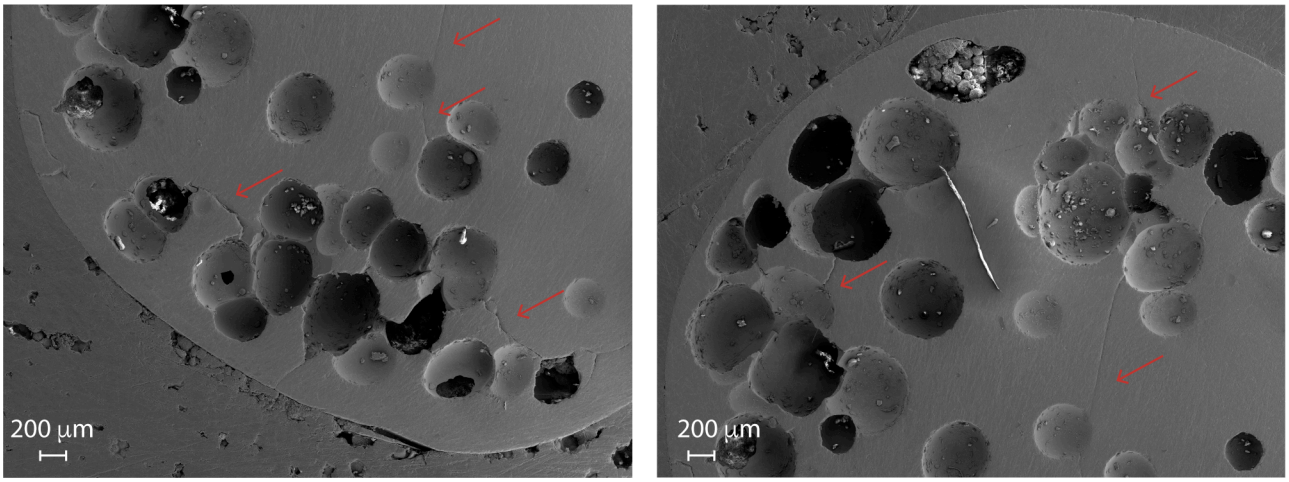

Figure 16.SEM images of a thin section of a foamed core quenched in water. The red arrows indicate the presence of micro-cracks within the sample structure.

6. Volcanological implications

All magmas degas as they rise through the crust as a consequence of decreasing pressure, resulting in volatile oversaturation and degassing and crystallization (e.g., Blundy et al., 2006). The rheological behavior of magmas is controlled by various factors, such as temperature, pressure, chemical composition, volatile content (mainly water), thermal history and strain rate (e.g., Webb and Dingwell, 1990; Giordano et al., 2008; Ardia et al., 2008). Magma viscosity is controlled also by the concentration and shape of crystals (e.g., Vona et al., 2011; Mader et al., 2013). The presence of gas bubbles introduces additional complexity, as viscosity can either increase or decrease with vesicularity (Rahaman et al., 1987; Webb and Dingwell, 1990; Bagdassarov and Dingwell, 1992; Lejeune et al., 1999; Stein and Spera, 2002; Pal, 2003; Rust et al., 2003 Llewellin and Manga 2005; Quane and Russell, 2005; Robert et al., 2008; Quane et al., 2009; Heap et al., 2014). For the same melt chemistry, the evolution of volcanic processes can be influenced by various properties or parameters that control eruptive style in different ways, and volatiles have a central role in this (e.g

magma ascent rate, dissolved and exsolved volatile content, magma rheology, rate of decompression, bubble content) (Cassidy et al., 2018).

In the present study the role of degassing on the rheology of natural obsidians has been investigated through two different experimental approaches, which involves experiments on bubble-bearing magmas. The first set of experiments (*single-stage* experiments) represents a completely new experimental approach, which for the first time allows to observe the rheological behavior of a bubble-bearing magma; post- run analysis of obsidian cores proved that no outgassing phenomena occurred during deformation and that and exsolved H_2O remained into the melt as vesicles. In this condition, the magma can be assumed in a *close-system degassing regime* in which bubbles act to change the viscosity of magma to a certain extent.

The second experimental approach (*double-stage* experiments), was designed to investigated material which underwent a more complex history, having crossed at least one time the glass transition region, so, cooled and then reheated in laboratory as well as in nature. In this case, we observed that the effect of bubble on the viscosity of magma is enhanced and we interpreted this as due to fracturing of bubble walls promoting outgassing.

For this reason, we redefined the experiments as *closed-cell system* (SS) and *open-cell system* (DS). The difference in viscosity between the two subsets increases as a function of porosity reaching about 0.6 log units in viscosity at 50 % porosity. This result indicates that vesicle nature has an important influence on rheological response, and therefore on the evolution of volcanic eruptions and should be then taken into account for the purpose of modeling volcanic eruptions.

The experimental conditions (T_{foam} = 900-1050, T_{def} = 800-750, P =1 atm) could represent the peculiar instances of a dome emplacement or an obsidian lava flow in which the system switches from closed, if bubbles are vapor- filled (SS), to open when outgassing is promoting by micro-cracks development and propagation due to cooling (DS). For both systems, we defined constitutive equations linking viscosity to porosity through a unique parameter (α), which depends on degree of permeable gas flow in the suspensions.

Our experiments also allow us to explore the regime for ductile to brittle transitions in magmas. In general, the presence of pores enhances the fluidity of magmas. At the same time, it decreases the strength of magmas leading to rapid onset of brittle fragmentation (Vona et al., 2013, Vona et al., 2016). Stress/strain conditions and local heterogeneities in the pores/bubble distribution are all factors that can lead to regions of flow and/or brittle behavior and temporal crossing of Tg (Okumura et al., 2009; Cabrera et al., 2011). The crossing of the ductile/brittle transition can induce textural transformation responsible for the two observed apparent bulk viscosities (closed cells/open cells). For instance, during emplacement of a dome, repetitive fracturing and healing of the dome

walls due to extrusion of new magma can promote continuous transitions between open and close system. *Open-system degassing* is in this case linked to permeability increases driven by brittle processes favored by an increase in shear strain rate.

In our study, we suggest that similar brittle processes can be triggered by temperature variations, and this can be applied to both dome emplacement or silicic lava flows. Flow banding in rhyolitic obsidians (Tuffen and Castro, 2009; Dingwell, 2006) has also been interpreted as due to multiple switching from liquid to glassy state and to the repetitive formation of fractures. The decrease in viscosity and strength of magma favors additional crossing of ductile/brittle transition and the formation of new fractures, additional outgassing and further decrease in viscosity in a accelerating cascade effect which could generate complex and unpredictable scenarios.

There are few experimental and theoretical works on magma strength. Typically, the shear strength of natural magma is estimated to be between 10^6 and 10^7 Pa (Tuffen et al., 2003). Experimentally determined values of 10^8 Pa are reported for tensile failure of melts (i.e. glasses above Tg; (Webb and Dingwell, 1990; Mungall et al., 1996; Romano et al., 1996) and 10^{7-8} Pa for non-vesicular rhyolite failing in shear (Okumura et al., 2010). Vasseur et al., (2013) recorded a difference of one order of magnitude in compressive strength for porous glass cores (porosity > 0.25). Romano et al., (1996) found a value of $10^{5.8-6.4}$ Pa for micro-fractured glass (porosity ~ 0.12). Okumura et al., (2010) found out a magma strength values of 10^6 Pa in rhyolite with porosity varies form 0.20 - 0.41. In general, all those experiments suggest that the porosity reduces material strength by 1-2 order of magnitude.

For a pure melt system magma strength at fragmentation can be expressed as $\eta_0\ \dot{\varepsilon} \geq K_0$, where η_0 is the melt viscosity, $\dot{\varepsilon}$ is the strain rate and K_0 is the magma strength of the liquid phase alone. For porous melts, according to Vona et al., (2016) an analogous relation can be expressed as $\eta_{Bulk}\ \dot{\varepsilon} \geq K_\phi$ where η_{Bulk} is the bulk (melt-pores) viscosity, and K_ϕ is the magma strength of the porous melt. Dividing the two equations above and substituting the viscosity model for porous magmas from this study (see Vona et al., 2016 for details), a relation for the variation of K_ϕ as a function of melt porosity can be rewritten in logarithmic form as:

$$\log K_0 - \alpha\ (\phi_f / 1 - \phi_f) \geq \log K_\Phi \qquad (4)$$

Considering $\log K_0 = 10^8$ Pa the strength of the vesicle-free melt, shear strength of our bubble-bearing magmas for both *open-cell* and *closed-cells* system, has been calculated (Fig. 17). As it can be seen, in the case of *open-cell* system, the decrease in the mechanical resistance of the material is greater, and this is attributed to the effects of micro-fractures, in agreement with previous

observations by Romano et al., (1996). In this framework, for similar strain rates, *closed-cell* configuration can support viscous deformation whereas the presence of an *open-cell* condition could promote the onset of brittle deformation, further enhancing possible permeable flow and magma outgassing.

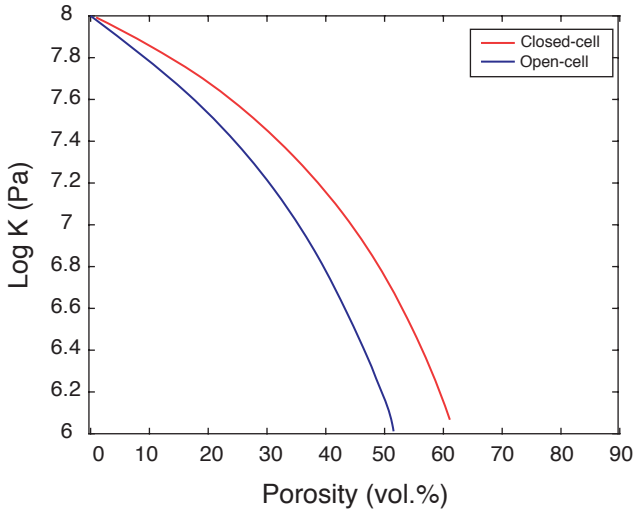

Fig. 17. Variation of porous magma strength (K_ϕ) modeled following Vona et al., 2016 as a function of porosity for the two subsets of data.

During heating of the experiments (in the DS setup), partial annealing of micro-cracks may has occurred. Even considering this scenario, the overall glass/melt would remain weaker by a combination of different thermal expansion (due to water profile inside the glass/melt) and for the total/partial outgassing of the bubbles. Potential annealing effects can therefore be considered negligible for the rheological response.

7. Conclusions

The nucleation of bubbles in volcanic eruptions occurs due to the over-saturation of volatiles as magma rises toward the Earth's surface. The extent of exsolution and the expansion of the volatile phase has a great influence on eruptive styles, and this transient feature strongly controls the rheological properties; indeed bubble content has a critical role on bulk viscosity of magma during eruption, flow and emplacement, but also in the change in styles of volcanic eruptive styles (e.g. from explosive to effusive).

Here we have presented a suite of high temperature experiments on foamed vesiculated cores of natural obsidian material. The new experimental approach allows to investigate not only the relation between porosity and viscosity in natural rhyolitic magmas, but also to further analyze the nature of the pores and its influence on the rheological behavior. *Double-stage* experiments show lower viscosity than *single-stage*, and we suggest that this behavior is a consequence of water loss/wall cracking, which make the material weaker. The same trend among DS experiments was observed in Vona et al., (2016) study, reinforcing our model.

In the present work we have presented an empirical equation able to predict magma viscosity as function of bubble content and pores nature. The proposed viscosity model represents the boundary conditions with two main end-member 1) H_2O-filled bubbles (SS or *closed-cell* system) and ii) empty pores (DS or *open-cell* system). *Single-stage* experiments could be compared with the two-phase region in a hypothetical volcanic conduit (setting aside the effect of pressure on the viscosity of the melt), where bubbles (mostly composed by H_2O and CO_2) are still in the melt; *double-stage* dataset identifies the condition in which outgassing happened (emplacement of lava flow, domes), perhaps promoted by micro-cracks formation. Three main points of the present study can be summarized as it follows: i) In-situ high-temperature degassing and deformation experiments were performed for the first time in order to investigate the rheological behavior of porous melts and viscosity model parameterization is provided for bubble-bearing melts; ii) the nature of the starting material has to be taken into account for parameterization, and lower viscosity values recorded in *double-stage* experiments could be interpreted as due to micro-cracks/gas escape formation during sample quenching; iii) The proposed viscosity models describe the rheological behavior of porous melts and can be applied to different framework (*open-cell* vs. *closed-cell* systems).

In conclusion, is possible to affirm that pore nature, as well as porosity fraction, has to be taken into account when modeling the rheology of multiphase magmas; the different rheological

response can indeed reflect different volcanic environments and influence the eruptive dynamics and emplacement.

Chapter 3

An experimental investigation of H_2O resorption process on degassed rhyolitic melt: definition of the experimental protocol

Abstract: Dissolved and exsolved H_2O in silicate melts plays a crucial role in volcanic eruptions affecting glass properties and magma evolution. It is known that H_2O dissolved in magmas exsolves, trough bubbles nucleation and grow, as it ascents in the volcanic conduit to the Earth surface, moving from higher to lower pressures. Water exsolution is one of the most important processes that drives and influences eruptive styles (e.g. effusive or explosive styles). Nevertheless, it could happen that exsolved H_2O is reabsorbed into the melt phase, if the environmental condition allows it, and this process will be here after called "resorption". If the resorption process occurs, physical and chemical properties of the melt have to be reassessed and rescaled at the new water/bubble content conditions.

In this study high temperature degassing experiments were performed in order to explore the water resorption process during cooling. In particular, the objective of the work was to identify the minimum cooling rate at which resorption processes are occurring. We present a suite of high-temperature (950–850 °C) degassing experiments performed on 5 × 5 mm cores of rhyolitic obsidian from Hrafntinnuhryggur, Krafla, Iceland, under atmospheric pressure using TMA. During each experiment obsidian cores were heated above the glass transition temperature (Tg), held for 5 hours at T_{foam}= 950 °C. After this first phase (the same for each experiment), the sample is subject to different cooling and heating cycles. In each heating/cooling cycle the sample is heated to T_{foam}= 950 °C, held for 0.5- 2 hours at the dwell T, then the temperature is lowered (T_{cool} = 850 °C) and the core is held again from 2 to 0.5 hours at T=850°C; after this, cores are heated again at T_{foam} = 950 °C and the cycle starts again. During the phase of cooling, temperature was lowered at different cooling rates (50 – 20 -10 - 5 -2 °C). During each heating phase the volume of the samples increased as H_2O vapor-filled bubbles nucleated and expanded, while during the cooling it decreased due to bubbles shrinking and thermal contraction of gas/melt. Additional evidence is needed to discern if resorption really happened or decrease in volume is linked to other factors (e.g. expansivity of H_2O, thermal expansion of the material, viscous relaxation of the material).

1. Introduction

All magmas contain dissolved volatiles that strongly control magmatic and volcanic processes. When magma rises, volatiles exsolve, and the extent of their exsolution and expansion influences volcanic processes from eruptive styles to post-eruptive volcanic processes (Sparks et al. 1999; Castro et al. 2005; Robert et al. 2008; Kennedy et al. 2010). Exsolution of water occurs as the magma becomes oversaturated as pressure decreases. During exolution, the associated loss of H_2O from the melt can cause a rapid and substantial rise in the Tg on the melt reducing the Tg window. On the other hand, there is a wide range of volcanic environments in which exolved H_2O can "turn back" in the melt, for example if the cooling is slow enough to induce H_2O resorption in the silicate melt. Ryan et al., (2015a) recently provided a thermodynamic model for the temperature dependence of H_2O solubility at low pressure (P= 0.1 MPa) exploring the effects of retrograde solubility on a variety of volcanic processes; in that study resorption process was qualitatively estimated using the well-know inversely proportional relationship between H_2O content and T, where the rate of sample volume change (increase porosity) was strictly dependent on experimental T and dwell time. More in details, the initial increase in sample volume was linked to bubble nucleation and growth regime and a response to an initial H_2O-oversaturation at 1-atm and T_{foam}. The volume change, thus porosity, was considered inversely proportional to the equilibrium concentration of H_2O in the glass; this meant that for higher temperature the extent of exsolved water was greater (which corresponded to greater porosity and volume change) conversely, as the temperature decreased the amount of exolved H_2O decreased, and so the porosity and the volume change.

All volcanic systems generally move from high to low temperature, in systems where cooling timescales are slow enough to facilitate H_2O diffusion in silicate melts; the melts have the opportunity to resorb H_2O. The retrograde solubility of H_2O provides a means of expanding the melt field relative to the glassy state. The consequence of this is to reduce the effective Tg of the melt allowing for further uptake of H_2O with cooling. The resorption process could be important in superficial volcanic deposits or within volcanic conduits as well as when investigating welding of pyroclastic deposits, or during the emplacement of lava flow of silicic melts. Indeed, recent studies of welding processes and timescales have emphasized the role H_2O plays in inducing or prolonging welding (Friedman et al. 1963; Sparks et al. 1999; Giordano et al. 2005; Grunder and Russell 2005; Keating 2005; Robert et al. 2008; Kolzenburg and Russell 2014). The rehydration causes a concomitant viscosity reduction and, thus, facilitates welding. Forensic investigations of storage and fragmentation depths of eruption dynamics are commonly based on measured H_2O contents in

melt inclusions or glasses to estimate pressure (Atlas et al. 2006; Rust and Cashman 2007; Wright et al. 2007). These studies could be further constrained by considering the *T*-dependence of H_2O solubility as noted by McIntosh et al. (2014). As in welding studies, many forensic volcanology studies have assumed isothermal conditions (Rust and Cashman 2007; Wright et al. 2007) constrained by geothermometry but the considerations of retrograde solubility can provide lower and upper bounds on estimated fragmentation depths.

In order to further investigate water resorption processes, a new suite of high temperature experiments were performed in this study at the same pressure condition (P = 0.1 MPa) and on the same natural obsidian cores used by Ryan et al., (2015a), using the vertical dilatometer (TMA). These new experiments concerned a foaming phase, at the same target temperature (T_{foam} = 950 °C) and a cooling phase at the T_{cool} = 850 °C. Several cycles of heating and cooling were applied to the samples with different cooling rate (50 – 20 -10 -5- 2 °C/min). This procedure was adopted in order to define a cooling regime where (1) the bubble population could 'respond' to cooling (bubble volume decreases with resorption). Here we present the preliminary results of this study; nevertheless further measurements are necessary to fully explore the effect of heating/cooling on natural rhyolitic melts at atmospheric conditions.

2. Material & Methods

The starting material is the same previously described and characterized by Tuffen and Castro (2009), Ryan et al. (2015a, 2015b) and Vona et al. (2016) and in Chapter 2 of the present thesis. It is a natural bubble and crystal free rhyolitic obsidian from Hrafntinnuhryggur, Krafla, Iceland, containing 0.11(4) wt.% H_2O (Ryan et al., 2015a, 2015b). Cylindrical cores (5x5 mm) were drilled, trimmed, and the ends ground to make parallel polished end-surfaces. The physical properties of cores were measured before and after the experiment. Initial length (L_0), diameter (D_0) and volume (V_0) were determined using a digital caliper, mass (m_0) with a high-precision balance. Initial porosity (ϕ_0) is assumed equal to zero (below detection).

High temperature foaming experiments have been performed using a Setaram Setsys vertical dilatometer (TMA) at Experimental Volcanology Lab (EVPLab) at Roma Tre University (Fig. 1). The device is composed by a heating chamber (P = 1 atm and oxygen fugacity fixed by continuous argon gas flux), where the sample is located and supported by an alumina base connected to a measuring head. Five experiments were conducted in order to investigate H_2O resorption due to cooling periods (at defined rates) where sample length (proxy for sample volume and porosity) is continuously measured through the Linear Variable Displacement Transducer (LVDT) sitting on

the sample for the whole experiment (Fig. 1a). The software Setsoft is used to set the experimental parameters (e.g. temperature, heating/cooling rate, probe weight, experiment time).

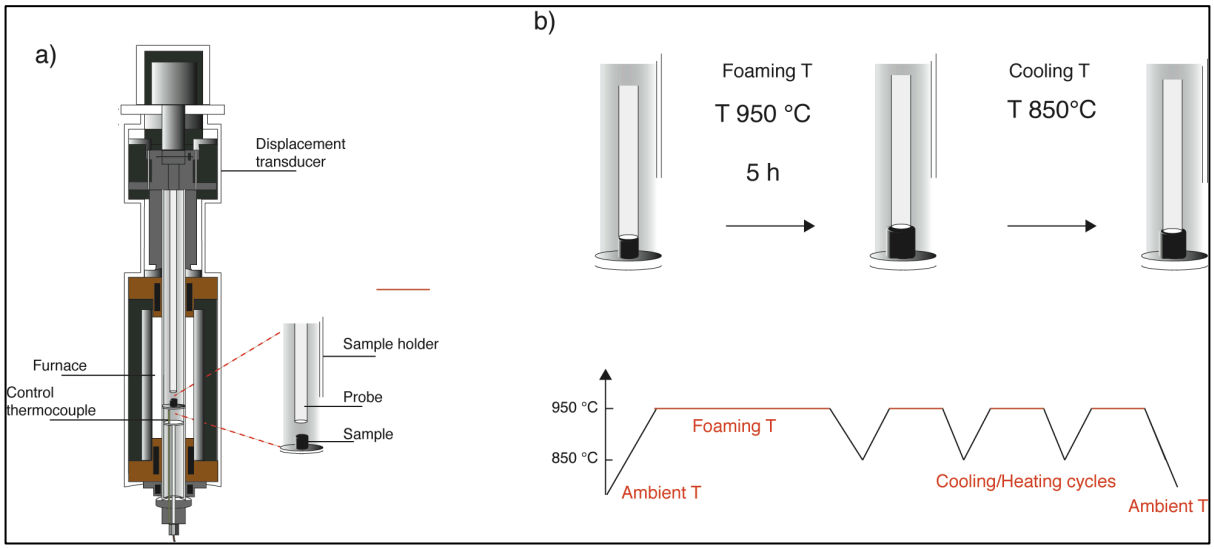

Figure 1. Sketch of the adopted setup. a) Setaram Setsys vertical dilatometer (TMA). b) Detail of the experimental setup used in the present study. c) Path of the variation of temperature resorption experiments.

Each experiment included a foaming phase where obsidian cores were heated with a rate of 5°C/min from room temperature to a target temperature above Tg (T_{foam} = 950 °C) and a dwell time at T_{foam} (t = 5 hours) (Fig. 1b). As the temperature increases, the volume of the foaming samples increases, because H_2O vapor-filled bubbles nucleate and expand. After this first step, the sample was submit to several cycles of cooling and heating from T_{foam} = 950 °C to a target cooling temperature of T_{cool} = 850 °C. The two-target temperatures (T_{foam} and T_{cool}) are the same for all the experiments. The objective of the experiments was to identify the minimum cooling rate at which resorption processes can operate. The extent of resorption is measured by the shortening of the core axes during cooling.

The novelty of the experimental approach required several tests in order to establish the best technique. For this reason, experiments were conducted changing several parameters as dwell time after the first foaming phase (which was maintained always 5h) and cooling rates.

The 5 experiments performed had the following features (see Tab.1 for details):

1) RES2: Cooling-heating cycles – variable cooling rates, slow heating (1 °C/min)
2) RES4: Cooling-heating cycles – variable cooling rates, fast heating (50 C/min);

3) RES5: Cooling-heating cycles – variable cooling rates, heating rates matching cooling rates;
4) RES6: One cooling rate – cool at 10 °C/min;
5) RES7: Control (no cooling);

Table 1. Initial physical properties of the pre-run cores used in high temperature (T) experiments and experimental conditions. L_0 and D_0 are respectively the the initial l lenght and diameter measured with calliper. V_0 is the estimated initial volume from the geometrical features.

Intial physical properties				Experimental conditions	
Sample	**L0** (mm)	**D0** (mm)	**V0** $(mm)^3$	**Heating rate °C/min 950 °C**	**Cooling rate °C/min 850 °C**
RES 2	5.28	4.90	99.58	1	50
				1	20
				1	10
				1	5
				1	
RES 4	5.51	4.94	105.59	50	50
				50	20
				50	10
				50	5
				50	2
				50	
RES 5	5.63	4.91	106.48		
				50	50
				20	20
				10	10
				5	5
				2	2
RES 6	5.73	4.90	108.14	10	10
				5	5
RES 7	4.79	4.90	90.47	5	10

Composition (wt.%) of obsidian (ρ =2.394 gcm−3) from Hrafntinnuhryggur, Krafla, Iceland (Tuffen and Castro, 2009): SiO_2 (75.23), TiO_2 (0.23), Al_2O_3 (12.00), FeO (3.28), MnO (0.11), MgO (0.10), CaO (1.66), Na_2O (4.15), K_2O (2.75), H_2O (0.114).

In all experiments the sample length through the heating and foaming stage and through the cooling stage(s) was continuously monitored. For each experiment a blank measurement (same thermal treatment and no sample) was performed to correct sample raw data and get absolute displacement values. The final volume at the end of the experiment, either 'foaming' (V_i) or 'foaming + deformation' (V_f) was analyzed using a Micromeritics AccuPyc II 1340 He-pycnometer.

3. Preliminary results and discussion

The high-T experiments cause exsolution of volatiles and volume increase (ΔV) due to bubble formation and growth. This is manifested by a systematic increase in sample height (i.e. displacement, ΔL) with increasing dwell time (t) until a maximum stable value is reached.

The rate of sample volume change (dV/dt) and the time to achieve the equilibrium plateau depends on T_{foam}. In this study the choice of T_{foam} (950 °C) and t (5 hours) is based on water solubility experiments by Ryan et al. (2015a, 2015b) conducted on the same obsidian material.

The changes in length recorded by the probe, were translated in volume change following the 1:1 relationship between axial (L_1/L_0) and radial (D_1/D_0) strain (i.e. isotropic expansion). This relation was used to estimate the variation in volume (ΔV) and porosity (ϕ) during the different cycles of heating and cooling of each experiment. This permitted calculation of the extent of volume change a check on whether or not resorption happened during the cooling stage. The variation in porosity from the first heating cycle to the final cooling stage is around the 2 vol.% in each sample; the axial strain varies from a minimum 0.04 to 0.11 in the whole dataset.

As each experiment has been performed following different procedures, results are here individually presented.

RES2: In this experiment (Fig. 2) the heating rate was set at 5 °C/min up to 850°C and then slowed down to 1 °C/min from 850 to 950 °C to avoid overshooting problems. The sample was held at 950 °C for 5 hour and then cooled to 850°C. Then, different cycles of cooling and heating were applied. Cooling rates were 50 – 20 -10 -5 C°/min and heating rate was always 1°C /min. At the end of each heating stage, sample was held at temperature for increasing amount of time (0.5 -1-1.5 - 2 hours). Sample was subjected to substantial foaming so we could easily detect changes in sample length related to cooling/resorption. Looking at the recorded data, we observe cycles of decreasing and increasing displacement connected to the cooling and heating of the sample. The decrease in displacement does not exactly match the cooling time as the sample continues to shrink even after the cooling stage is finished and the heating stage has initiated. Each phase of increasing displacement ends with a plateau, which does not recover the original value of height.

Calculated porosity values (from the volume estimation), varies from the first cycle to the last cooling from 59.53 to 55.07 vol.%. The decrease in the plateau value could be attributed to a viscous relaxation process due to the long duration of the experiment caused by the slow heating rate or to incomplete recovery after resorption. The relative minimum in displacement trace during cooling can be attributed to: 1) resorption and porosity loss, 2) thermal contraction of the liquid, 3) thermal contraction of the gas phase.

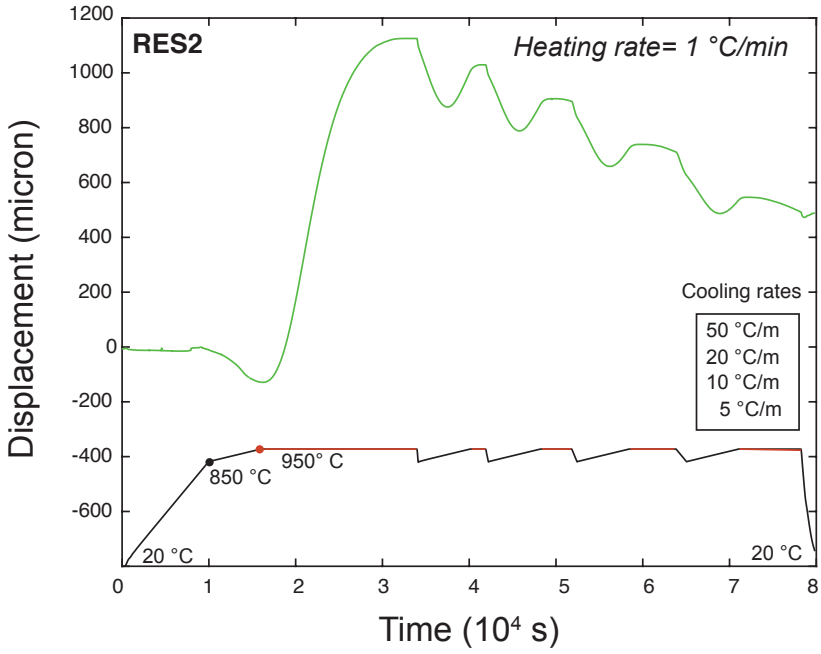

Figure 2. Displacement vs. time of RES 2. In this experiment the heating rate of each heating step is 1 °C/min, while the cooling rate (T_{cool}=850 °C) varies from 50 to 5 °C/min.

RES4: In this experiment (Fig. 3) the heating rate was set at 5 °C/min up to 850°C and then slowed down to 1 °C/min from 850 to 950 °C. The experiment was held at 950 °C for 5 hour and then cooled to 850°C. Then different cycles of cooling and heating compared to RES2 were applied. In this case (Fig. 3), in order to avoid viscous relaxation processes, the heating rate was set at 50°C/min and the cooling rates were 50 – 20 -10 - 5 and 2 C°/min. Once again sample was subjected to substantial foaming; in this experiment (and also in the following) the dwell time after the at the heating temperature (950°C) is always kept at 0.5 hour. With respect to the previous experiment, we still observe cycles of increase and decrease in displacement values. At higher cooling rate (up to 20°C/min), we observe good recovery of the displacement after heating. At lower cooling rate we observe a partial recovery maybe due to the longer duration of the experiment and concomitant viscous relaxation or again to incomplete recovery after resorption.

The relative minimum in displacement trace during cooling can, as in the previous experiment, be attributed to: 1) resorption and porosity loss, 2) thermal contraction of the liquid, 3) thermal contraction of the gas phase. In this experiment porosity varies from 58.65 to 56.99 vol.% in the last cooling phase.

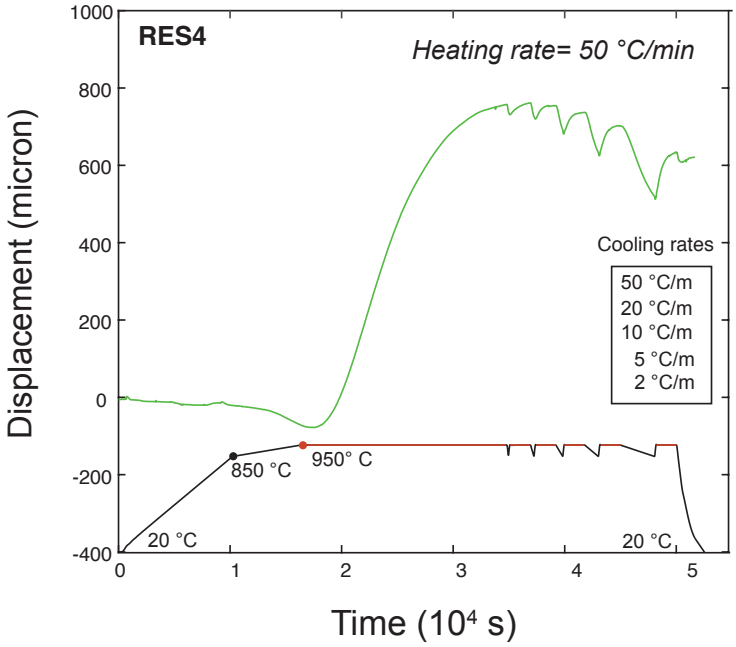

Figure 3. Shows RES 4 experiment in heating rate of each heating step is 50 °C/min, and cooling rate (T_{cool}=850 °C varies from 50 to 2 °C/min.

RES5: In order to avoid disequilibrium processes affecting the plateau recovery, due to difference in cooling and heating stages, in this experiment we set identical rates (50 – 20 -10 - 5 - 2 C°/min) (Fig.4). Once again sample was subjected to substantial foaming due to the initial increase in temperature. The first cycle of heating was performed at the same conditions as for the previous experiments. With respect to the previous measurements, we still observe cycles of increase and decrease in displacement values. However, in this case, we observe a good recovery of the displacement after heating. This result indicates that the experiment duration is short enough to avoid viscous relaxation but long enough to allow possible recover from resorption and bubble shrinking via bubble growing and thermal expansion of both melt and gas phases. At the last and slowest heating/cooling cycle (2 °C/min), the initial plateau is not recovered and this again can be due to viscous relaxation processes. The relative minimum in displacement trace during cooling can be attributed to: 1) resorption and porosity loss, 2) thermal contraction of the liquid, 3) thermal contraction of the gas phase. The decrease in porosity goes from 56.28 to 54.73 vol.%.

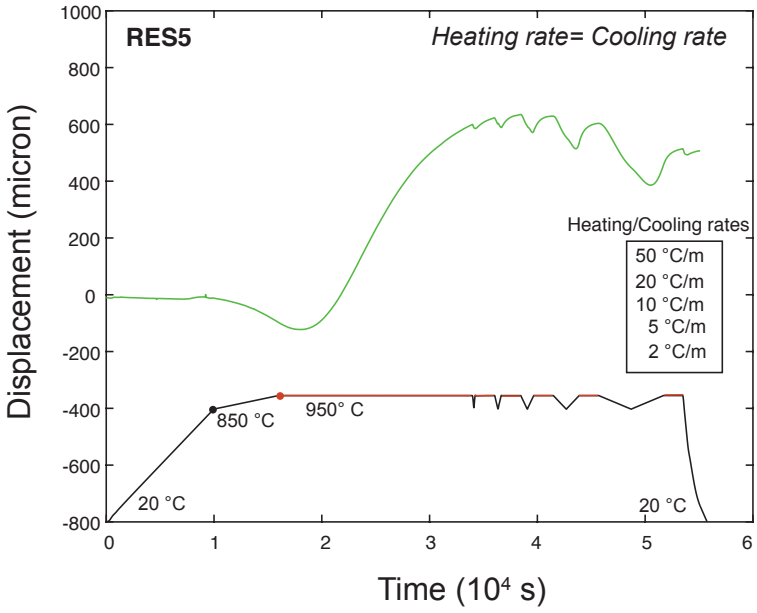

Figure 4. RES5 experiment is displayed as displacement vs. time. For each cycle cooling and heating rates match, varying from 50 to 2 °C/m.

RES6: Fig. 5 shows the last experiment in which the heating and cooling rates are matched. The first cycle of heating was performed at the same conditions as in the previous experiments. To test the time dependent behavior, and shorten the overall duration of the experiment, we decided to perform heating/cooling cycles only at 10 – 5 – 2 °C/min. In contrast to the previous experiment, during the cycle at 5 °C/min, the displacement recovers the initial plateau value. We attribute this to the shorter duration of the experiment anticipating the onset of viscous relaxation. Again the relative minimum in the displacement trace during cooling can be attributed to: 1) resorption and porosity loss, 2) thermal contraction of the liquid, 3) thermal contraction of the gas phase. The first calculated porosity value is 51.71, while the last value after cooling is 50.36 vol.%.

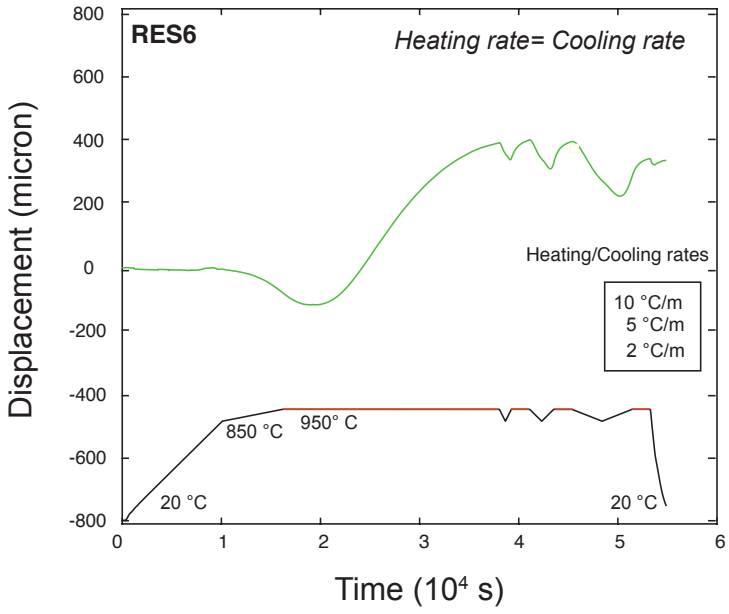

Figure 5. RES6 trace is shown as displacement vs. time. Even in this case heating and the cooling rates match, starting from 10 °C/min to 2 °C/min.

Each variation in length after the heating phase (950° C) and after the cooling stage (850° C) was estimated from the position of the probe recorded during the experiment (Tab. 2); then the variation in volume was extrapolated using the relation 1:1 between axial and radial strain. The difference in length and volume between each step, due to the heating and the cooling stages is also reported. At the end of each experiment, the final volume of the obsidian core was measured with He-Pycnometry techniques and compared with the calculated one. There is a a good correspondence between the two values that indicates that the estimation of volume was correct.

Table 2. Measured and calculated final physical properties of obsidian cores after each heating/cooling cycle.The calculated lenght (mm) and volume (mm^3) are reported named L_x for the heating stage (950° C) and R_x for the cooling stage (850 °C). The suffix L or R is used also for the estimated volume and porosity. The difference in lenght, volume and porosity between each cylce are expressed as ΔL, ΔV and ΔΦ. There are also reported the final lenght and volume measured with He-Pycnometer ate the end of each experiment.

Sample	950° C						850 °C						950° - 850° C			Mesured final properties		
	*Length (mm)		*Volume (mm^3)		*Φ (%)		*Length (mm)		*Volume (mm^3)		*Φ (%)		ΔL	ΔV	ΔΦ	[b]Lf (mm)	[b]Vf (mm)	[b] Φ (%)
RES 2	L1	6.38	$V_{L}1$	246.07	$Φ_{L}1$	59.53	R1	6.13	$V_{R}1$	236.51	$Φ_{R}1$	57.89	0.25	9.56	1.64	5.74	221.62	55.07
	L2	6.29	$V_{L}2$	242.32	$Φ_{L}2$	58.90	R2	6.05	$V_{R}2$	233.05	$Φ_{R}2$	57.27	0.24	9.27	1.64			
	L3	6.16	$V_{L}3$	237.49	$Φ_{L}3$	58.07	R3	5.92	$V_{R}3$	227.97	$Φ_{R}3$	56.32	0.25	9.52	1.75			
	L4	6.00	$V_{L}4$	231.02	$Φ_{L}4$	56.90	R4	5.74	$V_{R}4$	221.62	$Φ_{R}4$	55.07	0.25	9.41	1.83			
	L5	5.80	$V_{L}5$	223.88	$Φ_{L}5$	55.52												
RES 4	L1	6.31	$V_{L}1$	255.36	$Φ_{L}1$	58.65	R1	6.28	$V_{R}1$	254.27	$Φ_{R}1$	58.47	0.03	1.09	0.18	6.06	249.81	56.99
	L2	6.31	$V_{L}2$	255.51	$Φ_{L}2$	58.67	R2	6.27	$V_{R}2$	253.77	$Φ_{R}2$	58.39	0.04	1.74	0.28			
	L3	6.30	$V_{L}3$	255.18	$Φ_{L}3$	58.62	R3	6.23	$V_{R}3$	252.19	$Φ_{R}3$	58.13	0.07	2.99	0.49			
	L4	6.29	$V_{L}4$	254.46	$Φ_{L}4$	58.51	R4	6.18	$V_{R}4$	249.81	$Φ_{R}4$	57.73	0.11	4.65	0.77			
	L5	6.25	$V_{L}5$	253.00	$Φ_{L}5$	58.26	R5	6.06	$V_{R}5$	249.81	$Φ_{R}5$	56.99	0.19	3.19	1.28			
	L6	6.18	$V_{L}6$	250.30	$Φ_{L}6$	58.89												
RES 5	L1	6.28	$V_{L}1$	245.48	$Φ_{L}1$	56.62	R1	6.27	$V_{R}1$	244.93	$Φ_{R}1$	56.53	0.01	0.55	0.10	6.07	241.94	55.10
	L2	6.31	$V_{L}2$	246.39	$Φ_{L}2$	56.78	R2	6.27	$V_{R}2$	245.04	$Φ_{R}2$	56.55	0.03	1.35	0.24			
	L3	6.32	$V_{L}3$	246.82	$Φ_{L}3$	56.86	R3	6.25	$V_{R}3$	244.28	$Φ_{R}3$	56.41	0.06	2.54	0.45			
	L4	6.31	$V_{L}4$	246.57	$Φ_{L}4$	56.82	R4	6.20	$V_{R}4$	241.94	$Φ_{R}4$	55.99	0.11	4.63	0.83			
	L5	6.29	$V_{L}5$	245.48	$Φ_{L}5$	56.63	R5	6.07	$V_{R}5$	241.94	$Φ_{R}5$	55.10	0.22	3.54	1.53			
	L6	6.20	$V_{L}6$	242.12	$Φ_{L}6$	57.41												
																5.98	220.17	50.88
RES 6	L1	6.15	$V_{L}1$	226.28	$Φ_{L}1$	52.21	R1	6.10	$V_{R}1$	224.31	$Φ_{R}1$	51.79	0.05	1.97	0.42			
	L2	6.16	$V_{L}2$	226.59	$Φ_{L}2$	52.27	R2	6.07	$V_{R}2$	223.18	$Φ_{R}2$	51.55	0.09	3.41	0.73			
	L3	6.15	$V_{L}3$	226.33	$Φ_{L}3$	52.22	R3	5.98	$V_{R}3$	220.17	$Φ_{R}3$	50.88	0.17	6.16	1.34			
	L4	6.10	$V_{L}4$	224.48	$Φ_{L}4$	51.82												

[a] Final physical properties geometrically calculated; [b] Final physical properties measured with calliper and Pycnometer

The extent of exsolution of H_2O fluid at constant T is manifested by a change in volume (increased porosity) that depends on the experimental dwell time and on the 1-atm solubility of H_2O at that T (Fig. 1). The bubbles formed are assumed to be dominantly H_2O (Ryan et al., 2015a).

The experimental curves of each experiment show a consistent increase in displacement during the heating phase and decrease during cooling. In principle the increase in length during heating can be attributed to foaming while the decrease in length during cooling could be attributed to resorption, being the solubility at 850°C lower than the solubility at 950°C. Nevertheless, other factors have to be taken into account to prove that resorption processes affect rhyolitic cores when the temperature decreases.

The increase/decrease of sample volume due to change in temperature (100 °C), can be indeed influenced by four main factors:

1) Thermal expansion of H_2O in gas bubbles;
2) Thermal expansion of the melt;
3) Viscous relaxation of the bulk material;
4) Volatile diffusion to/from gas bubbles (foaming/resorption).

3.1 Gas thermal expansivity

To evaluate the relative contribution of gas expansion to the overall volume change observed in the experiments, we performed a series of calculations listed below:

1) H_2O solubility was calculated at 850 and 950°C according to the model of Ryan et al. (2015a) and Liu et al. (2005) (column 2, row 1 in Table 3 , Solubility limits in wt%);

2) The excess of water (respect to the solubility values) was calculated considering an original water content of 0.114 wt% both at 850 and 950°C;

3) The excess water was transformed from wt% to moles (column 3, row 1 in Table 3, moles of H_2O in bubbles);

4) The volume of gas was then estimated according to the gas equation of state the PV=nRT, considering P=101828 Pa and R= 8.314472 m^3 Pa K^{-1} mol-^{1}; (column 2, row 2, Table 3).

5) The volume change (ΔV), from 850 to 950 °C due to the expansivity of gas considering an initial excess water at equilibrium at 850°C was calculated (gas expansion).; (column 2; row 3)

6) The volume change (ΔV), from 950 to 850 °C due to the expansivity of gas considering an initial excess water at equilibrium at 950°C was calculated (gas contraction); (column 2; row 3)

7) Calcualted volume changes (ΔV) were then compared to the ΔV measured for sample RES6; (column 3; row 3)

In the RES6 case, we only consider the volume change from 950 to 850°C (decrease in volume), so we can compare our results with the ΔV calculated starting from equilibrium values at 950°C and for a similar decrease in temperature from 950 to 850 °C (24.17 and 11.51 mm^3).

The observed shrinkage in volume is always smaller than the calculated one for gas thermal contraction. Probably equilibrium was not reached during this experiment and the decrease in volume due to thermal contraction of the gas was only partial. In this situation, even if resorption occurred (further decrease in volume), it would be impossible to discriminate from gas contraction.

Table 3. Summary of the gas expansivity calculation using Ryan et al. (2015a) and Liu et al. (2005) models.

	Solubility limits in wt%		**moles of H_2O in bubbles (assuming all excess H_2O is in bubbles)**		
	LIU	RYAN		LIU	RYAN
850° C	0.101	0.111	850° C	1.83E-06	4.23E-07
950° C	0.093	0.104	950° C	2.96E-06	1.41E-06
			DIFFERENCE	1.13E-06	9.87E-07
	Volume of H_2O (mm^3) in bubbles 850° C solubility limit		**Volume of H_2O (mm^3) in bubbles 950° C solubility limit**		
	LIU	RYAN		LIU	RYAN
850° C	168.03	38.77	850° C	271.45	129.25
950° C	182.99	42.22	950° C	295.62	140.76
DIFFERENCE	14.96	3.45	DIFFERENCE	24.17	11.51
	Volume change (ΔV mm^3) T-Dependent expansivity of H_2O		**Volume change (ΔV mm^3) in RES6**		
	LIU	RYAN		V1 - V_res1	1.97
Expansion (850° - 950° C)	14.96	3.45		V2 - V_res2	3.41
Contraction (950° - 850° C)	24.17	11.51		V3 - V_res3	6.16

3.2 Melt thermal expansivity

Thermal expansivity of the melt has been calculated using the density model of Lange and Carmichael (1987) on the same sample RES 6. The estimation of the density is based on the molecular mass, the number of moles and the fractional volume relative to each chemical component. For RES 6 the density of the material at 850 and 950 °C is 2431.70 and 2420.69 Kg/m^3 respectively. From melt density and mass it is possible to estimate the volume of the melt phase at each target temperature and the difference between. Indeed the volume of the melt at 850 °C is 103.90 mm^3 while at 950 °C is 104.37 mm^3; the difference between the two values is 0.47 mm^3, which compared to the difference of volume recorded from the measurements is negligible. Indeed,

taking into account the first heating/cooling cycle of RES6, the difference in volume at 950°C (226.28 mm^3) and at 850 °C (224.31) is 1.97 mm^3, which is larger than the estimated volume value. In this case it is possible to consider the thermal expansivity of the material a secondary factor.

3.3 Porosity

Considering both gas and melt thermal expansion, calculation of final porosity (Φ) at 850 and 950°C can be performed according to the formula:

$$\Phi = \frac{V_{gas}}{V_{melt} + V_{gas}}$$

Gas volume at 850 and 950 °C was calculated considering the water solubility model of Ryan et al. (2015b) and the thermal expansivity of the gas, as described in the 3.1 section. Melt volume was calculated as in section 3.2, taking into account Lange and Carmichael (1987) model and thermal expansivity of the melt.

Considering the two target temperatures, the expected Φ should be 27.18 vol.% at 850 °C and 57.42 vol.% at 950 °C. Taking into account again the sample RES 6, the value at 950 °C is 52.21 vol.%, which can be consider comparable with the estimated one; on the contrary the expected value at 850 °C is lower than the measured, that is 51.79 vol.%. This observation suggests that water that goes into bubbles at 950 °C does not "turn back" completely during the cooling at 850 °C, and such variation in volume is some way influenced by the previous foaming phase.

The duration of the experiment was again not long enough to reach equilibrium condition and allow resorption/contraction to take place.

With the adopted method it was not possible to discriminate between the resorption of water (which would decrease the volume of the sample) and the gas contraction during cooling (which would also decrease the volume of the sample). The experimental approach needed to be improved.

As a further step for the determination of the resorption process we designed another type of experiments, which is described below:

RES7: This last experiments was performed simplifying the experimental strategy, imposing only one cycle of heating and cooling. The initial heating rate was set at 5 °C/min and the foaming stage at T_{foam}= 950 °C lasted 10 hours; after that, the temperature was lowered from 950 °C to

T_{cool}= 850 ° C with a cooling rate of 10 °C/min. In this experiment, only a small amount of foaming was observed (as it can be inferred from the small increase in the displacement during time), probably due to the heterogeneous distribution of water in the pristine obsidian block. Despite that, the sample shows shortening during cooling and approaches a new plateau, at the temperature 850 °C (Fig. 6).

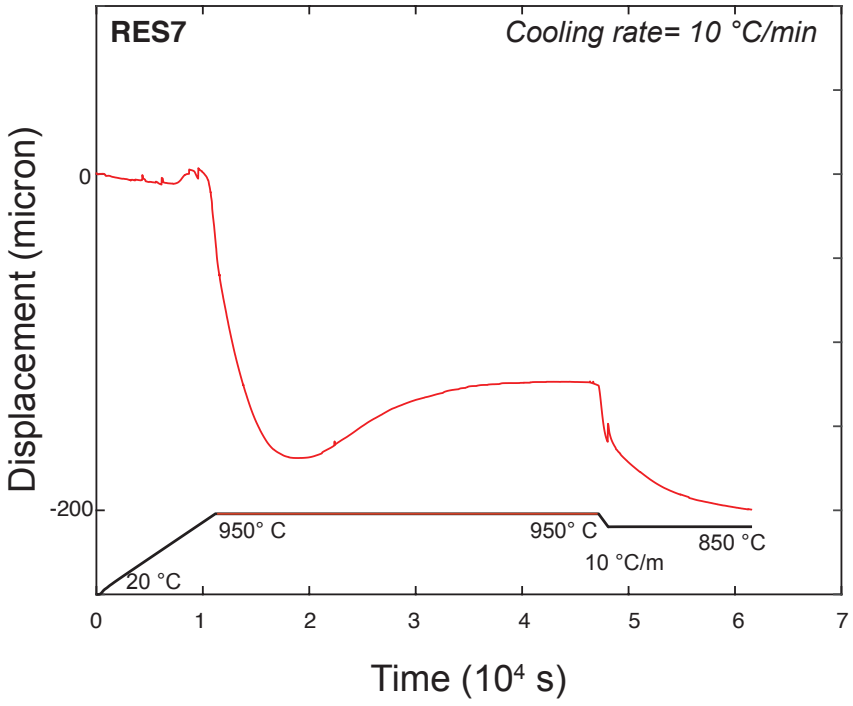

Figure 6. Displacement vs. time for RES 7 experiment. T_{foam}= 950; T_{cool}= 850 ° C with a cooling rate of 10 °C/min.

Also in this case, we calculated the variation in volume (contraction) during cooling from 950 to 850 °C. Differently from the other experiments, equilibrium conditions seem to have occurred after a 5 hours period and ΔV calculated is 1.19 mm^3.

As we can see in Table 3, the minimum ΔV calculated due to simple gas contraction from 950 to 850 °C, assuming an original water content of 0.115 wt% is 11.51 mm^3, far greater than the ΔV measured in this experiment. However, given the small amount of foaming observed for this sample, we could expect a lower water content compared to the other samples and therefore smaller ΔV. As we do not have a precise knowledge of the original water content of our sample, this calculation cannot be performed and the exact contribution of gas contraction versus resorption cannot be evaluated.

To overcome the problem, we performed a two steps experiment ("double heating" experiment: RES 8). In the first step, the obsidian core was heated at 950 °C at 5°/min and held for 10 hours, during which bubbles nucleation and growth was testified by the increase in sample volume; then the core was rapidly quenched (50° C/min) and the new volume was measured with He - Pycnometer. The initial volume (pre-foamed cores) is V_0= 101.52 mm^3 (geometrically estimated), and the new measured volume V_{950}= 195.00 mm^3, which corresponds to a porosity value of 47.94 %vol. From those measurements it was possible to calculate the exact amount of water (moles) present in the sample at that given temperature with the formula PV=nRT, which is 5.12 10^{-4} number of moles.

At this point the foamed and quenched core was re-heated again at 850° C and held for 20 hours; at the end of the experiment the volume of the re-foamed sample was once again measured trough He-Pycnometer, and the measured values was V_{850}= 167.50 mm^3, corresponding to a porosity of 39.39 %vol and 5.48 10^{-4} number of moles of H_2O. The difference in volume (V_{950} – V_{850}) is about 27.50 mm^3 (a decrease of 14.10 % from 950 to 850°C) with a difference in porosity of 8.55 vol.%. Taking into account the previous calculation where the variation in volume could be due to thermal expansion of 1) H_2O in gas bubbles and 2) silicate melt, which are respectively 11.51 mm^3 and 1.97 mm^3, it is possible to estimate the variation in volume due to H_2O resorption contribution, that is 14.02 mm^3.

This "updated" experimental approach seems to be more appropriate as a possible resorption contribution was measured. This could be due to the longer period (20 h) at which the sample was held at the new temperature (850° C) after the first foaming phase (950° C), allowing to reach equilibrium conditions at the given temperature.

Further experiments will be necessary in the future to quantitavely constrain the conditions of temperatures and cooling rate where the resorption process occurs.

Summary

All volcanic systems cool and if the cooling is slow enough the melts are subject to rehydration. Rehydration allows expanding the melt window and lowering the Tg. This process can be applied to a wide variety of volcanic environments (conduits, domes, ignimbrites, and lavas) and thus a to range of processes (welding, sealing/permeability collapse, and flow dynamics).

In this thesis five experiments have been conducted on obsidian cores heated (above Tg) at T_{foam} = 950 °C and subsequently cooled at T_{cool} = 850 °C with different cooling rates in order to find the smallest cooling rate at which resorption occurs. The experiments where heating and cooling rates were cyclic (RES2, RES4, RES5, RES6) were not satisfactory because the equilibrium

conditions were not reached after the cooling phase, and the different contributions causing volume contraction could not be separated. As a result, a different experiment was performed with a single heating/cooling cycle at the cooling rate of 10 °C/min, but although in this case the equilibrium was reached, the small amount of foaming did not allow again to resolve the resorption phenomena.

In order to overcome this problem, we designed a two steps experiment. In the first experiment, the cycle of heating and cooling is performed to establish the exact amount of water present in the sample, through ΔV measurements. In the second experiment, performed on the same sample immediately after quenching, the cycle of heating and cooling is performed to estimate the change in volume due to decrease in temperature and the relative contribution of the different factors (liquid and gas thermal expansion and water resorption). These two separate steps allowed to track in a quantitative manner, the H_2O resorption process in rhyolitic material. Further experiments will be necessary in the future to quantitatively constrain the conditions of temperatures and cooling rate where the resorption process occurs.

Chapter 4

Final remarks

The style and evolution of volcanic eruption are dictated by the fluid mechanics that govern magma ascent (Gonnerman and Manga, 2007). All magmas stored in a magma chamber contain dissolved volatile species that drive eruption dynamics; the melt within the magma chamber may already be supersaturated in volatiles and contain a pre-eruptive exsolved gas phase (Wallace et al. 1995), or it may become supersaturated upon ascent-driven decompression, causing bubbles to nucleate at the exsolution depth and to grow as the magma continues to rise.

Dissolved and exsolved volatiles strongly affect the thermodynamic and physical properties of the melt and dramatically influence magmatic and volcanic processes. Water (H_2O) is the most relevant species in natural melts and has a great influence, (even at low concentration) on a variety of thermodynamic and physical properties (Behrens and Zhang, 2009; Giordano et al., 2015; Lange and Carmichael, 1990; Poe et al., 2012; Scaillet and Macdonald, 2001; Stebbins et al., 1995) and on bulk properties such as viscosity and density (Bouhifd et al., 2015; Dingwell et al., 1996; Lange and Carmichael, 1990; Whittington et al., 2000) both as dissolved and exsolved species.

Degassing processes have a crucial role on the rheological behavior of magma and volcanic dynamics. In this thesis, the results of a meticulous study concerning the degassing process in silicic melts have been presented.

In order to understand the degassing effects, the first step was to properly quantify water content. Although, many studies and techniques exist (FTIR, KFT, TGA), dealing with measurements of water in glasses/melt, a universally accepted methodology able to properly determine water content in multicomponent natural volcanic samples is still not available. In order to fill this gap, a general model for water quantification in natural hydrous glass was developed using Raman spectroscopy. The proposed model allows to estimate water content of natural glassy samples for a wide range of compositions, from basalt to rhyolite including alkali- and iron-rich compositions. The HW/LW ratio versus H_2O content of the different samples defines a slope (A coefficient) which is strongly dependent on chemical composition, thus different A parameters have to be taken into account for water estimation, in relation to the analyzed composition using the formula $H_2O\ wt\% = \frac{HW}{LW} \cdot A$.

Further investigations have pointed out that an important chemical parameter defining the compositional dependency on the Raman features is the iron content. Therefore, a further calibration based on the iron percentage of the sample is presented in this work and can be used to estimate the water content $H_2O\ wt\% = \frac{HW}{LW} \cdot m$, in which the *m* coefficient can be calculated as

$$m = 0.096 \cdot FeO + 0.663.$$

For both spectrometers (Roma Tre and LMU) a linear relationship between the *m* coefficient and the iron content was observed. Therefore, following the spectra treatment presented in this study, a unique calibration based on the iron content of the sample can be used to estimate the water content.

The degassing process and exsolution pattern of felsic volcanic systems is under investigated in literature, even if effects of exsolved fluid (i.e. bubbles) on the bulk viscosity of magmas are very important and may contribute to explain typology and evolution of eruptive styles (e.g., explosive vs. effusive). The second part of this thesis concerned the study of the rheology of bubble-bearing and porous silicic melts. It is known that the presence of bubbles is important as they may either increase or decrease the viscosity of the suspension, depending on the deformation environment. Existing models include 1) theoretical models; 2) empirical functions fitted to experiments on analogue materials; 3) empirical functions constrained by few experiments on natural materials. Despite the wide literature available, these studies are often in disagreement and a general parameterization does not exist. In-situ high-temperature degassing and deformation experiments were performed for the first time in order to investigate the rheological behavior of porous melts and viscosity model parameterization is provided for bubble-bearing melts.

The new experimental approach allows to define the relationship between porosity and viscosity in natural rhyolitic magmas, and also to further analyze the nature of the pores and its influence on the rheological behavior. The two experimental strategies, *double-stage* (DS) and *single-stage* (SS), pointed out different features; indeed, DS experiments showed lower viscosity than SS, and this behavior has been attributed to the water loss and/or micro-cracks formation. The same trend among DS experiments was observed in Vona et al., (2016) study, reinforcing our model.

The proposed viscosity models describe the rheological behavior of porous melts and can be applied to different framework (*open-cell* vs. *closed-cell* system). In conclusion, it is possible to affirm that pore nature, as well as porosity fraction, has to be taken into account in multiphase

magmas rheology models; the different rheological response can indeed reflect different volcanic environments and influence the eruptive dynamics and emplacement.

The last part of this thesis regards the study of H_2O resorption, which is a process that can occur after degassing and exsolution during cooling of the magma due to the retrograde solubility of water. All magmas cool and if the cooling rates are slow enough, exsolved water can return in the melt. This phenomenon could have important implication in volcanology; indeed, H_2O resorption during cooling reduces Tg expanding the "melt window" in volcanic systems and causing melts to quench at higher H_2O contents and lower temperatures. Expanding this "melt window" can prolong the "life" of magma and its mobility. Volcanic environments in which this phenomenon could happen are dome extrusion or ignimbrites and lava emplacement.

For this reason, in this study high temperature degassing experiments were performed in order to explore the water resorption process during cooling in order to identify the minimum cooling rate at which H_2O returns in the melt phase and resorption processes occurs. Those experiments proved the high response of the natural obsidian cores to the heating/cooling cycles. Different setups and heating and cooling cycles were tested in order to define the best experimental strategy to investigate this phenomenon. The resorption contribution from the melt and gas thermal expansion was observed and calculated for the "double heating" setup which was proved to be the best experimental approach to investigate this process.

Supplementary Material 1

Effect of iron and nanolites on Raman spectra of volcanic glasses: reassessment of existing strategies to estimate the water content

The supplementary material of this study includes FTIR methodology and analyses of hydrous glasses synthesized in this study, SEM result of nanolite-bearing samples, and Raman spectra of samples affected by laser-induced oxidation. Moreover, a *MATLAB*® code is provided for the Raman spectra (available on request). A *R* code is also available, please feel free to email the corresponding author.

1.1 FTIR methodology

FTIR spectra were collected with a Bruker Vertex 70 spectrometer coupled with an IR Microscope Hyperion 3000 at the Institute of Mineralogy at the University of Göttingen. Operation conditions were: a light source, W lamp for NIR and globar light for MIR; beamsplitter, CaF_2 for NIR and KBr for MIR. To limit the volume of sample analyzed, a square focus area of 50 x 50 mm was chosen. Typically, 100 and 50 scans were accumulated for each spectrum, with a spatial resolution of 4 cm^{-1} for NIR and 2 cm^{-1} for MIR, respectively. The sample thickness was measured using a Mitutoyo digital micrometre, with a precision of 2 mm. The sample thickness was below 400 mm.

1.2 IR results

In the NIR spectra, two water-related bands at ~4500 and ~5200 cm^{-1} are visible for hydrous glasses. The peak at 4500 cm^{-1} reflects the stretching and bending mode of Si-OH groups; the absorption band at 5200 cm^{-1} results from the combination of stretching and bending modes of H_2O molecules (Scholze, 1960, 1966; Bartholomew et al., 1980; Stolper, 1982; Ohlhorst et al., 2001). In the MIR spectra, two banda at ~ 3550 and ~1630 cm^{-1} are visible for hydrous glasses. The first was attributed to the OH stretching vibration of weakly H-bonded hydrous species and it is commonly used to estimate the bulk water content. The latter was assigned to the fundamental H_2O bending vibrations, giving evidence for the presence of H_2O molecules in the glass (Scholze, 1959). Linear

baselines were fitted to the bands at 4500, 5200 and 3550 cm^{-1} to define the peak height (absorbance) (Fig. S1.1 A, B).

We used the Lambert-Beer law to estimate the water concentration of our samples using a baseline-corrected height of the absorption peak:

$$C = MA/d\rho\varepsilon \quad (1)$$

where C is the weight fraction of molecular or OH^- water in wt%, M is the molar mass of the component or species, d is the thickness of the sample in cm, ρ is the density in g/l, and ε is the linear molar absorption coefficient in $l \cdot mol^{-1} \cdot cm^{-1}$.

For the HO spectra (dacite), the e_{4500} = 0.97 ± 0.04 $l \cdot mol^{-1} \cdot cm^{-1}$ and e_{5200} = 1.11 ± 0.05 $l \cdot mol^{-1} \cdot cm^{-1}$ were used (Ohlhorst et al., 2001), while e_{4500} = 1.41 ± 0.07 $l \cdot mol^{-1} \cdot cm^{-1}$ and e_{5200} = 1.66 ± 0.05 $l \cdot mol^{-1} \cdot cm^{-1}$ were adopted for the RH rhyolite (Withers and Behrens, 1999). The employed absorption coefficients for the MIR band is e_{3550} = 76 $l \cdot mol^{-1} \cdot cm^{-1}$ (Stolper, 1982).

Figures

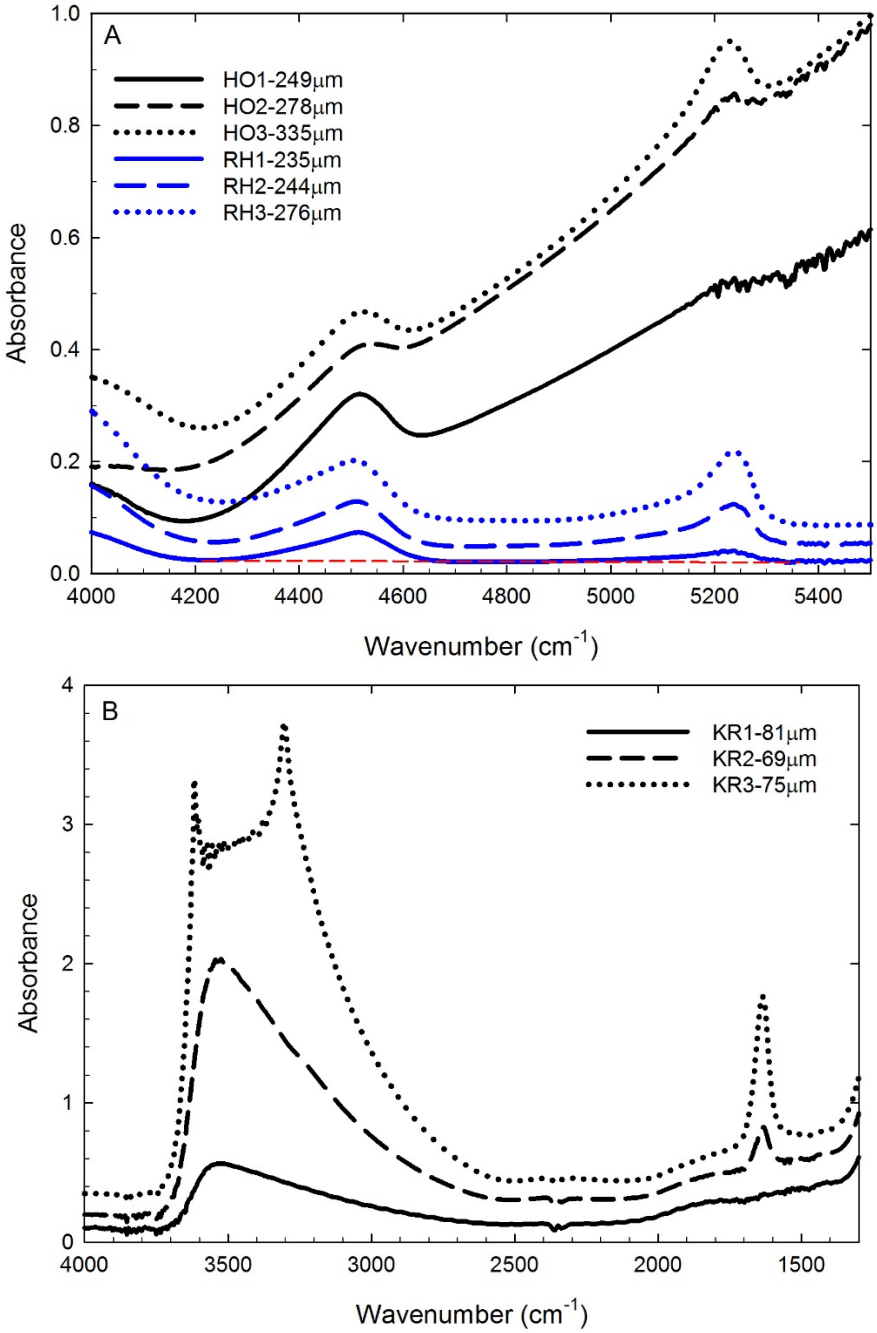

Fig. S1.1. (A) NIR absorption spectra of hydrous OH and RH glasses (T=1200°C; P=3kbar). The 4500 cm^{-1} and 5200 cm^{-1} bands represent the combination mode of OH of H_2O molecules groups, respectively. Dashed line shows the baseline used to calculate the peak intensities. HO spectra show a dramatic change in the absorption due to the crystal field transitions of iron (Ohlhorst et al., 2001) and, possibly, iron-bearing nanolites (see main text for more details). (B) MIR absorption spectra of hydrous experimental KR glasses (T=1200°C; P=3kbar). For the KR3 sample, the saturation of the OH band at 3550 cm^{-1} was reached. Sample thickness is reported in the legend.

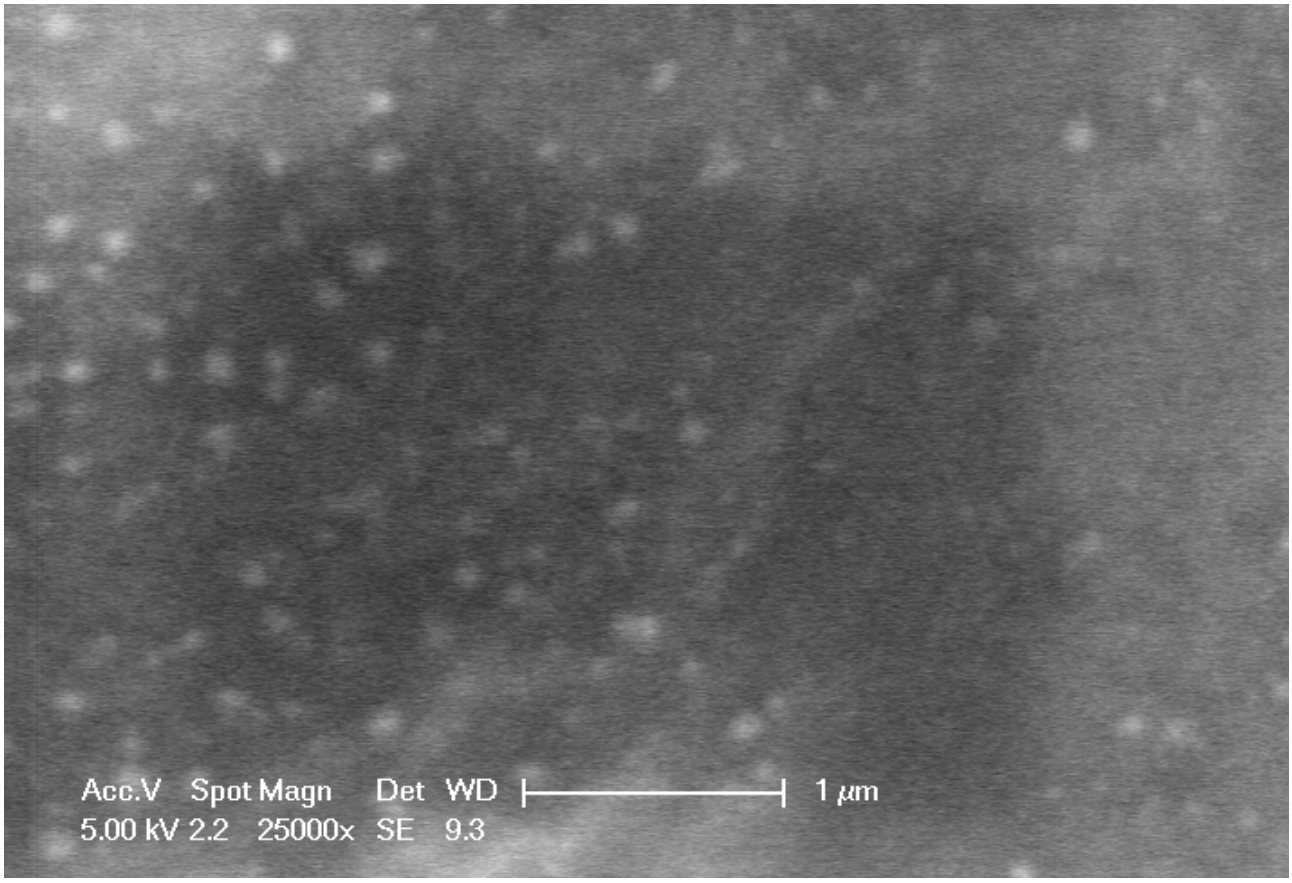

Fig. S2.1. Scanning Electron Microscopy (SEM) image of the KR glass containing nanolites (light particles). The spectra of this sample showed a peak at ~690 cm^{-1} which reflects the presence of iron-bearing oxides (i.e. magnetite, see main text for a detailed discussion).

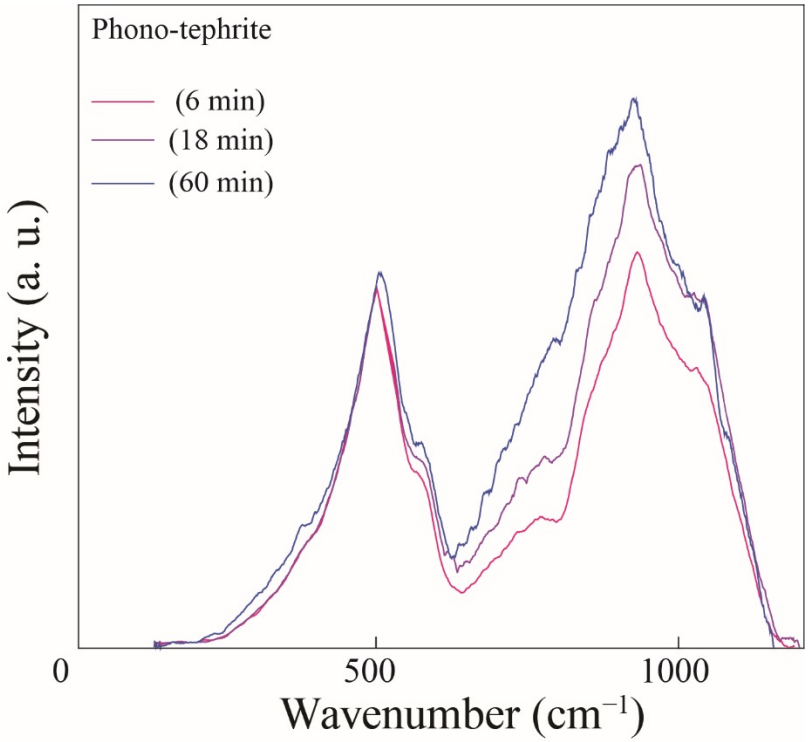

Fig. S3.1 Corrected Raman spectra (LW region) of the phono-tephrite sample (V_1631_3, $FeO_{tot.}$ = 4.8 wt.%, H_2O = 3.32). With increasing the acquisition time, the region at ~970 cm-1 increased suggesting that the sample oxidized with time (see main text for more details). Numbers in the legend show the acquisition time for each spectrum.

Table S1

Measured water speciation ($H_2O_{mol.}$ and OH^-) and total water content of hydrous sample synthesised in this study using the band at ~5200, ~4500, and ~3550 cm^{-1}, respectively. For each sample, three different wafers were used.

Sample	FTIR[a]			ρ[b]
	$H_2O_{molec.}$	OH^-	$H2O_{tot.}$	(g l^{-1})
KR1	-	-	0.58 (±0.04)	2678
KR2	-	-	2.75 (±0.18)	2656
HO1	0.06 (±0.01)	1.05 (±0.06)	-	2560
HO2	0.69 (±0.12)	2.21 (±0.13)	-	2539
HO3	2.07 (±0.14)	1.99 (±0.12)	-	2530
RH1	0.45 (±0.02)	1.27 (±0.08)	-	2382
RH2	1.37 (±0.07)	1.80 (±0.12)	-	2372
RH3	2.16 (±0.11)	2.03 (±0.13)	-	2365

[a] Water content (wt%) measured by Infrared spectroscopy.

[b] The glass density was calculated after Lange and Carmichael, 1990.

Molar absorption coefficients for the combination band of OH^- at ~4500 cm^{-1} and H_2O_m at ~5200 cm^{-1}, total water $H_2O_{tot.}$ at ~3550 cm^{-1} are reporte in the main text.

Supplementary Material 2

Bubbles vs. Pores: a rheological study

2.1 Differential Scanning Calorimetry (DSC)

Calorimetric measurements were performed by Differential Scanning Calorimeter (DSC) technique (Netzsch DSC 404 Pegasus, EVPLab Rome Tre University) calibrated using melting temperatures of standard materials (inorganic salts of Rb, K, Cs and Ba) up to 1000 °C. A doubly polished sample 40 mg in weight was placed in a Pt/Rh crucible under a constant Argon flow rate (20 lt/min). The sample was heated at 1 °C/min from room temperature to 50 °C where it was kept for one hour to achieve DSC signal equilibrium. Subsequently, T was raised with a heating rate of 20 °C/min up to about 50 °C above the estimated glass transition temperature (Tg) of the sample. The trace of this first heating is related to natural cooling rates (black curve, Fig. S1.2). Subsequently, measurements of Tg were performed in 3 subsequent thermal treatments where the heating rates always matched the previous cooling rates (20–10–5 °C/min) (colored curves, Fig. S1.2). In order to convert raw DSC signals to absolute heat capacity values (Cp, J g^{-1} $°C^{-1}$), a baseline measurement was taken where two empty Pt/Rh crucibles were loaded into the DSC and then the DSC was calibrated against the Cp of a single sapphire crystal (Robie et al., 1979). The heat capacity versus temperature paths did not show any evidence of crystallization during the experiments, as also confirmed by post run optical analysis.

Table S1. Glass transition temperatures (Tg) determined at the peak of heat capacity by DSC analysis for different cooling rates

Cooling rate (°C/min)	Tg (°C)
5	725.3
10	704.8
20	700.2

Table S1 includes the glass transition temperatures (Tg_{peak}) determined at the peak value of heat capacity curves for different prescribed cooling rates (colored curves, Fig. S1.2).
Glass transition temperatures (Tg_{peak}) ranging from 700 to 725 °C, as a function of cooling rate, increasing with increasing cooling rate (5, 10, 20 °C).

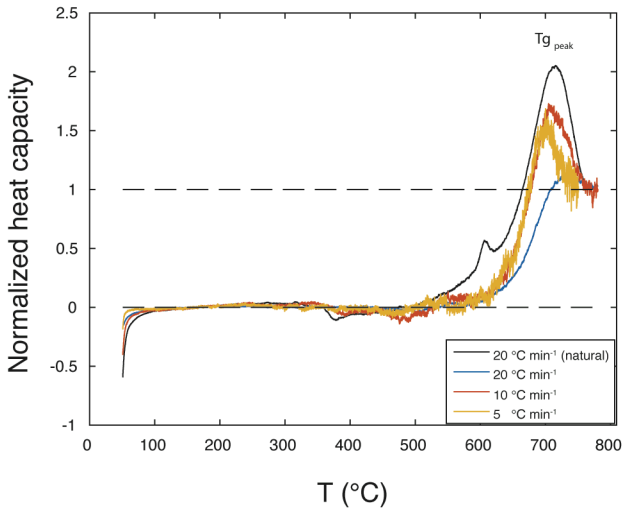

Figure S1.2. Normalized traces of heat capacity (Cp) and T (°C) data. The different colored curves are relative to different cooling rates (20, 10, 5 °C). The Tg_{peak} value decreases as the cooling rate decreases.

One additional DSC analysis was performed to higher target temperature (900 °C) to replicate the thermal treatment undergone by samples during TMA measurements (i.e., 5 °C/min up to 900°C) and to compare DSC- and TMA-derived glass transition interval and reaction onset (e.g., volatile exsolution and crystallization) above Tg. Results of this measurement are displayed and discussed in Fig. 2 in Chapter 2.

2.1 Pre-deformation geometry

Pre-run cores were completely characterized in terms of length and diameter with precision digital calliper and mass with a high-precision balance ($\sigma \pm$ ~0.006 mg). For the initial properties we used the suffix "0" (e.g., L_0, D_0, m_0,). The porosity of the undeformed sample (ϕ_0) is zero (unvesiculated obsidian samples).

The knowledge of the post-foaming and pre-deformation geometry (named with the suffix "i", e.g., L_i, D_i, ϕ_i) is crucial for the determination of the sample rheological properties. The variation in length (i.e. displacement) of the samples during deformation phase was continuously recorded and used to calculate the viscosity of the foamed cores. Viscosity was continuously calculated using the parallel plate theory (Gent, 1960). In the computation also the diameter (and therefore the volume) of the sample is needed.

For *double-stage* measurements the foamed core geometry (i.e. Length, L_i, Diameter, D_i, Volume, V_i, Porosity, ϕ_i) was directly measured prior to reheating and deformation. Conversely, for *single-stage* experiments the pre-deformation geometry of the foamed cores needed to be calculated. In such experiments, lowering the probe on the sample directly after the foaming stage

allowed the measurement of the foamed sample height (i.e. Length, L_i), but no information was accessible on sample diameter (D_i) (and therefore V_i and ϕ_i).

Therefore, a calibration for the samples geometric variation as function of degassing process is needed. To do this, we took into account the *double-stage* experiments, in which foaming and rheological measurements are two separate steps, and the samples were extracted from the instrument before the deformation stage allowing for the direct measurement of their geometrical features (L_i, D_i, V_i and ϕ_i,) by calliper and He-pycnometer.

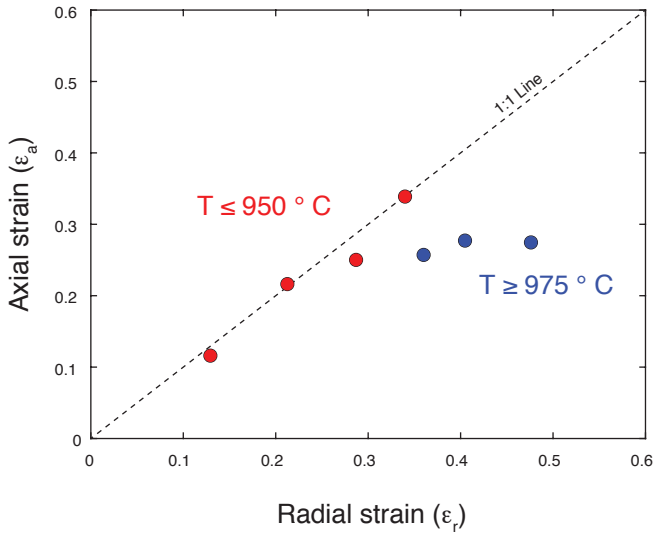

Figure S2.2 Radial stain (ε_r) vs. Axial strain (ε_a) of *double-stage* suite of experiments. The 1:1 relationship between ε_r and ε_a seems true for experiments below 950 °C; a different trend is followed by experiments at T ≥ 975 °C, where radial expansion becomes larger the axial one.

In Fig.S2.2, a comparison of measured axial $[\varepsilon_a = (L_i - L_0)/L_0]$ and radial $[\varepsilon_r = (D_{max} - D_0)/D_0]$ strain for *double-stage* experiments is displayed. Two different trends can be recognized as a function of foaming temperature. Cores run at T ≤ 950 °C (i.e. 900, 925 and 950 °C) describe a 1:1 relationship (within error) indicating that at the experimental unconfined conditions sample expansion (i.e. foaming) can be approximated as isotropic. In contrast, cores run at T ≥ 975 °C (i.e. 975, 1000 and 1050 °C) depart from such trend as radial strain (i.e. bulging) becomes larger than axial strain indicating non-isotropic expansion. For this reason, all *single-stage* experiments were conducted at foaming temperatures T_{foam} ≤ 950 °C and the $\varepsilon_a = \varepsilon_r$ model was adopted to estimate foamed core maximum diameter (D_{max}) as:

$$D_{max} = D_0 \left[1 + \left(\frac{L_i - L_0}{L_0}\right)\right] \quad \text{(S.1.1)}$$

The value of D_{max} represents the maximum diameter value. Analysis of post-foaming sample geometry indicates that samples are not perfect cylinders as they are characterized by an incipient barrel shape (Fig. S3.2).

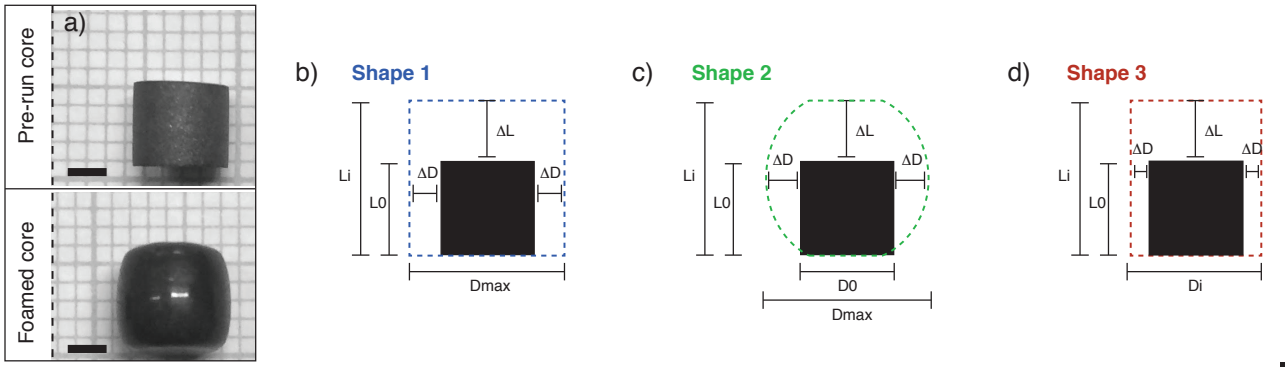

Figure S3.2. Post-foaming porosity calculations. (a) Photograph of starting material (pre-run) and post- foaming sample. Scale bars are 2 mm. (b-d) Sketch of the post-foaming geometries tested for initial porosity (ϕ_i) estimation. b) Shape 1: perfect cylindrical shape. c) Barrel shape with minimum D_0 (and maximum (D_{max}) diameters. d) Shape 3: hybrid cylindrical shape with a mean diameter D_i corresponding to the average of maximum (D_{max}) and minimum (D_0) diameters.

Samples volume V_i and porosity ϕ_i were calculated approximating sample shape to three different geometries:

1. A perfect cylindrical shape with diameter D_{max} ('Shape 1');
2. A barrel shape with minimum $D_0$and maximum (D_{max}) diameters ('Shape 2');
3. A hybrid cylindrical shape with a mean diameter D_i corresponding to the average of maximum (D_{max}) and minimum (D_0) diameters [$(D_i = (D_{max} + D_0)/2]$ ('Shape 3');

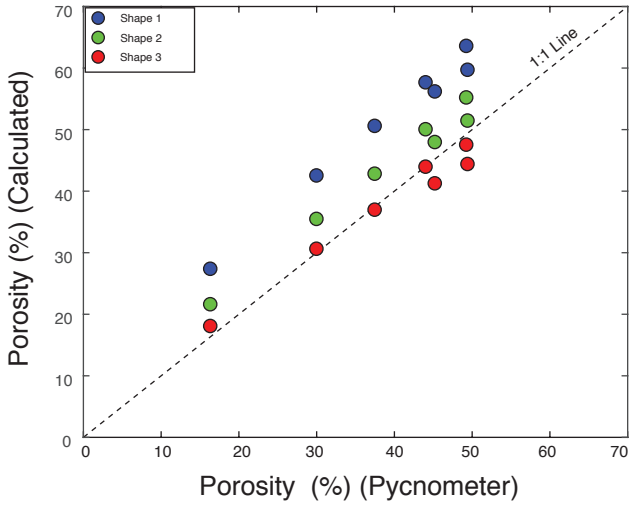

Figure S4.2. Measured (pycnometer) versus calculated (geometrical) initial porosity (ϕ_i). Different shapes are used for the calcualtions: 'Shape 1' (perfect cylinder), 'Shape 2' (barrel) and 'Shape 3' (hybrid cylinder), see Fig. S3. The best approach is to estimate the initial porosity using 'Shape 3' formula, as both 'Shape 1' and 'Shape 2' formulas lead to an overestimation of porosity.

Fig. S4.2 plots the values of porosity measured by pycnometer on foamed cores against porosity values calculated according to the shape assumptions above. 'Shape 3' assumption seems to best reproduce measured data with the lowest root mean square error (RMSE = 2.4 %) with respect to other geometries (RMSE = 4.7 % and 11.8 % for 'Shape 2' and 'Shape 1', respectively).

Therefore, we decided to adopt this geometrical assumption (and the associated error) to calculate the initial volume V_i (post foaming) of the *single stage* experimental samples.

2.2 Deformation of foamed cores and viscosity estimation.

After the foaming stage temperature is reduced from T_{foam} to T_{def} with a cooling rate of 50 °C/min. As T_{def} is reached, the probe is lowered on the sample surface and maintained with load zero for 30 minutes in order reassess the equilibrium of the core at the new temperature. Therefore, a constant load of 150 g is applied on the foamed core (by the probe) and the deformation starts.

On the base of the curves time-displacement, the viscosity of the sample is calculated using Gent's 1960 parallel plate theory. The derived equations describe two different deformation styles*:* *perfect slip* and *no slip*. In perfect slip (Equation S.2.2) during deformation, sample geometry remains rather cylindrical, expanding radius.

$$\eta_{bulk} = \left(\frac{L_i^2 F}{3\ V_i \frac{dL_i}{dt_i}} \right) \quad \text{(S.2.2)}$$

In no slip (Equation S.2.3) the original radius remains unchanged but the sample is subject to shortening.

$$3\eta_{bulk} = \left(\frac{F L_i 2\pi}{3V_i \frac{dL_i}{dt_i} (F L_i 2\pi)^3 + V_i} \right) \quad \text{(S.2.3)}$$

In Gent's formula viscosity is function of the incremental residual length of the core (L_i), load (F), the initial volume of the core (V_i), and the incremental rate of core shortening (dL_i/dt_i). We first considered both Gent's equations for viscosity estimation, showing a little discrepancy ($\approx$ 0.01); nevertheless we decide to take into account perfect slip equation, as it better describes the samples stress accommodation.

2.3 Post-deformation geometry

During deformation stage, the probe was lowered to the sample surface, and a constant load was applied (150 g). The motion of the probe records the sample deformation (displacement, ΔL). At the end of the experiment, samples were extracted from the dilatometer and the final geometrical features were measured (e.g., L_f, D_f, V_f ,ϕ_f, m_f).

The final length measured by calliper (Fig. S5.2a), shows a good agreement with the final length recorded by the dilatometer ($L_{f\_inst} = L_i - \Delta L$) indicating that:

1) All deformation is transferred to the sample;
2) The inferred initial length (L_i) is a good estimation for the actual post-foaming length.

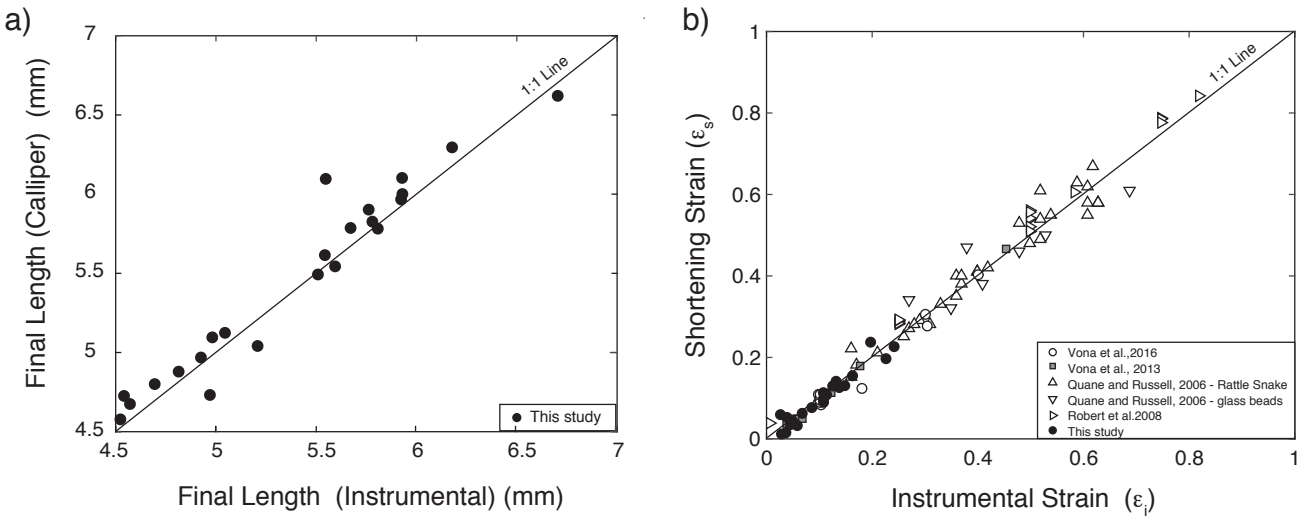

Figure S5.2 Comparison of variation in length (a) and strain (b) after deformation stage. a) Final length measured using precision calliper vs. final length recorded as displacement by the TMA (instrumental). b) Strain estimated from shortening of the cores (ε_s) compared to instrumental strain (ε_i) recorded during experiment. Literature data from high-temperature deformation of porous samples are reported for comparison.

An additional control on the accuracy of the experimental set-up can be given by the comparison between instrumental strain (ε_i) and the strain recorded by the sample as shortening (ε_s). The instrumental strain ($\varepsilon_i = \Delta x/L_i$) is defined as the amount of TMA probe displacement (Δx) over the initial length (L_i). Sample strain ($\varepsilon_s = (L_i - L_f)/L_i$) is calculated as the total shortening of the core. If the total amount of ε_i is accommodated by sample as ε_s, these two values need to be equivalent. As shown in Fig S5.2b, all data display a good match within the error associated with this type of measurements as indicated by scattering in literature data on high temperature deformation experiments on porous materials reported for comparison.

References

Atlas, Z.D., Dixon, J.E., Sen, G., Finny, M., and Martin-Del Pozzo, A.L. (2006). Melt inclusions from Volcán Popocatépetl and Volcán de Colima, Mexico: Melt evolution due to vapor-saturated crystallization during ascent. Journal of Volcanology and Geothermal Research, 153, 221–240.

Bachmann, O., Wallace, P.J., Bourquin, J., (2009). The melt inclusion record from the rhyolitic Kos Plateau Tuff (Aegean Arc). Contrib. Mineral. Petrol. 159, 187–202. http://dx.doi.org/10.1007/s00410-009-0423-4.

Bagdassarov, N.S., Dingwell, D.B., (1992). A rheological investigation of vesicular rhyolite. J. Volcanol. Geotherm Res. 50, 307–322.

Bartholomew R. F., Butler B. L., Hoover H. L. and Wu C. K., (1980). Infrared spectra of a water-containing glass. J. Am. Ceram. Soc. 63, 481–485

Behrens, H., Zhang, Y., (2009). H_2O diffusion in peralkaline to peraluminous rhyolitic melts. Contrib. Mineral. Petrol. 157, 765–780. http://dx.doi.org/10.1007/s00410-008-0363-4.

Behrens, H., Roux, J., Neuville, D.R., Siemann, M., (2006). Quantification of dissolved H_2O in silicate glasses using confocal microRaman spectroscopy. Chem. Geol. 229, 96–112. http://dx.doi.org/10.1016/j.chemgeo.2006.01.014.

Bell, R.J., Dean, P., (1972). The structure of vitreous silica: validity of the random network theory. Philos. Mag. 25, 1381–1398. http://dx.doi.org/10.1080/14786437208223861.

Bell, R.J., Bird, N.F., Dean, P., (1968). The vibrational spectra of vitreous silica, germani and beryllium fluoride. J. Phys. C Solid State Phys. http://dx.doi.org/10.1088/0022-3719/1/2/304.

Berry, A.J., Danyushevsky, L.V., O'Neill, H., Newville, M., Sutton, S.R., (2008). Oxidation state of iron in komatiitic melt inclusions indicates hot Archaean mantle. Nature 455, 960–963. http://dx.doi.org/10.1038/nature07377.

Blundy, J., Cashman, K.V., (2005). Rapid decompression-driven crystallization recorded by melt inclusions from Mount St. Helens volcano. Geology 33, 793. http://dx.doi.org/10.1130/G21668.1.

Bouhifd, M.A., Whittington, A.G., Richet, P., (2015). Densities and volumes of hydrous silicate melts: new measurements and predictions. Chem. Geol. 1–11. http://dx.doi.org/10.1016/j.chemgeo.2015.01.012.

Burgisser, A., Scaillet, B., (2007). Redox evolution of a degassing magma rising to the surface. Nature 445, 194–197.

Burnham, C.W., and Jahns, R.H. (1962). A method for determining the solubility of water in silicate melts. American Journal of Science, 260, 721–745. https://doi.org/10.2475/ajs.260.10.721.

Cabrera, A., Weinberg, R.F., Wright, H.M.N., Zlotnik, S., Cas, R.A.F.,(2011). Melt fracturing and healing: a mechanism for degassing and origin of silicic obsidian. Geology 39, 67–70.
http://dx.doi.org/10.1130/g31355.1.

Carroll, M.R., and Blank, J.G. (1997). The solubility of H_2O in phonolitic melts. American Mineralogist, 82, https://doi.org/549–556.10.2138/am-1997-5-615.

Carroll, M.R., Holloway J.R., (1994). Volatiles in magmas. Mineralogical Society of America 30, 517.

Cassidy, M., Manga, M., Cashman, K., Bachmann O. (2018). Controls on explosive-effusive volcanic eruption styles.Nat. Commun. 19, 9(1)2839. https://doi.org/10.1038/s41467-018-05293-3.

Castro, J. M., M. Manga, and M. C. Martin., (2005). Vesiculation rates of obsidian domes inferred from H_2O concentration profiles, Geophys. 695 Res. Lett., 32, L21307, https://doi.org10.1029/2005GL024029.

Chabiron, A., Pironon, J., Massare, D., (2004). Characterization of water in synthetic rhyolitic glasses and natural melt inclusions by Raman spectroscopy. Contrib. Mineral. Petrol. 146, 485–492. http://dx.doi.org/10.1007/s00410-003-0510-x.

Di Matteo, V., Carroll, M.R., Behrens, H., Vetere, F., and Brooker, R.A. (2004). Water solubility in trachytic melts. Chemical Geology, 213, 187–196. https://doi.org/10.1016/j.chemgeo.2004.08.042

Di Genova, D., Romano, C., Hess, K.U., Vona, A., Poe, B.T., Giordano, D., Dingwell, D.B., Behrens, H., (2013). The rheology of peralkaline rhyolites from Pantelleria Island. J. Volcanol. Geotherm. Res. 249, 201–216.

Di Genova, D., Romano, C., Giordano, D., Alletti, M., (2014a). Heat capacity, configurational heat capacity and fragility of hydrous magmas. Geochim. Cosmochim. Acta 142, 314–333. http://dx.doi.org/10.1016/j.gca.2014.07.012.

Di Genova, D., Romano, C., Alletti, M., Misiti, V., Scarlato, P., (2014b). The effect of CO_2 and H_2O on Etna and Fondo Riccio (Phlegrean Fields) liquid viscosity, glass transition temperature and heat capacity. Chem. Geol. 377, 72–86. http://dx.doi.org/10.1016/j.chemgeo.2014.04.001.

Di Genova, D., Morgavi, D., Hess, K.U., Neuville, D.R., Borovkov, N., Perugini, D., Dingwell, D.B., (2015). Approximate chemical analysis of volcanic glasses using Raman spectroscopy. J. Raman Spectrosc. 46, 1235–1244. http://dx.doi.org/10.1002/jrs.4751.

Di Genova, D., Hess, K.U., Chevrel, M.O., Dingwell, D.B., (2016a). Models for the estimation of Fe^{3+}/Fetot. ratio in terrestrial and extra- terrestrial alkali- and iron-rich silicate glasses using Raman spectroscopy. Am. Mineral. 101, 943–952.

Di Genova, D., Kolzenburg, S., Vona, A., Chevrel, M.O., Hess, K.U., Neuville, D.R., Ertelingrisch, W., Romano, C., Dingwell, D.B., (2016b). Raman spectra of Martian glass analogues: a tool to approximate their chemical composition. J. Geophys. Res. Planets 121, 740–752. https://doi.org/10.1002/2016JE005010.

Di Genova, D., Vasseur, J., Hess, K.U., Neuville, D.R., Dillon, R.T., (2017). Effect of oxygen fugacity on the glass transition, viscosity and structure of silica- and iron-rich magmatic melts. J. Non-Cryst. Solids 0–1. http://dx.doi.org/10.1016/j.jnoncrysol.2017.05.013.

Di Genova D., Kolzenburg S., Wiesmaier S., Dallanave E., Neuville D., Hess K.U., Dingwell D.B., (2017b). A chemical tipping point governing mobilization and eruption style of rhyolitic magma. Nature, https://doi.org/10.1038/nature24488.

Di Muro, A., Giordano, D., Villemant, B., Montagnac, G., Scaillet, B., Romano, C., (2006a). Influence of composition and thermal history of volcanic glasses on water content as determined by micro-Raman spectrometry. Appl. Geochem. 21, 802–812. http://dx.doi.org/10.1016/j.apgeochem.2006.02.009.

Di Muro, A., Villemant, B., Montagnac, G., Scaillet, B., Reynard, B., (2006b). Quantification of water content and speciation in natural silicic glasses (phonolite, dacite, rhyolite) by confocal microRaman spectrometry. Geochim. Cosmochim. Acta 70, 2868–2884. http://dx.doi.org/10.1016/j.gca.2006.02.016.

Di Muro, A., Métrich, N., Mercier, M., Giordano, D., Massare, D., Montagnac, G., (2009). Micro-Raman determination of iron redox state in dry natural glasses: application to peralkaline rhyolites and basalts. Chem. Geol. 259, 78–88. http://dx.doi.org/10. 1016/j.chemgeo.2008.08.013.

Dingwell, D.B., Romano, C., Hess, K.U., (1996). The effect of water on the viscosity of a haplogranitic melt under P-T-X conditions relevant to silicic volcanism. Contrib. Mineral. Petrol. 124, 19–28.

Dingwell, D.B., Holtz, F., and Behrens, H. (1997). The solubility of H_2O in per-alkaline and peraluminous granitic melts. American Mineralogist, 82, 434–437. https://doi.org10.2138/am-1997-3-421

Dingwell, D.B., (2006). Transport properties of magmas: diffusion and rheology. Elements 2, 281–286. http://dx.doi.org/10.2113/gselements.2.5.281.

Dixon, J.E., Stolper, E.M., and Holloway, J.R. (1995). An experimental study of water and carbon dioxide solubilities in mid-ocean ridge basaltic liquids. Part I: Calibration and solubility models. Journal of Petrology, 36, 1607–1631.

Ducamp, V. C., and R. Raj.,(1989). Shear and densification of glass powder compacts, J. Am. Ceram. Soc., 72, 798–804. https://doi.org/10.1111/j.1151-2916.1989.tb06220.x.

Fanara, S., Botcharnikov, R.E., Palladino, D.M., Adams, F., Buddensieck, J., Mulch, A., Behrens, H., (2015). Volatiles in magmas related to the Campanian Ignimbrite eruption: experiments vs. natural findings. Am. Mineral. 100, 2284–

2297. http://dx.doi.org/10.2138/am-2015-5033.

Friedman, I., Long, W., and Smith, R.L. (1963). Viscosity and water content of rhyolite glass. Journal of Geophysical Research, 68, 6523–6535. https://doi.org/10.1029/JZ068i024p06523.

Furukawa, T., Fox, K.E., White, W.B., (1981). Raman spectroscopic investigation of the structure of silicate glasses. III. Raman intensities and structural units in sodium silicate glasses. J. Chem. Phys. 75, 3226. http://dx.doi.org/10.1063/1.442472.

Galeener, F.L., (1982). Planar rings in vitreous silica. J. Non-Cryst. Solids 49, 53–62.

Gardner, J.E., Hilton, M., Carroll, M.R., (2000). Bubble growth in highly viscous silicate melts during continuous decompression from high pressure. Geochim. Cosmochim.Acta 64, 1473–1483.

Gent, A.N., (1960). Theory of the parallel plate viscometer. Br. J. Appl. Phys. 11, 85–87.

Giordano, D., Nichols, A.R.L., and Dingwell, D.B. (2005). Glass transition temperatures of natural hydrous melts: a relationship with shear viscosity and implications for the welding process. Journal of Volcanology and Geothermal Research, 142, 105–118. https://doi.org/10.1016/j.jvolgeores.2004.10.015.

Giordano, D., Russell, J.K., Dingwell, D.B., (2008). Viscosity of magmatic liquids: a model. Earth Planet. Sci. Lett. 271, 123–134. http://dx.doi.org/10.1016/j.epsl.2008.03.038.

Giordano, D., Nichols, A.R.L., Potuzak, M., Di Genova, D., Romano, C., Russell, J.K., (2015). Heat capacity of hydrous trachybasalt from Mt Etna: comparison with $CaAl_2Si_2O_8$ (An)–$CaMgSi_2O_6$ (Di) as basaltic proxy compositions. Contrib. Mineral. Petrol. 170, 48. http://dx.doi.org/10.1007/s00410-015-1196-6.

Gonnermann, H.M., Gardner, J.E., (2013). Homogeneous bubble nucleation in rhyolitic melt: experiments and nonclassical theory. Geochem. Geophys. Geosyst. 14, 4758–4773. http://dx.doi.org/10.1002/ggge.20281.

Gottsmann, J., and Dingwell, D.B, (2001). Cooling dynamics of spatter-fed phonolite obsidian flows on Tenerife, Canary Islands. . J. Volcanol. Geotherm. Res. Volume 105, 323-342 https://doi.org/10.1016/S0377-0273(00)00262-6.

Grunder, A., and Russell, J.K. (2005) Welding processes in volcanology: insights from field, experimental, and modeling studies. Journal of Volcanology and Geothermal Research, 142, 1–9. https://doi.org/10.1016/j.jvolgeores.2004.10.010.

Hammer, J.E., Cashman, K.V., Voight, B., (2000). Magmatic processes revealed by textural and compositional trends in Merapi dome lavas. J. Volcanol. Geotherm. Res. 100, 165–192. http://dx.doi.org/10.1016/S0377-0273(00)00136-0.

Hartley, M.E., Maclennan, J., Edmonds, M., Thordarson, T., (2014). Reconstructing the deep CO_2 degassing behaviour of large basaltic fissure eruptions. Earth Planet. Sci. Lett. 393, 120–131. http://dx.doi.org/10.1016/j.epsl.2014.02.031

Heap, M.J., Kolzenburg, S., Russell, J.K., Campbell, M.E., Welles, J., Farquharson, J.I., Ryan, A.G., (2014). Conditions and timescales for welding block-and-ash flow deposits. J. Volcanol. Geotherm. Res. 289, 202–209. http://dx.doi.org/10.1016/j.jvolgeores.2014.11.010.

Hess, K.-U., and Dingwell, D. B.,(1996). Viscosities of hydrous leucogranitic melts: A non-Arrhenian model, Am. Mineral., 81, 1297–1300.

Hinch, E.J., Acrivos, A., 1980. Long slender drops in a simple shear flow. J. Fluid Mech. 98, 305– 328. https://doi.org/10.1017/S0022112080000171

Holtz, F., Behrens, H., Dingwell, D.B., Johannes, W., (1995). H_2O solubility in haplogranitic melts: Compositional, pressure and temperature dependence. American Mineralogist, 80, 94–108. https://doi.org/10.2138/am-1995-1-210.

Holtz, F., Roux, J., Behrens, H., and Pichavant, M., (2000). Water solubility in silica and quartzofeldspathic melts. American Mineralogist, 85, 682–686. https://hal-insu.archives-ouvertes.fr/hal-00077547.

Humphreys, M.C.S., Brooker, R.A., Fraser, D.G., Burgisser, A., Mangan, M.T., McCammon, C., (2015). Coupled interactions between volatile activity and Fe oxidation state during arc crustal processes. J. Petrol. 56, 795–814.

Keating, G.N., (2005). The role of water in cooling ignimbrites. Journal of Volcanology and Geothermal Research, 142, 145–171.

Kennedy, B., Spieler, O., Scheu, B., Kueppers, U., Taddeucci, J., Dingwell, D.B., (2005). Conduit implosion during Vulcanian eruptions. Geology 33, 581–584. http://dx.doi.org/10.1130/G21488.1.

Kennedy, B.M., Jellinek, A.M., Russell, J.K., Nichols, A.R.L., and Vigouroux, N., (2010). Time-and temperature-dependent conduit wall porosity: A key control on degassing and explosivity at Tarawera volcano, New Zealand. Earth and Planetary Science Letters, 299, 126–137. http://dx.doi./10.1016/j.epsl.2010.08.028.

Kolzenburg, S., and Russell, J.K. (2014) Welding of pyroclastic conduit infill: A mechanism for cyclical explosive eruptions. Journal of Geophysical Research- Solid Earth, 119, 5305–5323. https://doi.org/10.1002/2013JB010931.

Lange, R.A., Carmichael, I.S.E., (1987). Densities of Na_2O-K_2O-CaO-MgO-FeO-Fe_2O_3-Al_2O_3-TiO_2-SiO_2 liquids; new measurements and derived partial molar properties. Geochim.Cosmochim. Acta 2931–2946.

Lange, R.A., Carmichael, I.S.E., (1990). Thermodynamic properties of silicate liquids with emphasis on density, thermal expansion and compressibility. Rev. Mineral. Geochem. 24, 25–64.

Le Gall, N., Pichavant, M., (2016). Homogeneous bubble nucleation in H_2O- and H_2O-CO_2- bearing basaltic melts: results of high temperature decompression experiments. J. Volcanol. Geotherm. Res. 1–18. http://dx.doi.org/10.1016/j.jvolgeores.2016.10.004.

Le Losq, C., Neuville, D.R., Moretti, R., Roux, J., (2012). Determination of water content in silicate glasses using Raman spectrometry: implications for the study of explosive volcanism. Am. Mineral. 97, 779–790. http://dx.doi.org/10.2138/am.2012.3831.

Lejeune, A.M., Bottinga, Y., Trull, T.W., Richet, P., (1999). Rheology of bubble-bearing magmas. Earth Planet. Sci. Lett. 166, 71–84. https://doi.org/10.1016/S0012-821X(98)00278-7

Llewellin, E.W., Manga, M., (2005). Bubble suspension rheology and implications for conduit flow. J. Volcanol. Geotherm. Res. 143, 205–217. http://dx.doi.org/10.1016/j.jvolgeores.2004.09.018

Liu, Y., and Y. Zhang (2000), Bubble growth in rhyolitic melt, Earth Planet. Sci. Lett., 181, 251–264. https://doi.org/10.1016/S0012-821X(00)00197-7.

Liu Y, Zhang YX, Behrens H. (2005). Solubility of H_2O in rhyolitic melts at low pressures and a new empirical model for mixed H_2O-CO_2 solubility in rhyolitic melts. J. Volcanol. Geotherm. Res. 143:219–35. https://doi.org/10.1016/j.jvolgeores.2004.09.019

Long, D.A., (1977). Raman Spectroscopy. vol. 2. McGraw-Hill, pp. 276.

Loughlin, S.C. et al. eds., (2015). Global Volcanic Hazards and Risk, Cambridge, UK: Cambridge University Press, pp.393.

Martel, C., and Bureau H., (2001). In situ high-pressure and high-temperature bubble growth in silicic melts, Earth Planet. Sci. Lett., 191, 763, 115–127. https://doi.org/10.1016/S0012-821X(01)00407-1.

Martel, C., Iacono-Marziano, G., (2015). Timescales of bubble coalescence, outgassing, and foam collapse in decompressed rhyolitic melts. Earth Planet. Sci. Lett. 412, 173–185. http://dx.doi.org/10.1016/j.epsl.2014.12.010.

McIntosh, I. M., E. W. Llewellin, M. C. S. Humphreys, A. R. L. Nichols, A. Burgisser, C. I. Schipper, and J. F. Larsen (2014), Distribution of dissolved water in magmatic growth records growth and resorption of bubbles, Earth Planet. Sci. Lett., 401, 1–11. http://dx.doi.org/10.1016/j.epsl.2014.05.037.

McMillan, P.F., (1984). Structural studies of silicate glasses and melts-applications and limitations of Raman spectroscopy. Am. J. Sci. 69.

Mercier, M., Di Muro, A., Giordano, D., Métrich, N., Lesne, P., Pichavant, M., Scaillet, B., Clocchiatti, R., Montagnac, G., (2009). Influence of glass polymerisation and oxidation on micro-Raman water analysis in alumino-silicate glasses. Geochim. Cosmochim. Acta 73, 197–217. http://dx.doi.org/10.1016/j.gca.2008.09.030.

Métrich, N., Bertagnini, A., Di Muro, A., (2010). Conditions of magma storage, degassing and ascent at Stromboli: new insights into the volcano plumbing system with inferences on the eruptive dynamics. J. Petrol. 51, 603–626. http://dx.doi.org/10.1093/petrology/egp083.

Miyaji, N., Kan'no, A., Kanamaru, T., Mannen, K., (2011). High-resolution reconstruction of the Hoei eruption (AD 1707) of Fuji volcano, Japan. J. Volcanol. Geotherm. Res. 207,113–129. http://dx.doi.org/10.1016/j.jvolgeores.2011.06.013.

McMillan, P.F., (1984). Structural studies of silicate glasses and melts-applications and limitations of Raman spectroscopy. Am. J. Sci. 69.

McMillan, P., Peraudeau, G., Holloway, J., and Coutures, J.-P., (1986). Water solubility in a calcium aluminosilicate melt. Contributions to Mineralogy and Petrology, 94, 178–182. https://doi.org/10.1007/BF00592934

Moore, G., Vennemann, T., and Carmichael, I.S.E., (1998). An empirical model for the solubility of H_2O in magmas in 3 kilobars. American Mineralogist, 83, 36–42. https://doi.org/10.2138/am-1998-1-203.

Morizet, Y., Brooker, R.a., Iacono-Marziano, G., Kjarsgaard, B.a., (2013). Quantification of dissolved CO_2 in silicate glasses using micro-Raman spectroscopy. Am. Mineral. 98,1788–1802. http://dx.doi.org/10.2138/am.2013.4516.

Mungall, J.E., Bagdassarov, N.S., Romano C., Dingwell, D.B., (1996). Numerical modeling of stress generation and microfracturing of vesicle walls in glassy rocks. J. Volcanol. Geotherm. Res Vol. 73, 33-46. https://doi.org/10.1016/0377-0273(96)00017-0.

Mysen, B.O., (2003). Physics and chemistry of silicate glasses and melts. Eur. J. Mineral. 15, 781–802. http://dx.doi.org/10.1127/0935-1221/2003/0015-0781. (ST–Physics and chemistry of silicate gl).

Mysen, B.O., Virgo, D., Scarfe, C.M., (1980). Relations between anionic structure and viscosity of silicate melts - a Raman spectroscopic study. Am. Mineral. 65, 690–710.

Mysen, B.O., Virgo, D., Seifert, F.a., (1982). The structure of silicate melts: implications for chemical and physical properties of natural magma. Rev. Geophys. http://dx.doi.org/10.1029/RG020i003p00353.

Mysen, B.O., and Acton, M., (1999). Water in H_2O-saturated magma-fluid systems: Solubility behavior in K_2O-Al_2O_3 - SiO_2 -H_2O to 2.0 GPa and 1300 °C. Geochi- mica et Cosmochimica Acta, 63, 3799–3815.

Navon, O., A. Chekhmir, and Lyakhovsky V., (1998), Bubble growth in highly viscous melts: Theory, experiments, and autoexplosivity of dome lavas, Earth Planet. Sci. Lett., 160, 763–776 https://doi.org10.1016/S0012-821X(98)00126-5.

Neuville, D.R., Mysen, B.O., (1996). Role of aluminum in the silicate network: in situ, high temperature of glasses and melts on the join SiO_2-$NaAlO_2$. Geochim. Cosmochim. Acta 60, 1727–1737.

Newman, S.,and Lowenstern, J.B., (2002). VOLATILECALC: a silicate melt- H_2O-CO_2 solution model written in Visual Basic for excel. Computers and Geosciences, 28, 597–604.

Ohlhorst, S., Behrens, H., Holtz, F., (2001). Compositional dependence of molar absorptivities of near-infrared OH- and H_2O bands in rhyolitic to basaltic glasses. Chem.Geol. 174, 5–20. http://dx.doi.org/10.1016/S0009-2541(00)00303-X.

Okumura, S., Nakamura, M., Takeuchi, S., Tsuchiyama, A., Nakano, T., Uesugi, K., (2009). Magma deformation may induce non-explosive volcanism via degassing through bubble networks. Earth Planet. Sci. Lett. 281, 267–274. http://dx.doi.org/10.1016/j.epsl.2009.02.036.

Pal R. Rheological behavior of bubble-bearing magmas, (2003). Earth Planet. Sci. Lett 207 165-179. https://doi.org/10.1016/S0012-821X(02)01104-4.

Papale, P., Moretti, R.,Barbato, D., (2006). The compositional dependence of the saturation surface of H_2O+CO_2 fluids in silicate melts. Chemical Geol- ogy, 229, 78–95.

Pinkerton H., Stevenson R.J., (1992). Methods of determining the rheological properties of magmas at sub-liquidus temperatures J. Volcanol. Geotherm. Res. 53, 47-66 https://doi.org/10.1016/0377-0273(92)90073-M.

Poe, B.T., Romano, C., Zotov, N., Cibin, G., Marcelli, A., (2001). Compression mechanisms in aluminosilicate melts: Raman and XANES spectroscopy of glasses quenched from pressures up to 10 GPa. Chem. Geol. 174, 21–31. http://dx.doi.org/10.1016/S0009-2541(00)00304-1.

Poe, B.T., Romano, C., Di Genova, D., Behrens, H., Scarlato, P., (2012). Mixed electrical conduction in a hydrous pantellerite glass. Chem. Geol. 320–321, 140–146. http://dx.doi.org/10.1016/j.chemgeo.2012.05.023.

Pouchou, J.L., Pichoir, F., (1991). Quantitative analysis of homogeneous or stratified microvolumes applying the model "PAP". In: Heinrich, K.F.J., Newbury, D. (Eds.), Electron Probe Quantitation. Springer, US, pp. 31–75. http://dx.doi.org/10.1007/978-1-4899-2617-34.

Quane, S.L., Russell, J.K., (2005). Welding: insights from high-temperature analogue experiments. J. Volcanol. Geotherm. Res. 142, 67–87. http://dx.doi.org/10.1016/j.jvolgeores.2004.10.014.

Quane, S.L., Russell, J.K., Friedlander, E.A., (2009). Time scales of compaction in volcanic systems. Geology 37, 471–474. http://dx.doi.org/10.1130/G25625A.1.

Rahaman, M.N., De Jonghe, L.G., Scherer, G.W., Brook, R.J., (1987). Creep and densification during sintering of glass powder compacts. J. Am. Ceram. Soc. 70, 766–774. https://doi.org/10.1111/j.1151-2916.1987.tb04877.x

Richet, P., Lejeune, A.-M., Holtz, F., & Roux, J. (1996). Water and the viscosity of andesite melts. *Chemical Geology*, *128*(1), 185–197. https://doi.org/10.1016/0009-2541(95)00172-7

Robert, G., Russell, J.K., Giordano, D., (2008). Rheology of porous volcanic materials: high-temperature experimentation under controlled water pressure. Chem. Geol. 256, 216–230. http://dx.doi.org/10.1016/j.chemgeo.2008.06.028.

Romano, C., Mungall, J.E., Sharp, T.G., Dingwell, D.B., (1996). Tensile strengths of hydrous vesicular glasses: an experimental study. Am. Mineral. 81, 1148–1154.https://doi.org/10.2138/am-1996-9-1013.

Romano, C., Giordano, D., Papale, P., Mincione, V., Dingwell, D.B., Rosi, M., (2003). The dry and hydrous viscosities of alkaline melts from Vesuvius and Phlegrean Fields.Chem. Geol. 202, 23–38. http://dx.doi.org/10.1016/s0009-2541(03)00208-0.

Ryan, A.G., Russell, J.K., Nichols, A.R.L., Hess, K.-U., Porritt, L.A., (2015a). Experiments and models on H_2O retrograde solubility in volcanic systems. Am. Mineral. 100, 774–786. http://dx.doi.org/10.2138/am-2015-5030.

Ryan, A.G., Russell, J.K., Hess, K.-U., Phillion, A., Dingwell, D.B., (2015b). Vesiculation in rhyolite at low H_2O contents: a thermodynamic model. Geochem. Geophys. Geosyst. http://dx.doi.org/10.1002/2015GC006024.

Rust, A.C., Manga, M., Cashman, K.V., (2003). Determining flow type, shear rate and shear stress in magmas from bubble shapes and orientations. J. Volcanol. Geotherm. Res. 122, 111–132.
https://doi.org/10.1016/S0377-0273(02)00487-0

Scaillet, B., Macdonald, R., (2001). Phase relations of peralkaline silicic magmas and petrogenetic implications. J. Petrol. 42, 825–845.

Scaillet, B., Pichavant, M., (2004). Crystallization conditions of Vesuvius phonolites. In: Geophys. Res., (Abstract 6), pp. 3764.

Schmidt, B.C., Behrens, H., (2008). Water solubility in phonolite melts: influence of melt composition and temperature. Chem. Geol. 256, 258–267. http://dx.doi.org/10.1016/j.chemgeo.2008.06.043.

Seifert, F., Mysen, B.O., Virgo, D., (1982). Three-dimensional network structure of quenched melts (glass) in the systems SiO_2-$NaAlO_2$, SiO_2-CaAl2O_4 and SiO_2-$MgAl_2O_4$. Am.Mineral. 67, 696–717.

Silver, L., Ihinger, P., and Stolper, E., (1990). The influence of bulk composition on the speciation of water in silicate glasses. Contributions to Mineralogy and Petrology, 104, 142–162. https://doi.org/10.1007/BF00306439.

Sharma, S.K., Mammone, J.F., Nicol, M.F., (1981). Raman investigation of ring configurations in vitreous silica. Nature. http://dx.doi.org/10.1038/292140a0.

Shishkina, T.A., Botcharnikov, R.E., Holtz, F., Almeev, R.R., Portnyagin, M.V., (2010). Solubility of H_2O- and CO_2-bearing fluids in tholeiitic basalts at pressures up to 500 MPa. Chem. Geol. 277, 115–125. http://dx.doi.org/10.1016/j.chemgeo.2010.07.014.

Scholze H., 1959. Der Einbau des Wassers in Glasern. Glastechnische Berichte 32, 81–88, 142–145, 278–281.

Sparks, R.S.J., Tait, S.R., and Yanev, Y., (1999). Dense welding caused by volatile resorption. Journal of the Geological Society, London, 156, 217–225. https://doi.org/10.1144/gsjgs.156.2.0217.

Stabile, P., Giuli, G., Cicconi, M.R., Paris, E., Trapananti, A., Behrens, H., (2017). The effect of oxygen fugacity and Na/(Na + K) ratio on iron speciation in pantelleritic glasses. J. Non-Cryst. Solids 0–1. http://dx.doi.org/10.1016/j.jnoncrysol.2017.09.051.

Stebbins, J.F., McMillan, P.F., Dillon, R.T., (1995). Structure, Dynamics, and Properties of Silicate Melts. Mineralogical Society of America, Chantilly.

Stein, D.J., Spera, F.J., (2002). Shear viscosity of rhyolite-vapor emulsions at magmatic temperatures by concentric cylinder rheometry. J. Volcanol. Geotherm. Res. 113, 243–258. https://doi.org/10.1016/S0377-0273(01)00260-8

Stolper, E. M., (1982). Water in silicate glasses: An infrared spectroscopic study. Contrib. to Mineral. Petrol. 81, 1–17.

Sura, V.M., Panda, P.C., (1990). Viscosity of porous glasses. J. Am. Ceram. Soc. 73, 2697–2701. https://doi.org/10.1111/j.1151-2916.1990.tb06748.x

Svensen, H. et al., (2004). Release of methane from a volcanic basin as a mechanism for initial Eocene global warming. Nature, 429(6991), pp.542–245.

Taylor, G.I., (1934). The formation of emulsions in definable fields of flow. Proc. R. Soc. A 146, 501– 523. https://doi.org/110.1098/rspa.1934.0169

Thomas, R., (2000). Determination of water contents of granite melt inclusions by confocal laser Raman microprobe spectroscopy. Am. Mineral. 85, 868–872.

Thomas, S.M., Thomas, R., Davidson, P., Reichart, P., Koch-Müller, M., Dollinger, G., (2008). Application of Raman spectroscopy to quantify trace water concentrations in glasses and garnets. Am. Mineral. 93, 1550–1557. http://dx.doi.org/10.2138/am.2008.2834.

Tryggvason, E., (1986). Multiple magma reservoirs in a rift zone volcano: ground deformation and magma transport during the September 1984 eruption of Krafla, Iceland. J. Volcanol. Geotherm. Res. 28, 1–44. http://dx.doi.org/10.1016/0377-0273(86)90003-X.

Tuffen, H., Castro, J.M., (2009). The emplacement of an obsidian dyke through thin ice: Hrafntinnuhryggur, Krafla Iceland. J. Volcanol. Geotherm. Res. 185, 352–366. http://dx.doi.org/10.1016/j.jvolgeores.2008.10.021.

Vasseur, J., Wadsworth, F.B., Lavall.e, Y., Hess, K.-U., Dingwell, D.B., (2013). Volcanic sintering: timescales of viscous densification and strength recovery. Geophys. Res. Lett. 40, 5658–5664. http://dx.doi.org/10.1002/2013GL058105.

Vetere, F., Behrens, H., Holtz, F., & Neuville, D. R. (2006). Viscosity of andesitic melts—new experimental data and a revised calculation model. *Chemical Geology*, *228*(4), 233–245. http://doi.org/https://doi.org/10.1016/j.chemgeo.2005.10.009

Vona A., Ryan A.G., Russell J.K, Romano C., (2016). Models for viscosity and shear localization in bubble-rich magmas. Earth Planet. Sci. Lett 449, 26-38 https://doi.org/10.1016/j.epsl.2016.05.029

Webb, S.L. and DingweU, D.B., (1990). Non-Newtonian rheology of igneous melts at high stresses and strain rates: experimental results for rhyolite, andesite, basalt, and nephelinite. J. Geophys. Res., 95(B10): 15,965-15,701.

Yamashita, S., (1999). Experimental study of the effect of temperature on water solubility in natural rhyolite melt to 100 MPa, J. Petrol., 40, 815, 497–1507. https://doi.org/10.1016/j.jvolgeores.2004.09.019.

Wallace, P.J., Anderson Jr.A.T., Davis A.M., (1995). Quantification of pre-eruptive exsolved gas contents in silicic magmas. Nature 377:612–16

Whittington, A., Richet, P., Holtz, F., (2000). Water and the viscosity of depolymerized aluminosilicate melts. Geochim. Cosmochim. Acta 64, 3725–3736.

Withers, A.C., Behrens, H., (1999). Temperature-induced changes in the NIR spectra of hydrous albitic and rhyolitic glasses between 300 and 100 K. Phys. Chem. Miner. 119–132.

Zhang, Y., (1999). H_2O in rhyolitic glasses and melts: Measurement, speciation, solubility and diffusion. Reviews of Geophysics, 37, 493–516. https://doi.org/10.1029/1999RG900012

Zhang, Y., Xu, Z., Zhu, M., and Wang, H., (2007). Silicate melt properties and volcanic eruptions. Reviews of Geophysics, 45, RG4004 https://doi.org/10.1029/2006RG000216.

Zajacz, Z., Halter, W., Malfait, W.J., Bachmann, O., Bodnar, R.J., Hirschmann, M.M., Mandeville, C.W., Morizet, Y., Müntener, O., Ulmer, P., Webster, J.D., (2005). A composition-independent quantitative determination of the water content in silicate glasses and silicate melt inclusions by confocal Raman spectroscopy. Contrib. Mineral. Petrol. 150, 631–642. http://dx.doi.org/10.1007/s00410-005-0040-9.

Zotov, N., Keppler, H., (1998). The influence of water on the structure of hydrous sodium tetrasilicate glasses. Am. Mineral. 83, 823–834.